

INFORMATION TO USERS

This manuscript has been reproduced from the microfilm master. UMI films the text directly from the original or copy submitted. Thus, some thesis and dissertation copies are in typewriter face, while others may be from any type of computer printer.

The quality of this reproduction is dependent upon the quality of the copy submitted. Broken or indistinct print, colored or poor quality illustrations and photographs, print bleedthrough, substandard margins, and improper alignment can adversely affect reproduction.

In the unlikely event that the author did not send UMI a complete manuscript and there are missing pages, these will be noted. Also, if unauthorized copyright material had to be removed, a note will indicate the deletion.

Oversize materials (e.g., maps, drawings, charts) are reproduced by sectioning the original, beginning at the upper left-hand corner and continuing from left to right in equal sections with small overlaps.

Photographs included in the original manuscript have been reproduced xerographically in this copy. Higher quality 6" x 9" black and white photographic prints are available for any photographs or illustrations appearing in this copy for an additional charge. Contact UMI directly to order.

**ProQuest Information and Learning
300 North Zeeb Road, Ann Arbor, MI 48106-1346 USA
800-521-0600**

UMI[®]

University of Alberta

**Surface Morphology and Nanomechanical Properties of Tribological Antiwear
Films Derived from Zinc Dialkyl Dithiophosphate Compounds**

By

Mirwais Aktary



**A thesis submitted to the faculty of Graduate Studies and Research in partial fulfillment
of the requirements for the degree of Doctor of Philosophy**

Department of Chemistry

Edmonton, Alberta, Canada

Spring 2002



**National Library
of Canada**

**Acquisitions and
Bibliographic Services**

**395 Wellington Street
Ottawa ON K1A 0N4
Canada**

**Bibliothèque nationale
du Canada**

**Acquisitions et
services bibliographiques**

**395, rue Wellington
Ottawa ON K1A 0N4
Canada**

Your file Votre référence

Our file Notre référence

The author has granted a non-exclusive licence allowing the National Library of Canada to reproduce, loan, distribute or sell copies of this thesis in microform, paper or electronic formats.

The author retains ownership of the copyright in this thesis. Neither the thesis nor substantial extracts from it may be printed or otherwise reproduced without the author's permission.

L'auteur a accordé une licence non exclusive permettant à la Bibliothèque nationale du Canada de reproduire, prêter, distribuer ou vendre des copies de cette thèse sous la forme de microfiche/film, de reproduction sur papier ou sur format électronique.

L'auteur conserve la propriété du droit d'auteur qui protège cette thèse. Ni la thèse ni des extraits substantiels de celle-ci ne doivent être imprimés ou autrement reproduits sans son autorisation.

0-612-68535-7

Canada

University of Alberta

Library Release Form

Name of Author: Mirwais Aktary

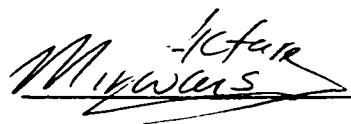
Title of Thesis: Surface Morphology and Nanomechanical Properties of Tribological Antiwear Films Derived from Zinc Dialkyl Dithiophosphate Compounds

Degree: Doctor of Philosophy

Year this Degree Granted: 2002

Permission is hereby granted to the University of Alberta Library to reproduce single copies of this thesis and to lend or sell such copies for private, scholarly or scientific research purposes only.

The author reserves all other publication and other rights in association with the copyright in the thesis, and except as herein before provided, neither the thesis nor any substantial portion thereof may be printed or otherwise reproduced in any material form whatever without the author's prior written permission.



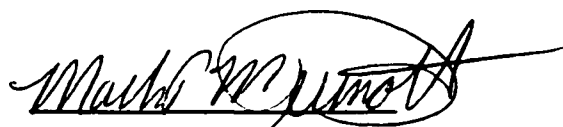
14939 – 72A Street
Edmonton, Alberta
Canada T5C 0S3

December 20, 2001

University of Alberta

Faculty of Graduate Studies and Research

The undersigned certify that they have read and recommended to the Faculty of Graduate Studies and Research for acceptance, a thesis entitled "Surface Morphology and Nanomechanical Properties of Tribological Antiwear Films Derived from Zinc Dialkyl Dithiophosphate Compounds" submitted by Mirwais Aktary in partial fulfillment of the requirements for the degree of Doctor of Philosophy.



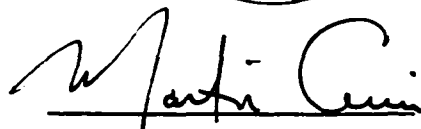
Dr. Mark T. McDermott



Dr. Frederick F. Cantwell



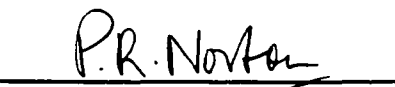
Dr. Charles A. Lucy



Dr. Martin Cowie



Dr. Michael Brett



Dr. Peter R. Norton, External
Examiner, University of
Western Ontario

DEC 10, 2001
Date

Dedication

This thesis is dedicated to my mother and father Nafissa and Nacim Aktary, to my brothers Walie and Zackie Aktary, and to my little sister Sara Aktary.

This thesis is also dedicated to the memory of my mother who gave her life in bringing me to this world and to the memory of my grandmother who shaped the most important seven years of my life.

Abstract

The protection of mechanical equipment from wear is of significant economic interest. It has been estimated that up to half of a percent of the gross domestic product of industrialized countries goes to replacing mechanical components that have lost compliance due to wear. Antiwear additives are key ingredients in lubrication oils that assist in protecting components from wear during high loads. These agents form sacrificial films on metal parts that limit the adhesion between the contacting surfaces and reduce the wear rate considerably. One of the most common classes of compounds employed as an antiwear agent is zinc dialkyldithiophosphates (ZDDP).

This work will explore the formation, structure, and mechanical properties of ZDDP derived antiwear films on the nanoscale. These studies are important because the macroscopic performance of antiwear coatings is dictated by their nanoscale surface properties. As a first study, scanning force microscopy (SFM) is employed to track the formation of films formed from the thermooxidative decomposition of ZDDP on gold substrates. The SFM analysis is correlated with infrared spectroscopy to relate surface structure to chemical composition.

The morphology and mechanical strength of ZDDP tribofilms formed at the interface of sliding stainless steel contacts is also investigated. The tribofilms evolve morphologically with contact time and are characterized by distinct segregated islands at low times that transforms to a full film at longer times. The nanomechanical properties of the tribofilms are evaluated by nanoindentation analysis. It is found that the films are mechanically softer than the underlying

steel substrate. SFM and nanoindentation analyses reveal that calcium sulphonate detergents promote the formation of ZDDP tribofilms and impart to them greater mechanical stability. By contrast succinimide dispersants reduce the capacity of ZDDP to form effective antiwear films.

The first application of SFM and nanoindentation to the study of automotive engine components obtained directly from vehicles is demonstrated. The wear zone on a rocker arm bridge from a diesel engine is shown to contain a tribofilm at the periphery of contact where the contact load is less. SFM images also reveal wear damage at the center of the wear zone where the contact load is expected to be higher.

Acknowledgements

I begin by thanking God for the gift of knowledge and the sense of curiosity. I hope that He will guide me to use this knowledge in the future to better myself and to help my surroundings.

This work would not have been possible without the support of my Supervisor Prof. Mark McDermott. I would like to express my sincere gratitude for all your kindness and encouragement. Mark, it is only that when we leave the group that we truly realize the resource you have been. I will miss working with you a great deal. I would like to thank the McDermott group members. You have been a great bunch and made my life as a graduate student comforting and enjoyable. I wish you all the best in the future.

And last but not least, I want to thank my family for their love and patience, especially over the last few months when I have been occupied with preparing this discourse. I want to thank my parents Nacim and Nafissa Aktary for making me understand the importance of education. I hope that I have lived up to your expectations. To my brothers Walie and Zackie Aktary and to my sister Sara Aktary; now the pressure is on you to keep the family tradition going. I would like to also acknowledge my extended families that live throughout the world. I want to specifically mention my Uncle Osman Akhtary for his love and encouragement and my cousin Aziz Akhtary for his support and devotion.

Table of Contents

Chapter I: Synopsis and Introduction	Page
General Introduction	1
Friction and Wear	2
Lubrication of Mechanical Systems	6
Engine Oil Formulations	10
Studies of Boundary Films of ZDDP	18
Techniques Utilized in this Work	25
Research Objectives	36
References	38

Chapter II: Morphological Evolution of Films Formed from the Thermooxidative Decomposition of ZDDP

Introduction	44
Experimental	46
Results and Discussions	49
Conclusion	65
References	67

Chapter III: Morphological and Nanomechanical Properties of ZDDP Tribofilms

Introduction	69
Experimental	73
Results and Discussions	76
Conclusion	102
References	103

Chapter IV: The Effect of Detergents and Dispersant on the Morphology and Nanomechanical Properties of ZDDP Tribofilms

Introduction	107
Experimental	114
Results and Discussions	115
Conclusion	131
References	133

Chapter V: Morphology and Nanomechanical Properties of Automotive Engine Components

Introduction	135
Experimental	137
Results and Discussions	140
Conclusion	161
References	162

Chapter VI: Conclusion and Future Work

Overall Conclusions	164
Suggestions for Future Work	169
References	173

Appendix A: Surface Directed Deposition of Platinum Nanostructures on Graphite by Chemical Vapor Deposition

Introduction	175
Experimental	177
Results and Discussions	178
Conclusion	186
References	186

List of Tables

	Page
Table 1.1. Constituents of modern automotive lubrication blends.	14
Table 3.1. Indentation moduli and Hardness values of ZDDP tribofilms prepared in the presence of 1.5 wt. % ZDDP as a function of rubbing time in a C – P wear tester.	89
Table 4.1. Indentation moduli of ZDDP tribofilms prepared in the presence of 2.0 wt. % Ca sulphonate detergent, 7.0 wt. % PIBSA dispersant, and 1. 5 wt. % ZDDP as a function of rubbing time in a C – P wear tester.	122
Table 5.1. Elemental composition of the engine oil used to lubricate the rocker arm bridges.	139
Table 5.2. X-ray atomic energy lines of the elements.	148

List of Figures

	Page
Figure 1.1. Microscopic view of the interfacial regions between sliding blocks illustrating the inherent roughness in the surface topography.	4
Figure 1.2. Hypothetical wear rate and frictional force as a function of load and sliding velocity for planar lubricated contact.	8
Figure 1.3. Hydrodynamic lubrication of planar sliding contact by an interposed fluid film.	9
Figure 1.4. Microscopic view of the interfacial region during boundary lubrication showing metal to metal contact between asperities from opposing surfaces.	11
Figure 1.5. Composition of base stock extracts from crude petroleum oil.	13
Figure 1.6. Microscopic view of the interfacial region between opposing bodies showing how an antiwear film may prevent asperity contact during boundary lubrication.	17
Figure 1.7. An idealized model of the polymeric phosphate antiwear film intertwined with FeO on the surface.	23
Figure 1.8. Diagram of a scanning force microscope with a reflection based detection system.	27
Figure 1.9. An illustration of the loading and unloading cycle of a triangular tip penetrating a surface.	29
Figure 1.10. Load functions in a nanoindentation experiment.	31
Figure 1.11. The complete nanoindentation profile of an isotropic material.	32
Figure 2.1. Procedure for preparing and characterizing ZDDP thermal films on Au.	48
Figure 2.2. Topographic $5 \times 5 \mu\text{m}$ (z-scale = 10 nm) of (A) Unmodified Au substrate, (B) Au substrate immersed in MCT 10 base oil for 6 h at 150°C .	50

Figure 2.3.	IRRAS spectra of Au substrates immersed in base oil for 6 h at 150°C and Topographic 5 × 5 μm (z-scale = 20 nm) of Au substrate immersed in EHC 45 base oil for 6h	52
Figure 2.4.	Topographic 50 × 50 μm images of substrate immersed in a 1.5 wt. % ZDDP solution for various lengths of time at 150°C.	54
Figure 2.5.	ZDDP oil solutions heated for less than and greater than 2 h of heating.	56
Figure 2.6.	IRRAS spectra of Au substrate immersed in a 1.5 wt.% ZDDP solution at 150° C.	57
Figure 2.7.	Topographic 15 × 15 μm image obtained with a nanoindentation system. The bottom portion of the image is a topographic line trace across the image as indicated by the white trace on the image.	60
Figure 2.8.	Plot of thickness against immersion time for ZDDP films formed on Au substrates.	62
Figure 2.9.	Higher resolution 1 × 1 μm images of Au substrates immersed in a 1.5 wt.% ZDDP solution for various lengths of time held at 150°C.	64
Figure 2.10.	A model representing the morphology of the film After 6 h of immersion in a heated oil bath of ZDDP.	66
Figure 3.1.	(A) Cross sectional view of the Cameron – Plint wear tester used to prepare the tribofilm samples. (B) Photograph of a 1 × 1 cm steel coupon after the deposition of a tribofilm.	70
Figure 3.2.	Schematic of the nanoindentation system used to determine the nanomechanical properties of the tribofilms.	75
Figure 3.3.	SEM images of a tribofilm prepared from 5 min and 40 min of rubbing contact in C - P wear tester.	77

Figure 3.4.	EDX spectra collected from the 5 min tribofilm sample. Spectrum 1 and 2 correspond to the labels 1 and 2 in Figure 3.3A. Spectrum 3 results from the subtraction of 1 from 2.	78
Figure 3.5.	Topographic 100 × 100 μm contact mode SFM images (z-scale = 200 nm) of tribofilms formed in a Cameron-Plint wear tester for different times.	80
Figure 3.6.	Topographic 100 × 100 μm contact mode SFM images (z-scale = 200 nm) of the 40 min tribofilm illustrating the morphological heterogeneity on different regions of the film.	83
Figure 3.7.	Topographic 50 × 50 μm (z-scale = 300 nm) of 10 min tribofilm generated with the nanoindentation system using a cube corner diamond tip.	86
Figure 3.8.	Nanoindentation profiles up to a maximum force of 100 μN of (A) steel substrate, (B) 120 min film and (C) 10 min film.	88
Figure 3.9.	Nanoindentation profiles from different regions of a 5 min tribofilm. and the profile of a thermooxidative ZDDP film formed from 3 h of heating.	91
Figure 3.10.	Topographic SFM images of ZDDP tribofilms prepared in the presence of soot debris.	95
Figure 3.11.	Nanoindentation profiles of ZDDP tribofilms prepared in the presence of soot debris. Also shown is the profile of standard 60 min ZDDP tribofilm.	98
Figure 3.12.	Topographic SFM images of a tribofilm prepared from 2 h of rubbing at a reciprocating frequency of 10 Hz.	101
Figure 4.1.	Structure of several automotive engine oil detergents where M is a monovalent or divalent atom.	109
Figure 4.2.	Structure of the dispersant polyisobutenyl succinic anhydride polyamine (PIBSA).	111
Figure 4.3.	SEM images of films prepared from 5 and 40 min of rubbing in a lubrication blend consisting of 1.5 wt.% ZDDP and 2.0 wt.% overbased Ca sulphonate detergent.	116

Figure 4.4.	EDX spectra of tribofilms prepared from a blend consisting of 1.5 wt.% ZDDP + 2 wt.% overbased Ca sulphonate rubbed for 5 min and 40 min	118
Figure 4.5.	Topographic 50 x 50 μm SFM images of ZDDP tribofilms prepared in a blend consisting of 1.5 wt.% ZDDP and 2 wt.% overbased Ca sulphonate detergent.	119
Figure 4.6.	Nanoindentation profiles of ZDDP tribofilms prepared from 40 min of rubbing in the presence and absence of overbased Ca sulphonate.	123
Figure 4.7.	SEM images of films prepared from 5 and 40 min of rubbing in a lubrication blend consisting of 1.5 wt.% ZDDP and 7.0 wt.% PIBSA dispersant.	125
Figure 4.8.	EDX spectra of film prepared from a blend consisting of 1.5 wt.% ZDDP + 7 wt.% PIBSA dispersant rubbed for 5 and 40 min	127
Figure 4.9.	Topographic 50 x 50 μm SFM images of ZDDP tribofilms prepared in a blend consisting of 1.5 wt.% ZDDP and 7 wt.% PIBSA dispersant.	128
Figure 4.10.	Nanoindentation profiles of ZDDP tribofilms prepared from 40 min of rubbing in the presence and absence of PIBSA dispersant.	130
Figure 4.11.	Nanoindentation profiles of stainless steel and different regions of a ZDDP tribofilm prepared in a blend consisting of 1.5 wt.% ZDDP + 7.0 wt.% PIBSA dispersant rubbed for 40 min	132
Figure 5.1.	Cross sectional schematic of the valve train assembly of a combustion engine showing the relative position of the rocker arm in relation to the cam.	138
Figure 5.2.	Photographs of the crosshead bridges removed from a heavy duty diesel engine.	141
Figure 5.3.	Topographic SFM images of the center region of the intake crosshead bridge.	143

Figure 5.4.	Topographic $1 \times 1 \mu\text{m}$ SFM images of the center region of the intake crosshead bridge. Panel A represents the topography of the bottom of the pits and panel B represents the terraces.	144
Figure 5.5.	SEM images of the center region of the intake crosshead bridge. The terrace and pit regions are as marked.	146
Figure 5.6.	EDX spectra of the intake crosshead obtained from the terraces and the pits as marked in Figure 5.4B.	147
Figure 5.7.	Nanoindentation profiles of a steel coupon (curve A), the terrace region of the intake crosshead bridge (curve B), a 3 h thermooxidative ZDDP film (curve C), and the pit region of the intake crosshead bridge (curve D).	150
Figure 5.8.	SEM images from the edge of the exhaust crosshead bridge. The light regions are the steel alloy used to manufacture the component and the dark regions a surface film.	153
Figure 5.9.	EDX spectrum of the film material at edge of the wear scar on the exhaust crosshead bridge.	154
Figure 5.10.	Topographic SFM images of the edge region of the exhaust crosshead bridge.	155
Figure 5.11.	Nanoindentation profiles of the film region from the exhaust crosshead bridge (curve A), and a 2 h tribofilm prepared in a Cameron - Plint wear tester (curve B).	157
Figure 5.12.	Nanoindentation profiles from different spots along the edge of exhaust crosshead bridge.	159
Figure 7.1.	(A) Cyclic voltammetry of a freshly cleaved HOPG electrode in 1.0 M H_2SO_4 . (B) Cyclic voltammetry of CVD Pt on HOPG in 1.0 M H_2SO_4 . Both curves represent the first cycle of the potential sweep from 1.2 to 0.0 V vs. CHE at a scan rate of 1 V/sec.	179
Figure 7.2.	Topographic TM SFM images of freshly cleaved HOPG and Pt deposited on HOPG by CVD. The arrows highlight 10 nm high nanowires that bridge Pt particles.	181
Figure 7.3.	Possible nucleation mechanism for the CVD of $\text{Pt}(\text{COD})(\text{CH}_3)_2$ on the edge plane sites of HOPG.	183

Figure 7.4. Topographic $8 \times 8 \mu\text{m}$ TM SFM image of Pt deposited on HOPG by CVD.

185

List of Symbols

A	Area of contact between indenter and sample
A_s	Imaging amplitude in tapping mode scanning force microscopy
A_o	Free oscillating amplitude
B	Empirical fitting parameter for calculating elastic modulus
C	Empirical constant of a polynomial area function
D	Combined tip – sample deformation in a Hertz fit
E	Elastic modulus (Young's modulus)
E_r	Reduced elastic modulus
E*	Indentation modulus
ε	Geometric constant for indenter shapes
F	Force normal to plane of substrate
F_{max}	Maximum indentation force normal to substrate
f	Frictional force
G	Shear modulus
H	Hardness
h	Indentation depth at any point along an nanoindentation profile
h_c	Real contact depth in a nanoindentation at maximum force
h_f	Depth of impression left in surface after an indent
h_{max}	Maximum indentation depth at maximum force
h_s	Displacement of surface at the perimeter of contact
i	Indenter

k	Probability of generating a wear particle from a shearing event
m	Empirical fitting parameter for calculating the elastic modulus
P_o	Yield pressure
Q	Wear rate
R	Radius of curvature of a probe tip
R.H.	Rockwell Hardness
r_{sp}	Ratio of imaging to free amplitude of an oscillating cantilever
S	Slope or sliding velocity
s	Sample or substrate
μ	Coefficient of friction
v	Poisson's ratio

List of Abbreviations

AES	Auger electron spectroscopy
CHE	Convenient hydrogen electrode
COD	1, 5 - Cyclooctadiene
C_p	Cyclopentadiene
C – P	Cameron – Plint wear tester
CV	Cyclic voltammetry
CVD	Chemical vapor deposition
E – bridge	Exhaust rocker arm bridge
EDX	Energy dispersive X-ray spectroscopy
EHC 45	Base stock petroleum oil (< 0.03 % sulfur content)
EP	Extreme pressure additive
EPMA	Electron probe microanalysis
EXAFS	Extended X-ray absorption fine structure
FMM	Force modulation microscopy
GPa	Giga Pascal
HOPG	Highly ordered pyrolytic graphite
I – bridge	Intake rocker arm bridge
IFM	Interfacial force microscopy
IR	Infrared
IRRAS	Infrared reflectance absorbance spectroscopy
LFM	Lateral force microscopy

MCT 10	Base stock petroleum oil (> 0.03 % sulfur content)
PIBSA	Polyisobutenyl succinic anhydride polyamine
PPM	Parts per million
RMS	Root mean square roughness
SEM	Scanning electron microscopy
SFA	Surface force apparatus
SFM	Scanning force microscopy
SPM	Scanning probe microscopy
TBN	Total base number
TEM	Transmission electron microscopy
TM SFM	Tapping mode scanning force microscopy
TOF-SIMS	Time of flight secondary ion mass spectrometry
UHV	Ultra high vacuum
XANES	X-ray absorption near edge spectroscopy
XPS	X-ray photoelectron spectroscopy
XRF	X-ray fluorescence
ZDDP	Zinc dialkyl dithiophosphate

Chapter I

Synopsis and Introduction

General Introduction

The Encyclopedia of Tribology defines tribology as, "The science and technology of interacting surfaces in relative motion encompassing friction, wear and lubrication"[1]. Coined in 1966 from the Greek words tribos and tribein meaning "to rub", tribology is literally the study of "rubbing" [2, 3]. Tribology now extends to many disciplines of science and engineering such as mechanical, metallurgical, and chemical engineering as well as physics, chemistry, and biology. A plethora of new terms have now evolved from the root word "tribo" that imply some aspect of tribology such as tribochemistry, tribophysics, tribomechanics, biotribology, triboelectricity, tribofilms, tribooxidation, tribometer, and tribosystem [1]. Of the three phenomena that concern tribology, friction was the first to be studied methodically, such that as early as the eighteenth century empirical laws of friction were formulated by Amonton and Coulomb [2, 4]. On the other hand the study of wear and lubrication became more important as advancements in technology, such as the inception of the combustion engine demanded high material strength and durability.

This thesis is a compilation of results obtained from series of studies that were undertaken to explore on the microscopic scale the formation, structure, and mechanical properties of thin film coatings derived from Zinc dialkyl dithiophosphate (ZDDP) compounds. These compounds are common additives of commercial engine oil formulations and decompose in the crankcase of the

engine to deposit a protective film at the interface of highly stressed junctions. The results of these investigations will be presented in Chapters II – V. We begin with the study of “thermal” ZDDP films formed from the thermooxidative decomposition of ZDDP in a static oil bath (Chapter II). Chapters III and IV investigate ZDDP “tribofilms” that were prepared in a bench top wear tester machine. In Chapter V the investigations conclude with the study of components that have been removed from automotive engines.

This Chapter introduces the concepts of friction, wear, and lubrication, followed by an examination of engine oil chemistry with emphasis on the antiwear agent ZDDP, and concludes with a discussion of the main techniques that have been employed throughout this research.

Friction and Wear

Friction in its simplest terms is the resistance to motion encountered when one substance slides over another. Empirically the friction force obeys two fundamental laws first described by Amonton in 1699. The first law states that the friction force is proportional to the normal force between two bodies in contact and is expressed through Eq. (1.0) as,

$$f = \mu F \quad 1.0$$

where f is the frictional force, μ is the coefficient of friction and F is the normal force. The equation holds for both static and dynamic contact with the difference being the magnitude of μ . The second law states that the friction force is

independent of the macroscopic area of contact such that a rectangular block will experience the same frictional force when pulled on its front or on its side. The second law results from the microscopic surface topography of bodies that consists of an irregular network of peaks (asperities) and valleys [2, 4].

Wear is also a consequence of the inherent roughness in the surface topography of bodies on the microscopic scale. The exact definition of wear varies among the different disciplines, but is generally agreed on as, “the loss of material from a substance brought about by mechanical action of an opposing body” [2, 5-8]. A number of mechanisms have been proposed to explain why material is lost from a surface when it is in sliding contact. The mechanism that best describes automotive engine wear is the adhesive theory of wear [2], as first put forth by Bowden and Tabor [9] and later advanced by Burwell and Strang [10]. The adhesive theory of wear states that regions of high local pressure form when opposing surfaces are brought together [9, 10]. This is better illustrated in Figure 1.1, where the interfacial region of two blocks in mechanical contact is magnified to illustrate the microscopic roughness of the surfaces and to show the formation of junctions as the asperities come into contact. Upon initial contact the asperities deform elastically until the yield point of the material is exceeded, beyond which the deformation becomes both elastic and plastic. Elastic deformation implies that no energy is lost and the material returns to its original shape and configuration when the load is removed whereas in a plastic deformation the material is permanently deformed. The adhesive theory of wear states that when the deformation becomes highly plastic, material from one

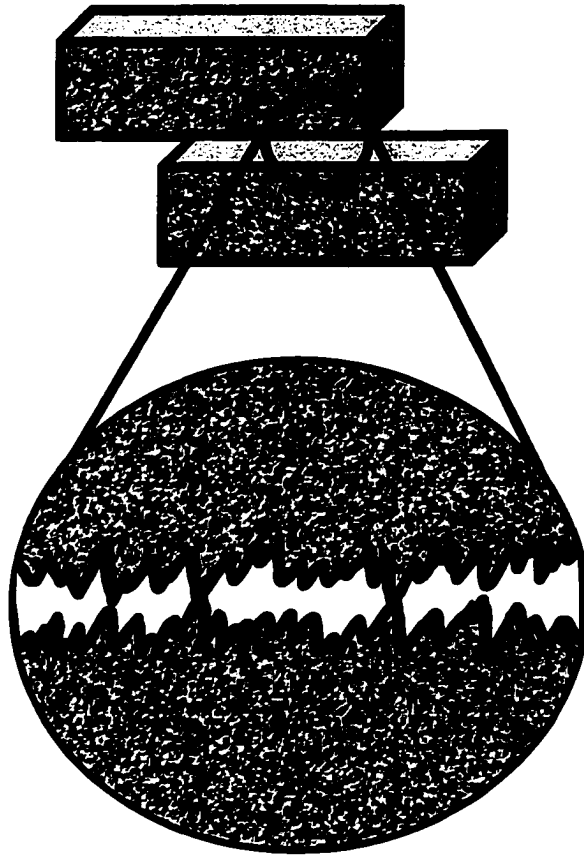


Figure 1.1. Microscopic view of the interfacial regions between two sliding blocks illustrating the inherent roughness in the surface topography.

surface flows into the other and “cold welds” to form a junction [2]. The continuous sliding causes the junctions to shear, displacing material from the surfaces that either adheres to the opposing surface or detaches to become wear particles. The wear particles then act as an abrasive and remove further material from the surface.

Empirically the wear rate is a function of the normal load (F) between the surfaces, the distance of sliding (S), and the yield pressure of the material (P_0). These variables were combined by Archard [11] to express the wear volume, Q, as:

$$Q = k \frac{FS}{3P_0} \quad 1.2$$

The constant, k, is the probability that a wear particle will be generated from a shearing event and was included to account for the fact that not all shearing events will yield a wear particle. The value of k depends very much on the geometry and surface topography of contact. It is generally about 0.001 for steel on steel contact [2], meaning that one in a thousand shearing events will lead to a wear particle.

The protection of mechanical equipment from wear is of significant economic interest. For example it was estimated that up to half of a percent of the gross domestic product of industrialized countries goes to replacing machinery that has lost compliance due to mechanical wear [2]. However in a time of conservation, the idea of simply replacing large machinery is not feasible and alternative approaches must be explored to minimize wear damage and

maximize the operational lifetime of mechanical equipment. Strategies to control wear include: (i) Engineering geometric contacts that reduce the effective load on components; (ii) Coating the surface with a hard metal or ceramic in the form of a hardness coating; (iii) Using lubricants to interpose an interfacial film between the substrates to prevent metal contact altogether. As for automotive engine wear, the method of a hardness coating is not feasible both for economic reasons and also because a mild degree of wear is desired initially for components to mate, a process commonly known as, "breaking in". The engineering approach is possible but with obvious design limitations. For example there will always be contact along the valve train of the engine to control the intake and exhaust cycles of the combustion process and hence wear will be inevitable. Thus lubrication is the only practical means of controlling engine wear and lubricant formulations are continuously being developed and refined to satisfy the demands of ever increasing engine power outputs. The lubrication and additive industry in North America is in excess of 5 billion dollars annually as can be expected from the enormous demands on transportation from which stems a large research initiative with most major oil companies devoting much resources to lubrication research.

Lubrication of Mechanical Systems

Oils and greases have been utilized throughout history to reduce friction. The modern period of lubrication started with the classical work of Osborne Reynolds on the tribological behavior of shafts and bearings in locomotives [4].

Reynolds showed that the inherent viscosity of liquids causes the formation of a fluid film near the contact zone. This film effectively separates the components from making contact - a condition that is known as hydrodynamic lubrication.

The entrapped film produces a hydrodynamic pressure that withstands and counters the load between the components. Although the exact solution of Reynolds' equation is beyond the scope of this work, for planar sliding contact, the hydrodynamic pressure and film thickness are a function of the viscosity of the lubricant, the load between the components, and the tangential sliding velocity. The hydrodynamic film collapses if the load becomes exceedingly high or the sliding velocity is insufficiently low or if the lubricant undergoes large viscosity changes. Boundary lubrication is then defined by the collapse of the hydrodynamic film whereby the surfaces are free to make contact.

Empirically the transition from hydrodynamic to boundary lubrication is marked by an increase in the wear rate. This behavior is represented graphically in Figure 1.2 where the hypothetical wear rate is plotted against the load and the sliding velocity for a sliding geometry such as that illustrated in Figure 1.3. Under the conditions of low load or high sliding velocity the lubrication is completely hydrodynamic and the wear rate is negligibly small (theoretically zero) since there is no direct metal to metal contact. Also the friction coefficient is less than 0.001 and the only mode of energy dissipation is shearing of the fluid film [4]. With an increase in load or a decrease in the sliding velocity, the lubricating film begins to collapse and asperities from the opposing surfaces come into contact resulting in a substantial increase in the wear rate. This is marked by the

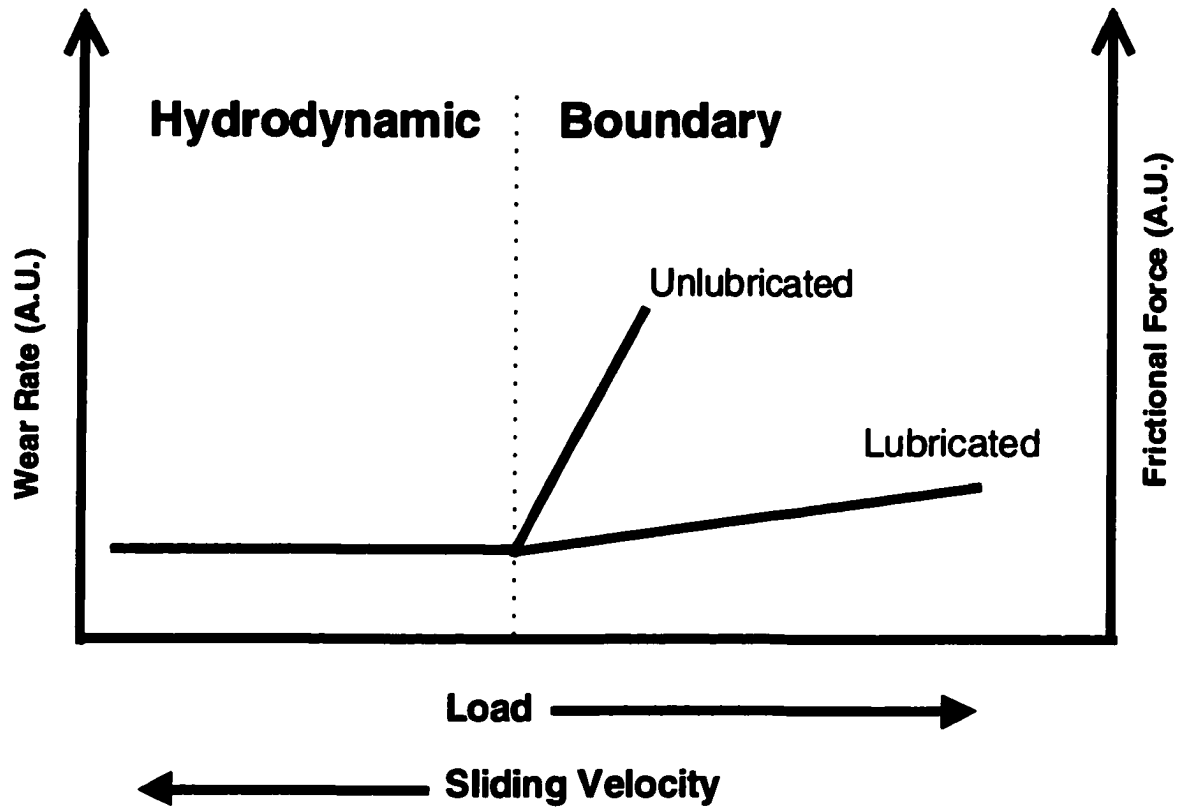


Figure 1.2. Hypothetical wear rate and frictional force as a function of load and sliding velocity for planar lubricated contact.

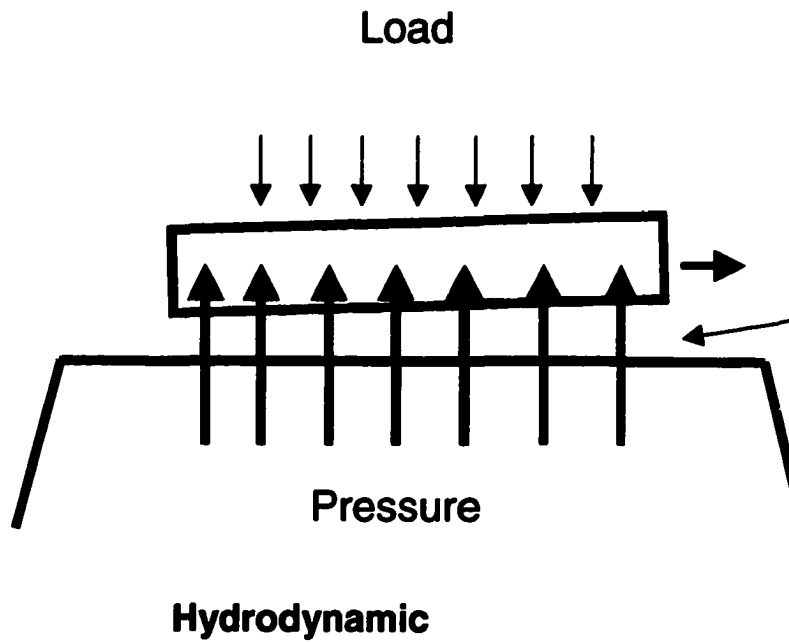


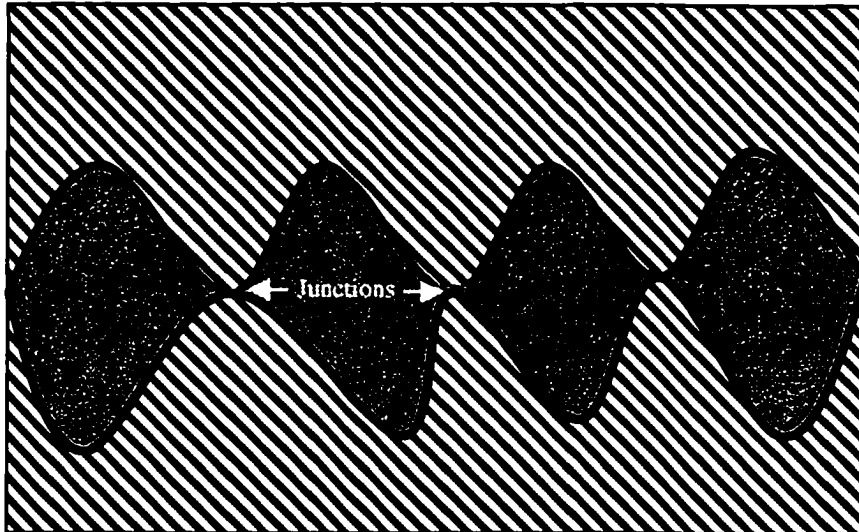
Figure 1.3. Hydrodynamic lubrication in planar sliding contact by the formation of an interposed fluid film.

transition point in the plot of Figure 1.2. Notably the friction coefficient increase two orders of magnitude ($\mu = 0.1$) leading to an increase in the frictional force as asperities make contact [4]. This situation is illustrated in Figure 1.4 where a conceptual microscopic view of the interfacial region highlights the formation of metal junctions that upon shearing will result in material loss.

The main function of engine oil formulations is to prevent metal contact in both hydrodynamic and boundary regimes and to help preserve components from wearing. The next section will give an overview of the composition and function of modern automotive engine oil formulations in providing lubrication to critical parts of internal combustion engines.

Engine Oil Formulations

Automotive engine oils must perform the following functions: (i) reduce friction and wear by imposing a hydrodynamic or boundary film between the moving parts; (ii) remove and suspend harmful by products of combustion from the crankcase; (iii) prevent oxidation and corrosion of the rubbing metal surfaces; (iv) dissipate heat from critical regions of the engine [12]. Engine oils are composed of a wide range of chemical additives blended in a base stock oil. Base stocks are high molecular weight refined extracts of crude oil that may consist of millions of different organic compounds. They are classified as paraffinic, naphthenic, or intermediate. This classification scheme infers the relative proportion of straight or branched hydrocarbons to aromatic hydrocarbons. The structure of several classes of organic compounds



Boundary Lubrication

Figure 1.4. Microscopic view of the interfacial contact region showing the formation of junctions due to adhesion during boundary lubrication.

that typically constitute the base lubricant is shown in the Figure 1.5. The final lubricant formulation is a blend of highly specific additives with a concentration of up to 5 weight percent in the base oil [13]. The additives serve to maintain the lubricating properties of the oil or they may serve an entirely separate function such as antiwear action. Table 1.1 lists some of the most common additives along with typical compounds and their function. For example pour-point depressants and viscosity index improvers play a role in maintaining the viscosity and rheological properties of the oil. This is important because of the strong viscosity dependence on hydrodynamic lubrication. Detergents and dispersants function to isolate contaminants such as carbon, soot, and sludge by keeping them in suspension through the formation of micelles. They are also responsible for removing moisture and neutralizing harmful acids. Antioxidants are important because base oils are susceptible to oxidation at high temperature where the oil acidifies and forms sludge. The effect of oxidation is undesirable because of changes in the viscosity of the oil [12]. Referring to Scheme 1, oxidation initiates with the formation of an alkyl radical ($R\bullet$) through homolytic cleavage of a carbon hydrogen bond. The alkyl radicals are further oxidized to form a peroxy radical ($ROO\bullet$) that can further abstract a hydrogen from an alkyl group and form a second radical $R\bullet$ and $ROOH$ [12].

Antiwear additives are also key ingredients in lubrication oils and assist in protecting engine parts from wear during high loads [13, 14]. In gasoline engines the high speeds produce large stresses along cams and tappets, cam-followers, pushrods, and rocker arm bridges. These parts, collectively known as the valve

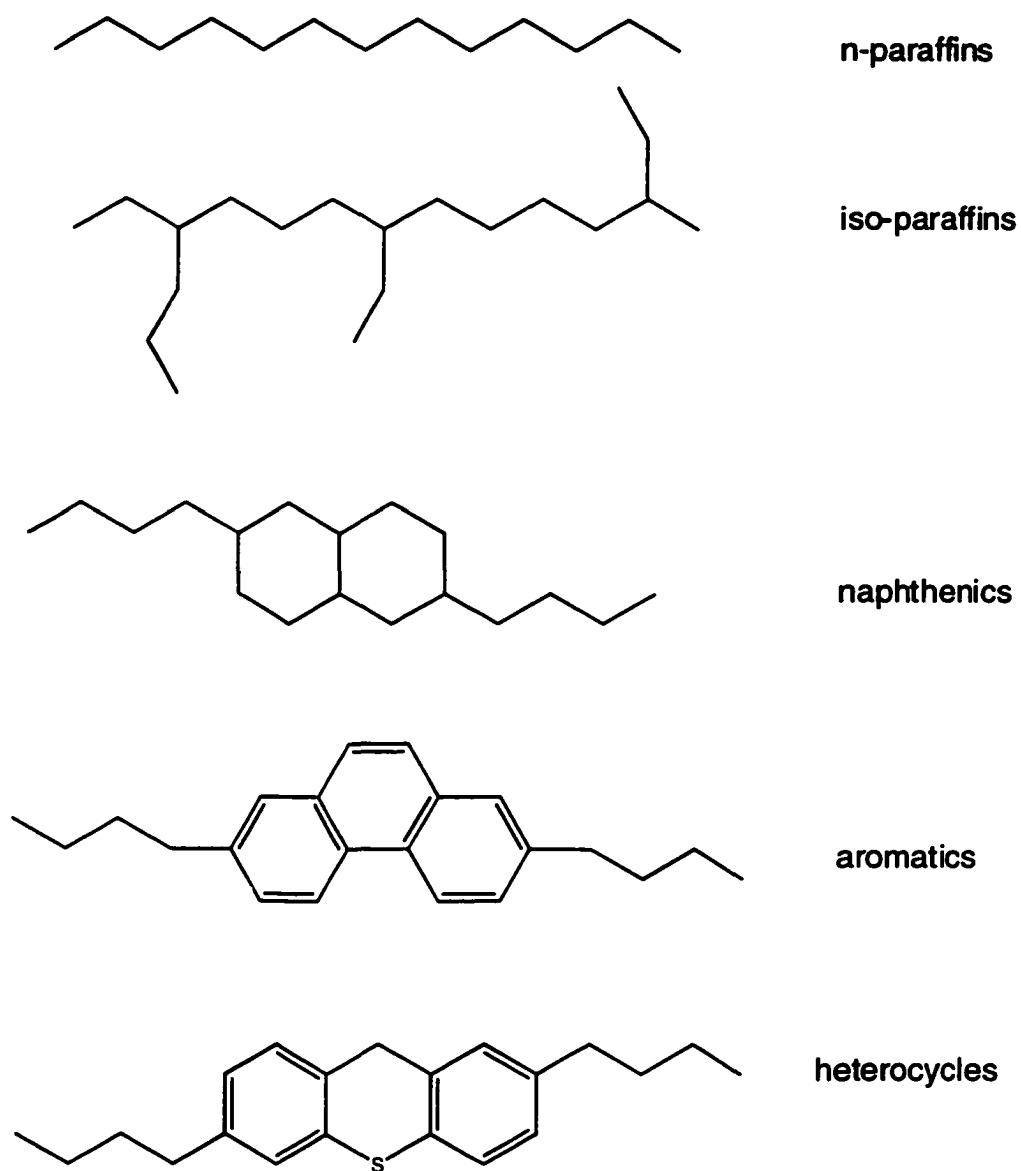
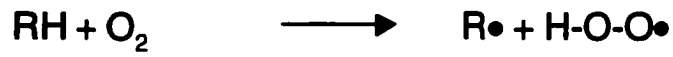
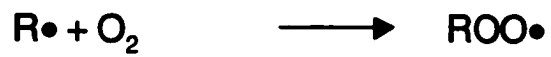


Figure 1.5. Composition of base stock extracts from crude petroleum oil.

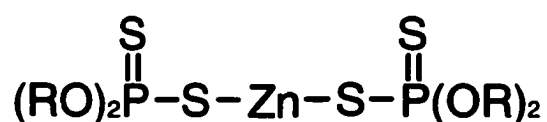
Table 1.1. Additives of Modern Automotive Lubrication Blends

Additive	Compounds	Function
Antiwear	Zinc dialkyl dithiophosphate, tricresylphosphate, organic phosphates, chloride compounds	Prevent wear by forming sacrificial antiwear films
Detergent and Dispersant	Succinimides, sulfonates, phenates, phosphates, amine compounds	Keep sludge, soot, and other carbon impurities in suspension
Rust Inhibitors	High base additives, sulfonates, phosphates, organic acids, esters	Prevents rust by forming protective thin film coating
Friction Modifiers	Molybdenum disulfide	Reduce friction coefficient by forming solid lubricant film
Anti-foam agents	Silicone Polymers	Reduce foam in crankcase
Antioxidants	ZDDP, hindered phenols, nitrogen, sulfur compounds	Prevent oxidation of oil and formation of varnish, sludge
Viscosity Improvers	Polyisobutylene, methacrylate polymers	Reduce the dependence of viscosity on temperature
Alkaline compounds	Overbased metallic sulfonates and phenates	Neutralize acids and prevents corrosion of metal
Pour point depressants	Methacrylate polymers	Lower freezing point allow better flow at low temperatures

Initiation:**Propagation:**

Scheme 1. Initiation and propagation of oxidation of base oil.

train, operate in the boundary lubrication regime and must be lubricated constantly by antiwear agents. These agents typically form sacrificial films at the interface of sliding contacts and limit the adhesion between the surfaces to reduce the wear rate considerably. In Figure 1.6 the interfacial contact regime is illustrated to show how the antiwear film prevents asperity contact by interposing a film between the surfaces. One of the most common classes of compounds employed as antiwear agents are zinc dialkyldithiophosphates (ZDDP) of the general formula:



In this structure zinc is coordinated by two alkyldithiophosphate moieties through metal thiol bonds. Typically, R is a secondary alkyl group (e.g., *sec*-butyl) but can also be a primary alkyl or an aryl group. The antiwear activity of ZDDP is inversely proportional to thermal stability of the starting compound, which is dependent on the R group. Thermal stability of ZDDP increases with carbon number and in the order of aryl > primary alkyl > secondary alkyl. The wide popularity of ZDDP stems also from its ease of synthesis that consists of the reaction of an alcohol with phosphorus pentasulfide to give dialkyldithiophosphoric acid. Subsequent neutralization with ZnO yields ZDDP. The original motivation for using Zn as the cation was likely its negative reduction potential to counter oxidation of the oil. In practice, a mixture of different ZDDP's may be added to oil depending on the application. For example in hotter running engines it will be better to have more primary alkyls than secondary whereas the reverse will be

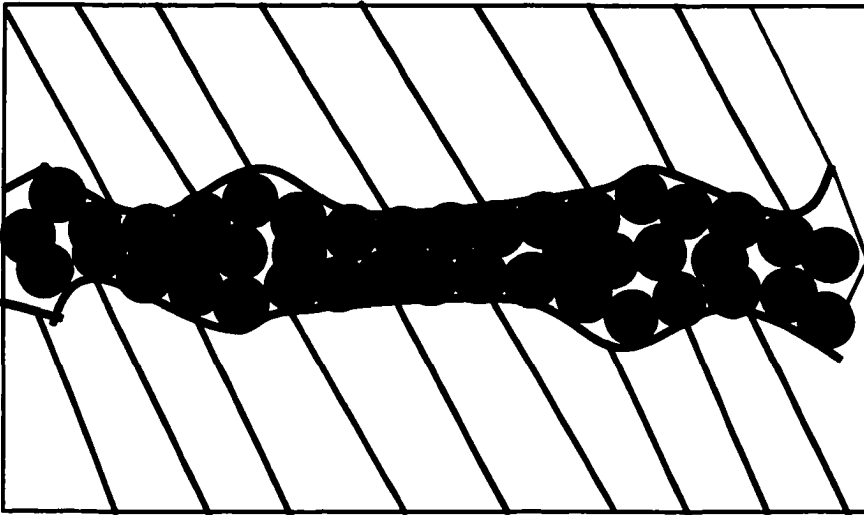


Figure 1.6. Microscopic view of the interfacial region between opposing bodies showing how an antiwear film may prevent asperity contact.

true for colder running engines. However a main concern of using ZDDP is that phosphorus is known to poison catalytic converters. Therefore environmental regulations limit the amount of ZDDP that may be present in the formulation.

Studies of Boundary Films of ZDDP

The first boundary lubricants were organic amines, alcohols and esters because they exhibited strong adhesion to the surface, formed compact monolayers, and had low shear strength so as to minimize frictional losses [4]. However as engine power and operating temperatures increased organic additives became ineffective in controlling wear because of thermal degradation and a series of new compounds were developed that included organic phosphates, dithiophosphates, dithiocarbonates, and culminated in 1941 with the development of ZDDP by Lubrizol [13]. Initially added at low concentrations as an antioxidant, it was soon realized that ZDDP can also provide remarkable antiwear activity and is now the exclusive antiwear agent (present in part per million) in most automotive lubrication blends. The antiwear mechanism and chemical composition of the antiwear films has been and remains the subject of numerous studies in the area of tribology.

Various surface analysis techniques have been employed in investigating the chemical composition and tribological properties of ZDDP. Experimentally, the films are prepared in reciprocating wear testers that are designed to simulate the geometry and contact pressure that components in the valve and powertrain of an automotive engine experience. Some of the more common types of wear

testers include 4 – ball wear testers, cam and tappet assemblies, and Cameron – Plint wear rigs. The number of papers devoted to the study of the boundary films of ZDDP is vast and most describe the application of two or more techniques to the analysis. Here only a brief overview of some of the more important contributions will be given, grouped in terms of the techniques that were employed in the studies.

Some of the initial elemental analyses were performed by Rounds who employed X-ray fluorescence (XRF) to detect mainly Zn, P, and S on the surface of a 4 – ball wear tester that had been run in blends containing several different ZDDPs [15]. These results were further corroborated using techniques such as electron probe microanalysis (EPMA) and energy dispersive X-ray (EDX) in the work of Sheasby et al. in a reciprocating wear tester who reported large quantities of Zn, P, S, and O on the surface corresponding to the starting ZDDP material [16]. While the above techniques were element specific, techniques such as X-ray photoelectron spectroscopy (XPS) and Auger electron spectroscopy (AES) have dominated recent analyses because of their superior ability to provide both elemental and chemical information such as oxidation state and valency. As well, sputter techniques in concert with AES, have provided elemental depth profiles of films. The initial XPS work of Bird and Galvin confirmed that the films are rich in Zn, P, S, O, Fe, and from the binding energy of P and S concluded the presence of phosphates and sulfides on the surface [17]. Later XPS analysis by Spedding and Watkin confirmed the presence of phosphates but went further to suggest that Zn is bonded to P and not to S [18,

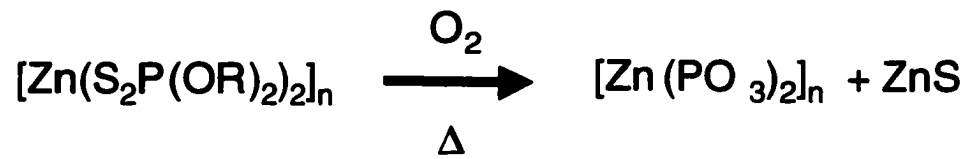
19]. The studies of Jahanmir concluded that the films are primarily composed of zinc polyphosphates and iron sulfide [20], while the *in - situ* AES work of Glaeser et al. suggested that the films are composed of a layered structure where a phosphate layer overlays a thin sulfide layer chemisorbed to the substrate [21].

Infrared reflectance spectroscopy has also been used extensively to probe the structure of the films. In the work of Harrison et al. the major bands in the infrared spectra of films formed from several ZDDP compounds were assigned to the P-O-P, P=O, and P-O-C, functionalities [22]. In several papers on films formed in a lubricated cam and tappet, Willermet et al. employed infrared analysis in conjunction with AES and XPS to conclude that the films are inorganic amorphous polyphosphate materials such as orthophosphate (PO_4^{3-}) and pyrophosphate ($\text{P}_2\text{O}_7^{4-}$) associated with Zn and proposed a model for the transformation of ZDDP to the antiwear film [23-25]. The films have also been analyzed by mass spectrometric techniques. For example time of flight – secondary ion mass spectrometry (TOF-SIMS) was employed to study films formed in a Cameron-Plint wear rig. The results suggested the presence of long chain polyphosphate on the surface with an O to P ratio of 5 to 2 [26, 27]. Other techniques that have been utilized in the study of ZDDP include extended X-ray absorption fine structure (EXAFS) spectroscopy [28, 29], ellipsometry [30, 31], and electric contact resistance [32].

Much of the recent developments and insight about the nature of ZDDP films has come from the application of synchrotron radiation to probe the X-ray absorption near edge structure (XANES) of the elements constituting the films

[33-41]. XANES is the study of electronic transition from the core levels to unoccupied levels and has proven to be a sensitive technique to the speciation of the films. Advantages of synchrotron XANES include: high sensitivity to the chemical environment of the atom; high power density to analyze minute amounts of material; and the ability to probe both the surface and bulk characteristics of a material by collecting electron and fluorescence yields respectively. The initial work of Yin et al. compared the XANES spectra of the antiwear films with several model compounds [33]. This was followed by a series of other reports that investigated the effect of physical parameters such as sliding speed, temperature, and time on the chemistry of the films [37]. XANES was also utilized as a means to quantify the chain length of the polyphosphates [37].

The combined results of these studies have led to a mechanism for the formation of the antiwear film from the ZDDP precursor. This mechanism is presented in Scheme 2 and consists of: (i) Adsorption of ZDDP from the solution phase on to the surface; (ii) Thermooxidative decomposition of the surface bound ZDDP's to form long chain polyphosphates in a polymerization reaction; and (iii) Reaction of the long-chain polyphosphates with iron oxide moieties to form short-chain polyphosphates. An idealized model representing the final structure of the films is shown in Figure 1.7 where the phosphate moieties are bound to iron oxides on the surface and Zn is either present as ZnS or remains associated with the phosphate. An important note is that it is not clear whether ZDDP is intact or partially decomposed in the initial adsorption step. This is because the polymerization of ZDDP to polyphosphates can also occur by thermal



Scheme 2. The mechanism of antiwear film formation from ZDDP.

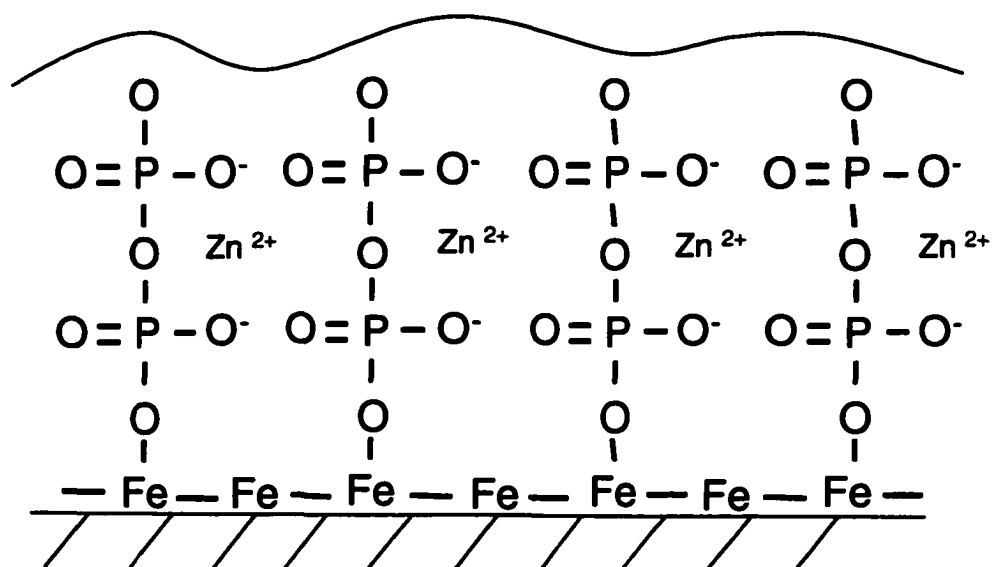


Figure 1.7. An idealized model of the ZDDP derived polyphosphate antiwear film chemisorbed to iron oxide moieties on a steel substrate.

decomposition of ZDDP in a static oil bath and does not require tribological contact [36]. Thus it is quite possible that the first step is adsorption of thermal decomposition products of ZDDP, such as long-chain polyphosphates, that are then converted to shorter chain polyphosphates by rubbing of the metal parts. My studies of the evolution of films formed from the thermal decomposition of ZDDP [42] will be discussed in Chapter II.

The effects of physical properties on the antiwear films of ZDDP have also been explored. For example, it was shown that temperature directly affects the rate of decomposition, [43-47] thickness, and antiwear performance of the films [16, 31]. The effect of concentration has also been studied in detail. It was found that higher concentrations resulted in higher rates of decomposition [44, 46, 48, 49] and better antiwear performance [50, 51]. The effects of load, surface roughness, and sliding speed have also been investigated [16, 20, 21, 52-54]. The conclusions from these studies are: (i) Film thickness increases up to a maximum load of 600 N, but decreases with higher loads; (ii) Films take longer to form on rough surfaces; and (iii) Films form more rapidly as the sliding velocity is increased.

Techniques Utilized in this Work

As stated previously, the focus of this work is to gain deeper insights into the formation, structure, and performance of antiwear films formed from the decomposition of ZDDP compounds. These insights will develop from microscopic, spectroscopic, and nanoindentation analysis. Scanning force microscopy (SFM) and scanning electron microscopy (SEM) will be utilized to study the morphology of the films. This will be complemented by elemental and structural analysis through energy dispersive X-ray (EDX) analysis, and infrared reflectance absorbance spectroscopy (IRRAS). Finally, nanoindentation experiments will evaluate the mechanical properties of the films at sub micrometer spatial resolution. Herein we will discuss in detail SFM and nanoindentation techniques. Discussion of IRRAS and EDX will be left for Chapters II and III.

Scanning Probe Microscopy

The family of techniques known collectively as scanning probe microscopy (SPM) originated with the development of scanning tunneling microscopy (STM) by Binnig and Rohrer [55]. In STM, the tunneling current sensed between a tip and sample is used to map the topography of a surface. The main limitation of the STM technique however is that the tip and sample must be conductive. This limitation was overcome several years later with the development of the scanning force microscope (SFM) by Binnig, Quate, and Gerber [56]. In SFM the physical phenomenon of force is used to image a surface as opposed to tunneling current.

Today SFM has become a vital tool in the study of tribology. Friction, wear, and lubrication may be probed at microscopic length scales [57, 58]. In Figure 1.8 the basic setup of an SFM is illustrated, where a laser is focussed on to the back of a cantilever / tip assembly and reflected into a position sensitive photodetector. The sample is translated in the $x - y$ plane under a sharp probe tip with a radius of curvature of 30 nm or less. Topographic features on the surface induce a deflection of the cantilever normal to the surface that is detected by the top and bottom photodetectors. This deflection signal is used as a feedback signal to the piezoelectric actuator that extends or retracts to maintain a constant normal force between the tip and the sample. The voltage applied to the actuator is collected by a computer and is used to generate a pixel by pixel map of the surface topography. Similarly, the twisting of the cantilever can be used to map out the frictional forces between the tip and the sample by monitoring the differences between the left and right detectors. In the work presented here the SFM will be utilized solely in the topographic mode.

Nanoindentation and Nanomechanical Properties

The strength, durability, and effectiveness of coatings are related to the mechanical properties of the material constituting them. Mechanical properties are defined by parameters such as the elastic modulus (E) (also referred to as the Young's modulus), hardness (H), and yield pressure (P_o) [59]. The elastic modulus is a measure of a material's resistance to elastic deformation under an applied stress whereas hardness and yield pressure relate to plastic flow.

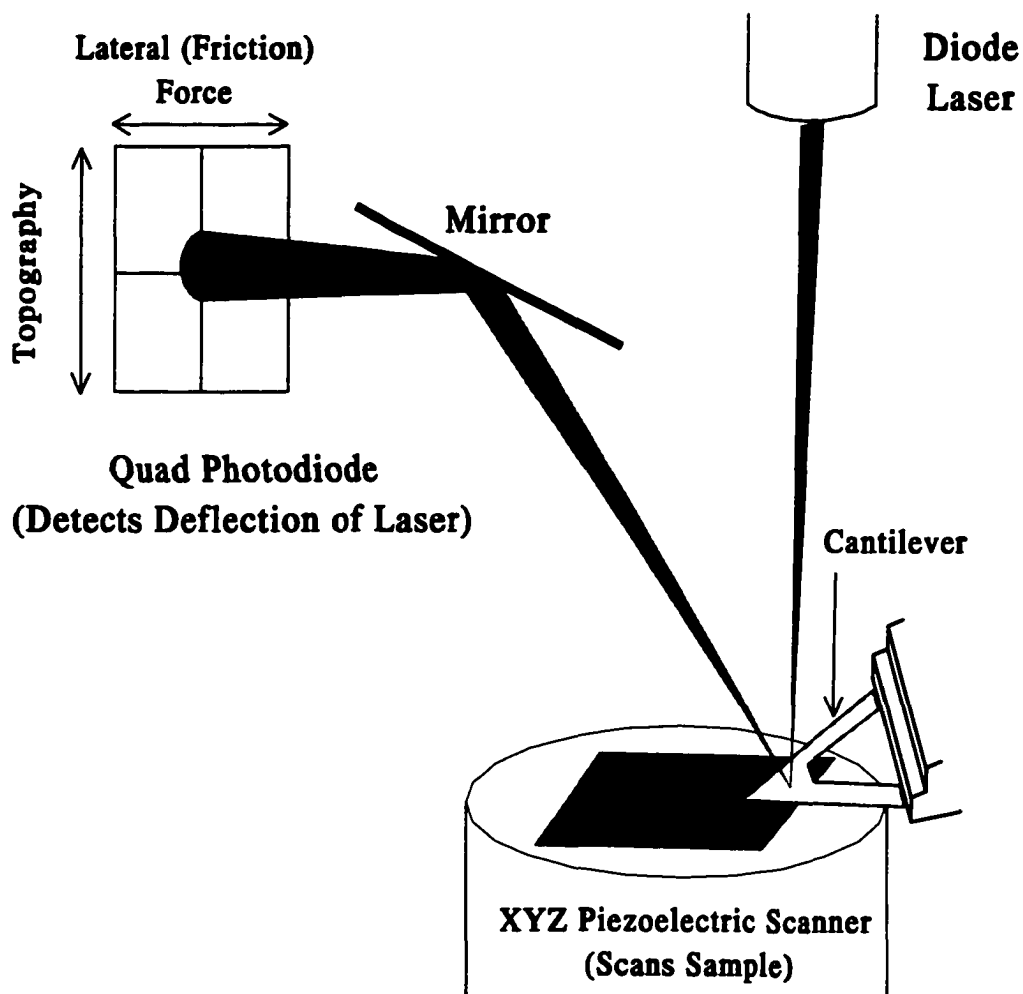


Figure 1.8. Diagram of a scanning force microscope with a reflection based detection system.

While E and H generally originate from macroscopic events, interests in nano – scale surface science and technology require that these parameters be measured at microscopic length scales [60]. This requirement has been satisfied with the development of nanoindentation instruments that are able to simultaneously measure force and indentation depth [60-64]. Nanoindentation has now become a common tool in the study of the nanotribology of polymers [65, 66], hardness coatings [67, 68], monolayer films [69], and semiconductors [70].

A nanoindentation experiment consists of indenting a material with a sharp tip through the application of load while simultaneously monitoring the depth to which the material is penetrated. Figure 1.9 illustrates the loading and unloading sequence of a tip penetrating a material up to some depth and then withdrawing. The maximum indentation depth, h_{max} , is the sum of the real contact depth, h_c , and the displacement of the surface at the perimeter of contact, h_s such that:

$$h_{max} = h_c + h_s \quad 1.3$$

The maximum indentation depth is equal to the combined tip - sample deformation and is easily attainable from the nanoindentation profile whereas h_s and h_c require more analysis as will be discussed later.

A number of designs have been implemented to accomplish the task of monitoring both the displacement and force simultaneously. All involve applying a force by means of an electromagnetic field and tracking the displacement through changes in the potential or capacitance between two plates. The

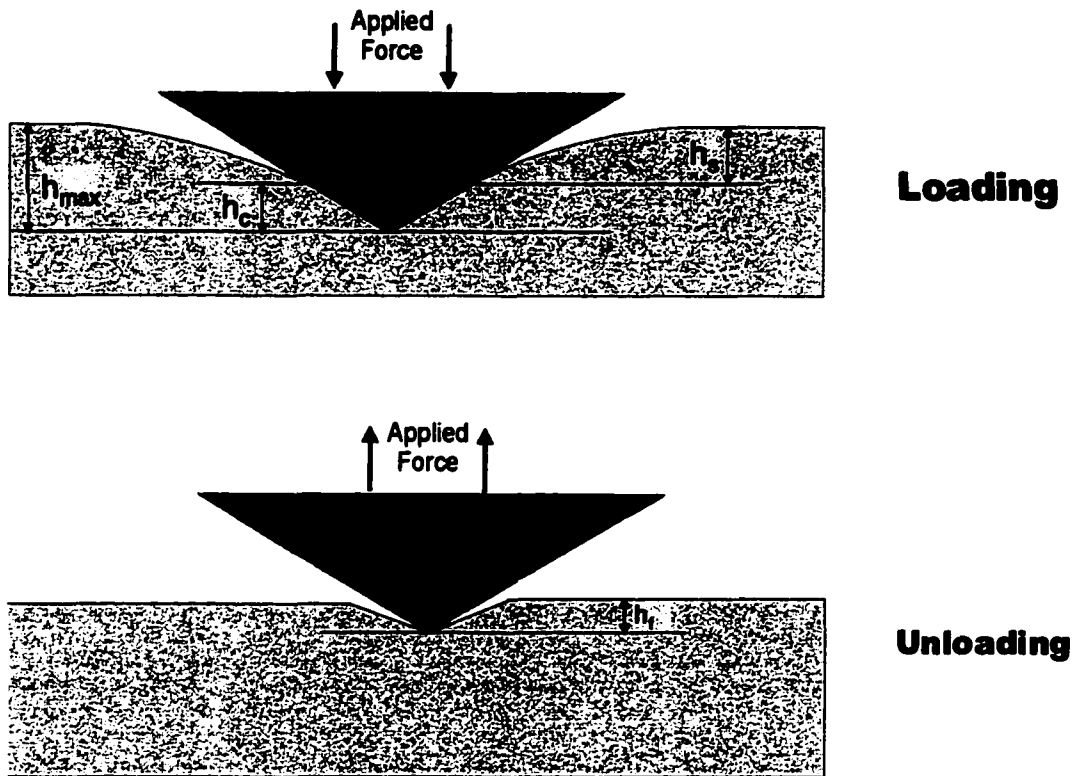


Figure 1.9. An illustration of the loading and unloading cycle of a triangular tip penetrating a surface. The maximum deformation (h_{max}) is the sum of the real contact depth (h_c) and the displacement of the surface at the perimeter of contact (h_s). The final depth (h_f) is equal to the depth of the permanent deformation left in the material after complete withdrawal of the tip.

specifics of the instrumentation used in this work will be discussed in Chapter III. Figure 1.10 shows some of the more common load functions in a nanoindentation. Generally the force is ramped in a linear fashion up to a maximum and reversed in a similar fashion to the origin. If the material creeps, a phenomenon where there is displacement in the absence of force, a trapezoid waveform is preferred where the force is held at the maximum for a small duration until the creeping subsides. Likewise, the trapezoid function is also utilized if the material exhibits viscoelastic behavior in the time frame of the experiment. The final nanoindentation profile consists of a loading and unloading portion that forms a closed loop such as the plot shown in Figure 1.11 for an isotropic material. The nanoindentation profile is a fingerprint of the material and more importantly can be used to calculate of E and H from continuum contact mechanics. The loading segment of the curve consists of both elastic and plastic components. In the unloading segment the elastic components are recovered and when the indenter is fully withdrawn, i.e. at $F=0$, the x-intercept corresponds to the permanent deformation left in the material.

The elastic modulus can be evaluated from the nanoindentation profile by two methods. The first method consists of fitting the initial segment of the loading cycle to the Hertz elastic model of an infinitely rigid parabolic indenter on a planar surface through the relationship:

$$F = \frac{4}{3} \sqrt{R} E_r h^{3/2} \quad 1.4$$

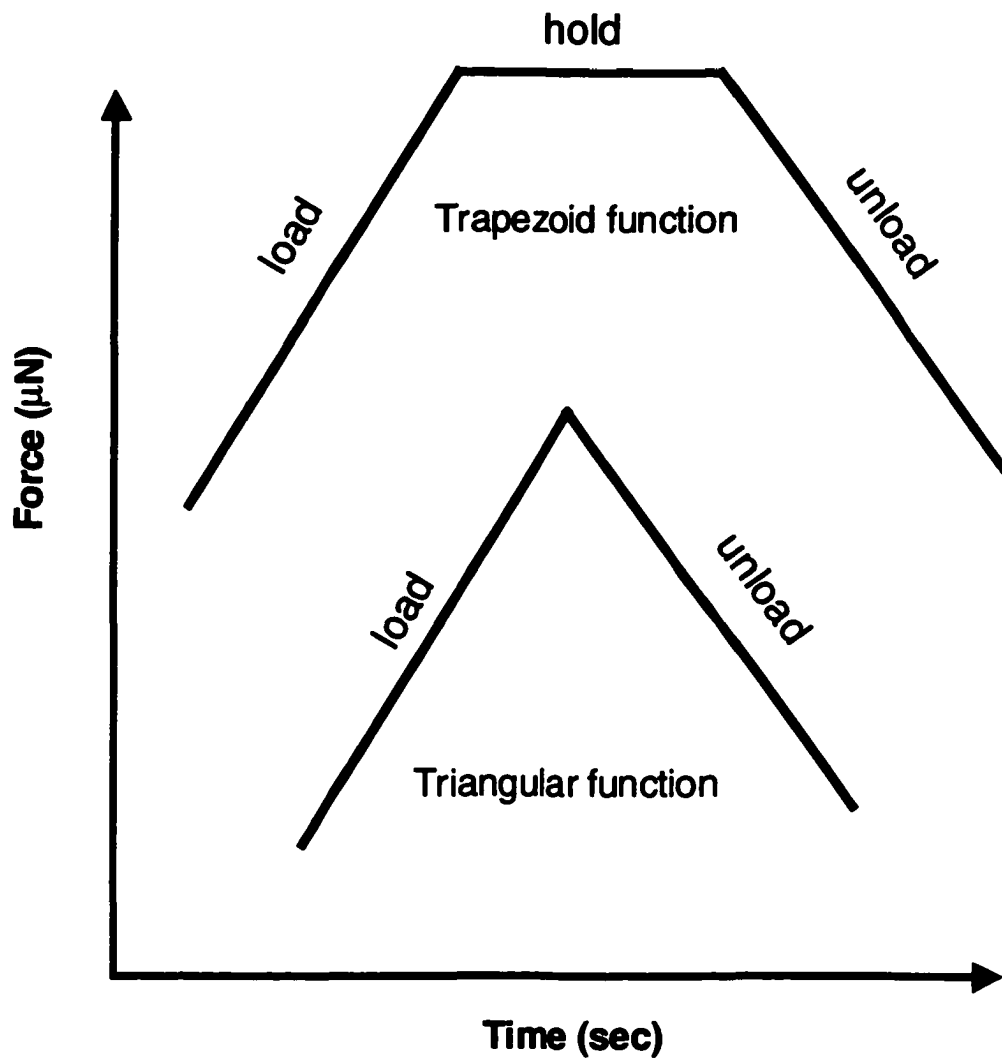


Figure 1.10. Load functions in a nanoindentation experiment. The trapezoid function is useful to dampen viscoelastic effects and creep on the nanoindentation profile.

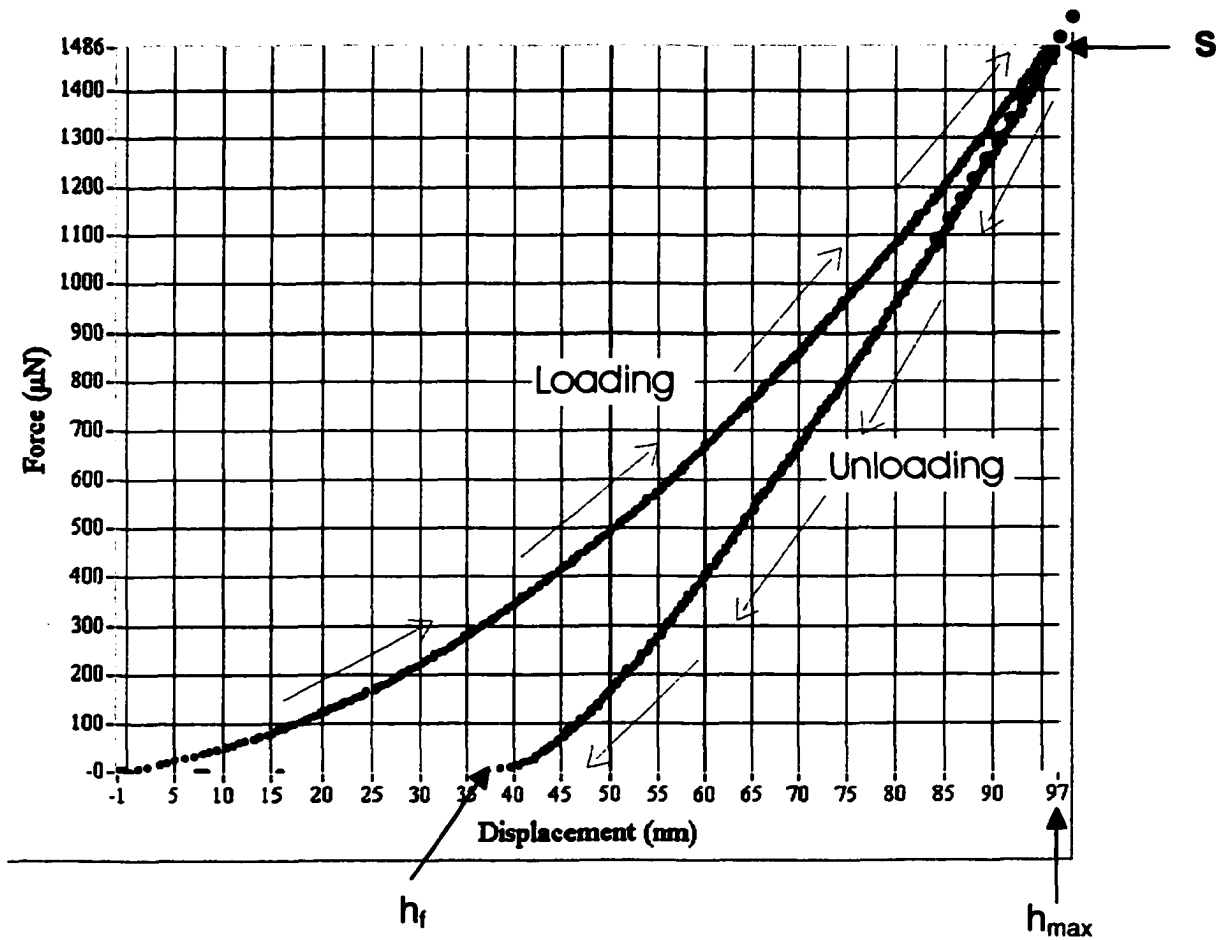


Figure 1.11. The complete nanoindentation profile of an isotropic material. The maximum indentation depth (h_{max}), the depth of the permanent deformation after tip withdrawal (h_f), and the slope (S), of the unloading portion of the curve are as marked.

F is the normal force, h is the indentation depth, R is the radius of curvature of the tip and E_r is the reduced elastic modulus given by,

$$\frac{1}{E_r} = \frac{(1-\nu_i^2)}{E_i} + \frac{(1-\nu_s^2)}{E_s} \quad 1.5$$

The subscripts i and s refer to the indenter and sample respectively, and ν is Poisson's ratio which is a ratio of the fractional change in the width to the length of a material under tension or load [59]. When ν is not known, as is often the case for thin films, it is sufficient to report the indentation modulus ($E^* = E_s / (1-\nu_s^2)$) as it is a very good estimate of the elastic modulus [63]. In practice the tip is made of a material of high elastic modulus such as diamond ($E = 1000$ GPa) such that the first term in Eq. (1.5) vanishes and E_r approaches the indentation modulus of the sample.

The elastic modulus may also be calculated from the unloading portion of a nanoindentation profile in what is known as the compliance method. The analysis first put forth by Doerner et al. and advanced by Oliver et al. [60, 63, 71] begins by fitting the unloading segment of the profile to the power law relation,

$$F = B(h - h_f)^m \quad 1.6$$

where F is the load, h is the indentation depth at any point during the unloading segment, h_f is the final depression left in the surface at zero force, and B and m are empirical fitting parameters. By differentiating Eq. (1.6) at the maximum

indentation depth, the slope S of the unloading curve at the onset of unloading becomes

$$S = \frac{dF}{dh} (h = h_{\max}) = mB(h_{\max} - h_f)^{m-1} \quad 1.7$$

The significance of determining the slope at the onset of unloading is that in the classic work of Sneddon [72] on elastic contact mechanics, the reduced modulus is proportional to S through,

$$E_r = \frac{\sqrt{\pi}}{2} \frac{S}{\sqrt{A_c}} \quad 1.8$$

where A_c is the real area of contact between the tip and sample at maximum load. The next part of the analysis is then to compute A_c from the real contact depth (h_c). This is empirically determined from an area function that is of the form:

$$A_c = C_0 h_c^2 + C_1 h_c + C_2 h_c^{1/2} + C_3 h_c^{1/4} \dots \dots \dots C_8 h_c^{1/128} \quad 1.9$$

C_1 through C_8 are constants and determined for a tip by making a series of indents into a standard material of known modulus. From the slope of the indentation profiles of the standard material, and using Eq. (1.8), the contact area (A_c) is determined for each indent. Similarly the real contact depth (h_c) is determined from Eq. (1.3) once h_{\max} and h_s are known. The maximum indentation depth (h_{\max}) can be obtained directly from the plot whereas the displacement of the surface at the perimeter of contact (h_s) is calculated by Eq. (1.10) below,

$$h_S = \epsilon \frac{F_{\max}}{S} \quad 1.10$$

Where F_{\max} is the maximum indentation force, S is the slope as before, and ϵ is a geometric constant that ranges from unity for a flat punch indenter to 0.72 for a conical indenter. The area function of the tip is then determined by fitting the values of A_c and h_c at each indentation depth to Eq. (1.9). Once the area function is determined for a tip, the reduced modulus of unknown samples can be readily computed. The procedure is then to simply calculate h_c and S from a nanoindentation profile of the unknown material and substitute these values into Eqs. (1.9 and 1.8) to calculate the reduced modulus.

The main advantage of using the unloading portion of the profile to calculate E_r is that the radius of curvature of the tip does not have to be known as it is accounted for by the area function. In the Hertz fit however, the radius of curvature must be known accurately. On the other hand the method of using the unloading portion has drawbacks in that effects such as material pile up can dramatically cause error in the real area of contact, while creeping will result in an overestimation of S [64, 71]. The elastic theory of Sneddon assumes that the material under the indenter sinks in during the indentation. Pile up occurs when material displaces around the perimeter of the indent instead of sinking in.

Hardness (H) is yet another parameter that describes a material's mechanical strength. In nanoindentation H is defined as the average pressure under the tip and is expressed in the form:

$$H = \frac{F_{\max}}{A_c} \quad 1.11$$

The main advantage of defining H in this way is that the indent does not have to be imaged as is done in traditional Vicker's and Moh's hardness tests [59]. The yield pressure (P_o) can also be determined once H is known, as it is equal to one third of H for most materials.

Thus nanoindentation is a powerful and convenient means of evaluating the mechanical strength of materials. Moreover, nanoindentation instruments are equipped with scanning probe capabilities allowing the evaluation of these parameters at nanometer resolution. This technique will be utilized extensively in Chapters III to V to examine the elastic and plastic properties of the antiwear films of ZDDP. The parameters will be calculated by analyzing the unloading portion of the curves through Eqs. (1.6 – 1.11).

Research Objectives

The primary objective of this project is to gain deeper insights into the formation, structure, and performance of antiwear films formed by the decomposition of ZDDP compounds. These insights will develop first from the analysis of films on a micrometer-scale with SFM and SEM. Nanoindentation analysis is then employed to probe the mechanical strength of the antiwear films at the microscopic scale, as this will be crucial in their ability to provide wear protection. In conjunction to scanning techniques, I will also utilize reflectance infrared spectroscopy and EDX analysis to probe the structural and elemental properties of the films.

My research approach consists of starting with simple experiments under controlled conditions and progressing to more complicated systems with the ultimate objective of predicting the behavior of ZDDP in a fully formulated engine oil. The first step will be to study the thermooxidative decomposition of ZDDP under static conditions. Thermooxidative decomposition is the primary step in the formation of ZDDP antiwear films over a surface. These studies will be presented in Chapter II where the morphology of films formed on Au substrates from the thermooxidative decomposition of ZDDP will be tracked with SFM. Au was used as the substrate for the films because it is relatively flat over large areas so as to limit the contribution of the substrate to the topography of the films.

While thermooxidative decomposition is the primary step in the formation of the antiwear film, ZDDP antiwear additives operate at the interface of mechanical contact between opposing bodies. The latter will influence both the mechanism of film formation and the properties of the films drastically. To investigate the effect of mechanical action on the properties of the films, samples were prepared in a wear tester where variables such as sliding speed, contact pressure, and oil temperature were controlled. The results of these studies will be presented in Chapter III where I will focus on the morphology and nanomechanical properties of the films as a function of rubbing time. In addition to the above I will also present SFM and nanoindentation results on the effect of soot impurities on the films and conclude with some preliminary results on the significance of sliding velocity on the morphology of the films.

Modern lubrication blends are composed of numerous chemical additives that are designed to function independently. However it has been found that certain additives impede the action of others. In Chapter IV I will study the effect of detergent and dispersants on the antiwear activity of ZDDP. Detergents and dispersant can chemically interact with ZDDP in the solution and as well affect the tribochemical properties of ZDDP derived antiwear films.

These investigations will culminate in Chapter V with analyses of engine components. The components include rocker arm bridges that have been removed from heavy duty diesel truck engines. These studies are the first of their kind and are aimed at developing SPM techniques as diagnostic tools for the study of engine components. These studies will also serve as a means to evaluate the validity of bench top experiments such as the C – P wear tester in providing insight about wear in an engine.

Reference:

1. C. Kajdas, S. S. K. Harvey, and E. Wilusz, Encyclopedia of Tribology, Elsevier, Amsterdam - Oxford - New York - Tokyo, 1990.
2. J. Halling, Principles of Tribology, Macmillan Press Ltd, London, 1975.
3. A. Dorinson and K. C. Ludema, Mechanics and Chemistry in Lubrication, 1985, Amsterdam, 1985.
4. F. P. Bowden and D. Tabor, Friction: An Introduction to Tribology, Anchor Press, New York, 1973.
5. P. J. Blau, Tribol. Int. 30:321 (1997).

6. T. L. Oberle, *J. Metals* June:438 (1951).
7. E. Rabinowicz, *Friction and Wear of Materials*, John Wiley and Sons, Inc., New York, 1965.
8. K. H. Zum Gahr, *Microstructure and wear of materials*, Elsevier, Amsterdam - Oxford - New York - Tokyo, 1987.
9. F. P. Bowden and D. Tabor, *Friction and Lubrication of Solids*, Oxford University Press, UK, 1950.
10. J. T. Burwell and C. D. Strang, *J. Appl. Phys.* 23:18 (1952).
11. J. F. Archard, *J. Appl. Phys.* 24:981 (1953).
12. S. Q. A. Rizvi, *Amer. Soc. Metals Handbook* 18:98 (1992).
13. A. Caines and R. Haycock, *Automotive Lubricants Reference Book*, Society of Automotive Engineers (SAE), 1996.
14. A. G. Papay, *Lubrication Sci* 10:209 (1998).
15. F. G. Rounds, *ASLE Trans.* 18:79 (1975).
16. J. S. Sheasby, T. A. Caughlin, A. G. Blahey, and K. F. Laycock, *Tribol. Int.* 23:301 (1990).
17. R. J. Bird and G. D. Galvin, *Wear* 37:143 (1976).
18. H. Spedding and R. C. Watkins, *Tribol. Int.* 15:9 (1982).
19. R. C. Watkins, *Tribol. Int.* 15:13 (1982).
20. S. Jahanmir, *J. Tribol.* 109:577 (1987).
21. W. A. Glaeser, D. Baer, and M. Engelhardt, *Wear* 162:132 (1993).
22. G. H. Harrison and P. Brown, *Wear* 148:123 (1991).

23. P. A. Willermet, J. M. Pieprzak, D. P. Dailey, R. O. Carter III, N. E. Lindsay, L. P. Hack, and J. E. de Vries, *ASME Trans.* 113:38 (1991).
24. P. A. Willermet, R. O. Carter, and E. N. Boulos, *Tribol. Int.* 25:371 (1992).
25. P. A. Willermet, D. P. Dailey, R. O. Carter III, P. J. Schmitz, W. Zhu, J. C. Bell, and D. Park, *Tribol. Int.* 28:163 (1995).
26. J. C. Bell, K. M. Delargy, and A. M. Seeney, in Proc. 18th Leeds-Lyon Symp. on Tribology, Elsevier, Lyon, France, 1991, p. 387.
27. J. C. Bell and K. M. Delargy, in Eurotrib 93', Vol. Proc. 6th Int. Congr. Tribol., Budapest, 1993, p. 328.
28. J. M. Martin, M. Belin, J. L. Mansot, H. Dexpert, and P. Lagarde, *ASLE Trans.* 29:523 (1986).
29. M. Belin, J. M. Marin, and J. L. Mansot, *ASLE Trans.* 32:410 (1989).
30. B. Cavdar and K. C. Ludema, *Wear* 148:305 (1991).
31. S.-H. Choa, K. C. Ludema, G. E. Potter, B. M. DeKoven, T. A. Morgan, and K. K. Kishore, *Wear* 177:33 (1994).
32. E. S. Yamaguchi, P. R. Ryason, S. W. Yeh, and T. P. Hansen, *Trib. Trans.* 41:262 (1998).
33. Z. Yin, M. Kasrai, G. M. Bancroft, K. F. Laycock, and K. H. Tan, *Tribol. Int* 26:383 (1993).
34. M. Fuller, M. Kasrai, J. S. Sheasby, G. M. Bancroft, K. Fyfe, and K. H. Tan, *Tribol. Lett.* 1:367 (1995).
35. E. S. Ferrari, K. J. Roberts, M. Sansone, and D. Adams, *Wear* 236:259 (1999).

36. M. L. S. Fuller, M. Kasrai, G. M. Bancroft, K. Fyfe, and K. H. Tan, *Tribol. Int.* **31**:627 (1998).
37. Z. Yin, M. Kasrai, M. Fuller, G. M. Bancroft, K. Fyfe, and K. H. Tan, *Wear* **202**:172 (1997).
38. K. Varlot, M. Kasrai, J. M. Martin, B. Vacher, G. M. Bancroft, E. S. Yamaguchi, and P. R. Ryason, *Trib. Lett.* **8**:9 (2000).
39. M. Kasrai, J. N. Citler, K. Gore, G. Canning, and G. M. Bancroft, *Tribol. Trans.* **41**:69 (1998).
40. M. Kasrai, M. Vasiga, M. Suominen Fuller, G. M. Bancroft, and K. Fyfe, *J. Synchrotron Rad.* **6**:719 (1999).
41. G. W. Canning, M. L. Suominen Fuller, G. M. Bancroft, M. Kasrai, J. N. Cutler, G. De Stasio, and B. Gilbert, *Trib. Lett.* **6**:159 (1999).
42. M. Aktary, M. T. McDermott, and J. Torkelson, *Wear* **247**:172 (2001).
43. J. J. Dickert and C. N. Rowe, *J. Org. Chem.* **32**:647 (1967).
44. R. C. Coy and R. B. Jones, *ASLE Trans.* **24**:77 (1981).
45. C. H. Bovington and B. Dacre, *ASLE Trans.* **27**:252 (1984).
46. R. B. Jones and R. C. Coy, *ASLE Trans.* **24**:91 (1981).
47. F. T. Barcroft, R. J. Bird, J. F. Hutton, and D. Park, *Wear* **77**:355 (1982).
48. S. Plaza, *ASLE Trans.* **30**:233 (1987).
49. B. Dacre and C. H. Bovington, *ASLE Trans.* **26**:333 (1981).
50. P. A. Willermet, S. K. Kandah, W. O. Siegl, and R. E. Chase, *ASLE Trans.* **26**:523 (1983).
51. P. A. Willermet and S. K. Kandah, *Lubr. Sci.* **5**:129 (1993).

52. J. M. Palacios, *Tribol. Int.* 19:35 (1986).
53. F. Rounds, *Tribol. Trans.* 36:297 (1993).
54. H. So, Y. C. Lin, G. G. S. Huang, and S. T. Chang, *Wear* 166:297 (1993).
55. G. Binnig and H. Rohrer, *Phys. Rev. Lett.* 49:57 (1982).
56. G. Binnig, C. F. Quate, and C. Gerber, *Phys. Rev. Lett.* 56:930 (1986).
57. R. W. Carpick and M. Salmeron, *Chem. Rev.* 97:1163 (1997).
58. R. Overney and E. Meyer, *MRS Bulletin* May:26 (1993).
59. W. D. Callister Jr., *Materials Science and Engineering: An Introduction*, John Wiley & Sons, Inc., New York, 1994.
60. W. C. Oliver and G. M. Pharr, *J. Mater. Res.* 7:1564 (1992).
61. J. E. Houston and T. A. Michalske, *Nature* 356:266 (1992).
62. S. A. Joyce and J. E. Houston, *Rev. Sci. Instrum.* 62:710 (1991).
63. M. F. Doerner and W. D. Nix, *J. Mater. Res.* 1:601 (1986).
64. O. L. Warren, Graham, and Norton, *Phys. in Can.* March / April:122 (1998).
65. B. J. Brisco, L. Fiori, and E. Pelillo, *J. Phys. D: Appl. Phys.* 31:2395 (1998).
66. I. Karapangiotis, W. Gerberich, and D. F. Evans, *Langmuir* 17:2375 (2001).
67. H. Engqvist and U. Wiklund, *Tribol. Lett.* 8:147 (2000).
68. N. X. Randall and A. Harris, *Wear* 245:196 (2000).
69. J. Fritz, M. K. Baller, H. P. Lang, T. Strunz, E. Meyer, H.-J. Guntherodt, E. Delamarche, C. Gerber, and J. K. Gimzewski, *Langmuir* 16:9694 (2000).

70. A. B. Mann and J. B. Pethica, *Langmuir* 12:4583 (1996).
71. A. Balashakov and G. M. Pharr, *J. Mater. Res.* 14:1049 (1998).
72. I. N. Sneddon, *Int. J. Eng. Sci.* 4:47 (1965).

Chapter II

Morphological Evolution of Films Formed from the Thermooxidative Decomposition of ZDDP*

Introduction

Zinc dialkyldithiophosphate (ZDDP) additives are a vital component of most commercial lubrication formulations. These materials inhibit oxidation of metal parts and form sacrificial films that reduce the wear of contacting surfaces considerably. The mechanism of antiwear film formation has been under intensive scrutiny and a number of mechanisms have been proposed [1, 2]. Although not completely understood, it is well accepted that the antiwear films are not composed of the ZDDP additive itself but are formed from ZDDP decomposition products: mainly zinc polyphosphates [1]. The uncertainty in the mechanism of antiwear film formation derives in part from the observation that exposing metal surfaces to heated ZDDP/oil solutions forms films similar to those generated in a wear rig (tribofilm) [2]. These “thermal films” are thought to form from the products of the thermooxidative decomposition of ZDDP. Although the thermal model seems viable, ZDDP tribofilms can be produced at temperatures well below that of thermooxidative decomposition. From a utility standpoint, both tribofilms and thermal films seem to provide protection from wear [3]. Thus, the current model for the antiwear action of ZDDP involves both a tribochemical and thermal component [4, 5]. A number of studies have focussed on the solution phase thermooxidative decomposition of ZDDP [6-9]. The resulting films

* A form of this Chapter was published as: M. Aktary, M.T. McDermott, and J. Torkelson, *Wear* **247**: 172 (2001)

prepared by exposing substrates to heated ZDDP solutions have also been studied and often in parallel with tribofilms for comparison purposes [4, 10-12].

The current understanding of the structure of ZDDP based films derives mainly from results from X-ray absorption near-edge structure (XANES) spectroscopy [2-4, 13, 14] and to a lesser extent infrared (IR) spectroscopy [15-18]. The most prominent models involve a two-layer structure. The layer in contact with the metal surface is thought to be composed of short chain length polyphosphates that are inter-grown with the iron oxide film on the metal surface. A second layer, consisting of long chain zinc polyphosphates, covers the first.

Thus far the topography of ZDDP derived films has received less attention in the literature. Several studies have employed scanning electron (SEM) or transmission electron microscopy (TEM) [5, 15, 17] to examine the distribution of ZDDP films formed both tribochemically and thermally. Scanning Auger microscopy has demonstrated the ability to correlate surface topography with film composition [19]. Recent studies have exploited the high resolution of scanning probe microscopic (SPM) techniques to probe the nanometer-scale topographic, frictional and mechanical properties of ZDDP antiwear films. Scanning force microscopy (SFM) images of tribofilms on steel revealed a smooth topography containing pits [20]. In addition, SFM based force-distance curves indicated that a soft layer is present on the surface of tribofilms. A separate study employed SFM and a related technique, interfacial force microscopy (IFM), to examine the topography and mechanical properties of tribo- and thermal ZDDP films [21].

This study found a correlation between the steel substrate topography and the deformation behavior of the films.

In this work, I extend the use of SFM in a study focused on probing the topographic evolution of thermal ZDDP films. Here, the term “thermal films” indicates films formed from the thermooxidative breakdown of ZDDP. In the two previous SFM studies of ZDDP films on steel, image interpretation was complicated by a rough substrate topography [20, 21]. Here I employ flat Au as a support for thermal ZDDP films to limit contributions of the substrate to the measured topography. The focus is to examine thermal films as a function of formation time by tracking the evolution of film morphology. The SFM images will be correlated with results from IR reflection absorption spectroscopy (IRRAS) analysis to relate surface structure to chemical composition. In addition, the nanoindentation system will be used to measure film thickness. Overall, these studies build upon the current understanding of antiwear films and provide a more complete picture of the morphology and structure of thermal ZDDP films.

Experimental

Reagents and materials. MCT 10 and EHC 45 base oils and the commercial ZDDP concentrate, ECA 6654 (15% iso-octyl and 85% iso-butyl dithiophosphate) were obtained from Imperial Oil of Canada, Samia Division. Reagent grade methanol and hexane (Caledon) were used as received. Pre-purified reagent grade Ar gas was used as received.

Sample preparation. All substrates were prepared by sputtering Au onto support materials. For infrared analysis, 15 nm of Cr and 300 nm of Au were sputtered onto a clean glass microscope slide. For SFM experiments, 2 nm of Cr and 40 nm of Au were sputtered onto freshly cleaved mica. These latter Au films provide relatively flat and featureless surfaces over lateral distances of tens of microns. For both SFM and IRRAS samples, Au substrates were rinsed in methanol and dried under Ar gas before being placed in an oil bath containing 1.5 wt.% ZDDP pre-heated to 150°C. The substrates were withdrawn from solution after various time intervals, rinsed in hexane (5 min) and dried with Ar gas until no visible solvent was present. The experimental procedure is summarized in Figure 2.1.

SFM imaging. SFM images were collected using a Nanoscope III (Digital Instruments, Santa Barbara, CA) using triangular Si₃N₄ cantilevers (spring constant, $k \sim 0.06$ N/m). Images presented here were captured continuously at a scan rate of 7.8 - 10.2 Hz at a normal force of no more than 50 nN. The images were software flattened both in the X and Y directions but have not been filtered.

IRRAS. All spectra were collected with a Mattson Infinity FTIR spectrometer equipped with a low-noise, I-N₂ cooled, MCT-A detector. A reflection accessory and a home built sample holder were housed in an external, auxiliary bench. The incident radiation was *p*-polarized and reflected at the substrate surface at a glancing angle of $\sim 80^\circ$ with respect to the surface normal. Each spectrum is an average of 500 scans obtained at a resolution of 2 cm⁻¹ and

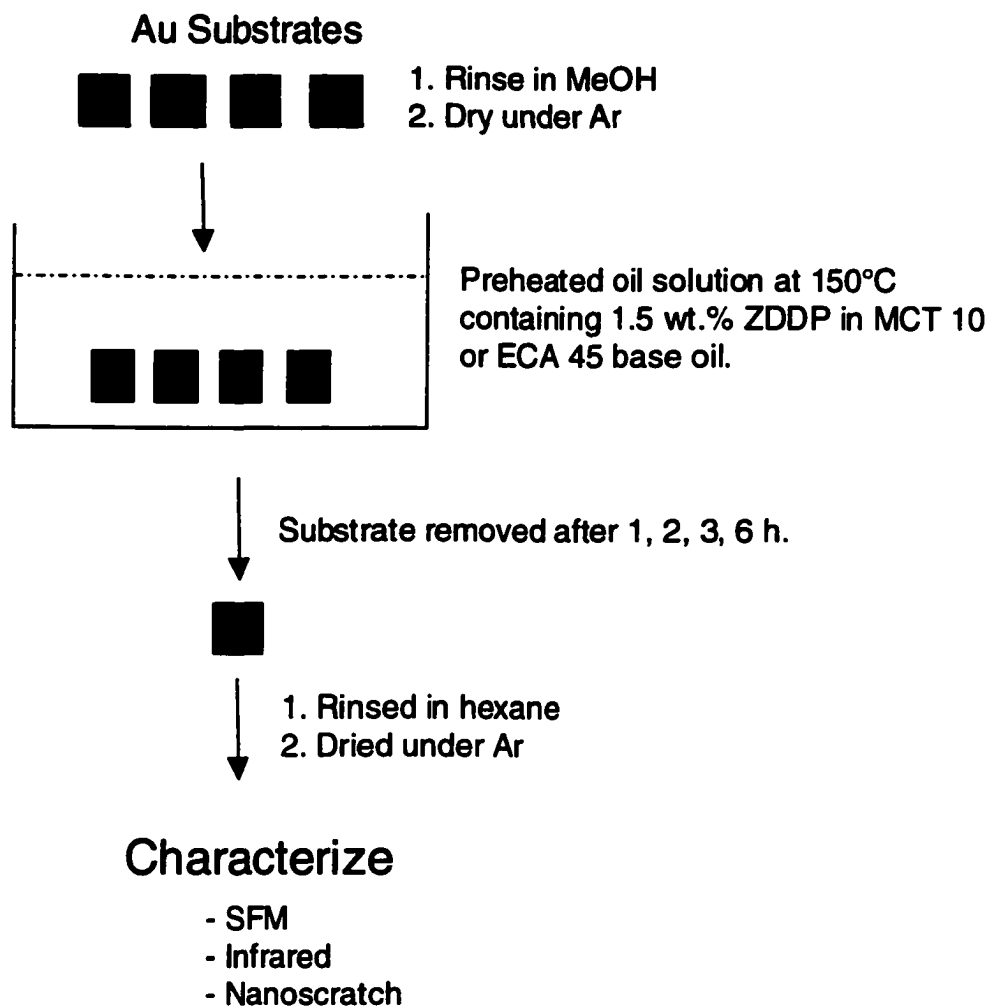


Figure 2.1. Procedure for preparing and characterizing ZDDP thermal films on Au.

a mirror speed of 40 kHz. Reference spectra using a clean Au substrate were obtained in a similar way.

Scratching experiments. Scratching experiments were performed with a Triboscope® (Hysitron Inc, Minneapolis, Minnesota) nanomechanical test instrument interfaced to a Digital Instrument (Santa Barbara, CA) controller allowing in-situ imaging of the indent and scratch regions. Scratching was performed with a cube corner diamond tip (Hysitron Inc) at a force of ~100 μN and a scan rate of 2 Hz for one complete cycle of the selected region. A detailed description of the nanoindenter will be given in Chapter III.

Results and Discussion

I first present results from control experiments aimed at characterizing material deposited onto Au from heated ZDDP-free MCT 10 base oil. Part A of Figure 2.2 is a $5 \times 5 \mu\text{m}$ topographic SFM image of an unmodified Au substrate. Full-scale in the z-direction is 10 nm, which is similar to most of the images presented here. As shown in Figure 2.2A, the surface of 40 nm thick Au films appears flat and featureless. Part B of Figure 2.2 is a topographic image of a similar Au substrate after 6 h immersion in MCT 10 held at 150°C. Evident in the image are relatively large islands, which range in height from 10 to 30 nm. These structures presumably originate from the deposition of material from the MCT 10. The islands were stable to imaging at moderate normal forces (10 nN) for extended periods.

An evaluation of the chemical composition of the material observed in Figure 2.2B was made using IRRAS. MCT 10 is a Group 1 base oil and contains

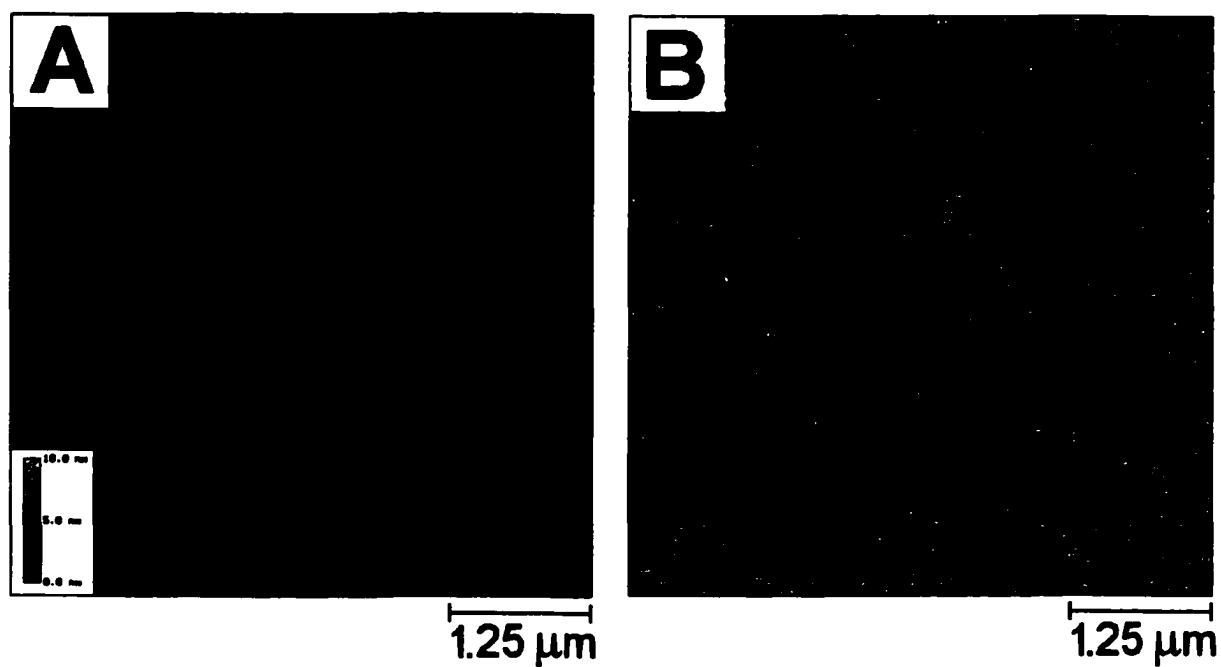


Figure 2.2. Topographic $5 \times 5 \mu\text{m}$ (z -scale = 10 nm) of (A) Unmodified Au substrate, and (B) Au substrate immersed in MCT 10 base oil for 6 h at 150°C . The inset in panel A represents the color scheme for the z -scale on both images.

>0.03% sulfur in the form of compounds such as thiophenes. Figure 2.3A is spectrum of a Au substrate exposed to MCT 10 under the same conditions as in Figure 2.2B. The prominent band in the spectra at 1165 cm^{-1} is consistent with S=O or C=S stretching modes. Material deposited on the Au substrate containing these functional groups is likely the result of thermooxidative decomposition of thiophene molecules in the MCT 10. The high affinity of sulfur containing compounds for Au surfaces results in the tight binding of these decomposition products. Other bands present in Figure 2.3A include those due to CH_2 and CH_3 deformation modes at 1437 cm^{-1} and due to C=O stretching at 1717 cm^{-1} . These functional groups are expected from the thermooxidative decomposition of hydrocarbon species in the base oil. It is clear from Figure 2.2B and spectrum A of Figure 2.3 that products from the MCT 10 oil can potentially contribute to and complicate the composition and morphology of an antiwear film derived from ZDDP.

Group 2 base oils, by definition, contain a lower amount of sulfur (<0.03%). We thus explored the possibility of forming films from EHC 45, a Group 2 base oil. Spectrum B in Figure 2.3 characterizes the Au substrate after being immersed in EHC 45 heated to 150°C for 6 h. Clearly, less material is deposited on the Au substrate and no band is observed at 1165 cm^{-1} reflecting the lack of sulfur containing species in EHC 45. Figure 2.3C is a $5 \times 5\ \mu\text{m}$ topographic SFM image of a substrate following immersion in heated EHC 45. The image reveals a much lower density of islands relative to Figure 2.2B and correlates well with the IRRAS spectra. These results directed me toward the

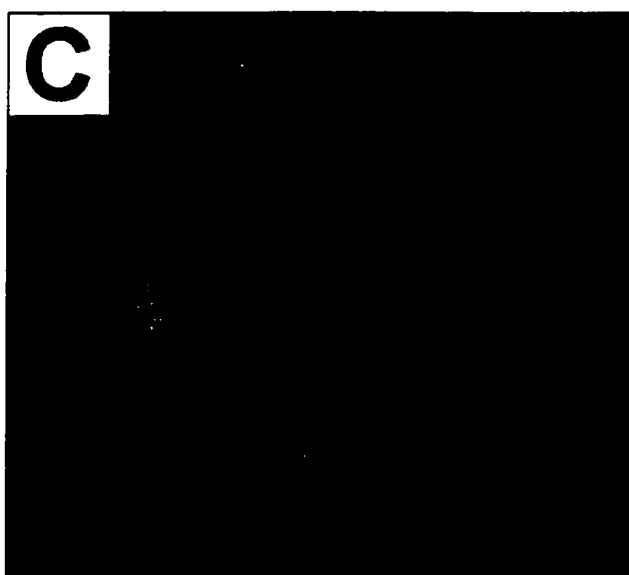
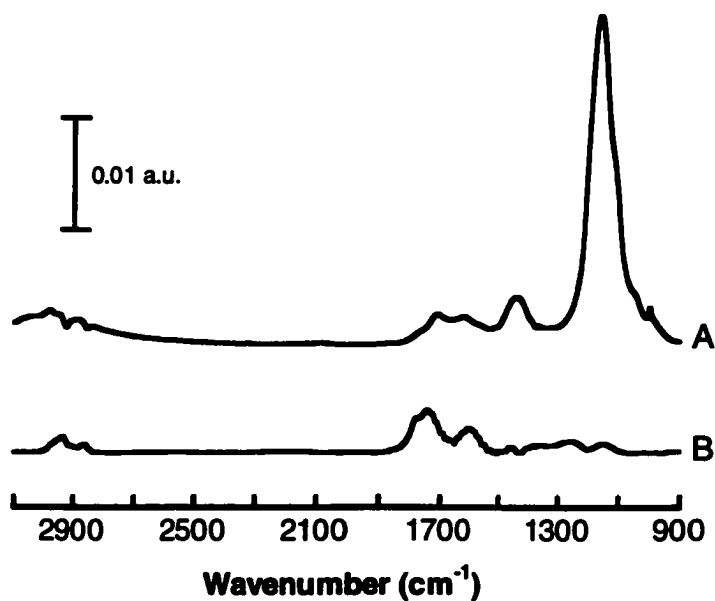


Figure 2.3. IRRAS spectra of Au substrates immersed in base oil for 6 h at 150°C. Spectrum (A) is MCT 10 and (B) is EHC 45. (C) Topographic 5 × 5 μm (z-scale = 20 nm) of Au substrate immersed in EHC 45 base oil for 6 h at 150°C.

use of EHC 45 to limit contributions from the base oil. The remainder of the study presented below corresponds to thermal ZDDP films formed from EHC 45.

An overview of the effect of immersion time on the morphology of thermal films is shown in Figure 2.4. My protocol for thermal film formation entails preheating a solution of EHC 45 containing 1.5 wt.% ZDDP to 150°C and immediately immersing all Au substrates simultaneously (time = 0). Importantly, I observe the precipitation of oil insoluble ZDDP decomposition products after ~2 h at 150°C. I believe that the observation of a precipitate is linked with changes in film morphology as discussed below.

Figure 2.4 contains low-resolution ($50 \times 50 \mu\text{m}$) topographic images of Au substrates immersed in ZDDP solution for 1, 2, 3 and 6 h. Figure 2.4A represents the topography resulting from 1 h immersion. At this point, the film is relatively uniform, with no distinguishing features. Note that the z-scale is 50 nm for the $50 \times 50 \mu\text{m}$ image. In fact, higher resolution images (Figure 2.9A) are necessary to differentiate the 1 h film from the unmodified Au substrate. At this stage of heating, I observe negligible amounts of precipitate in the ZDDP/base oil solution. Figure 2.4B depicts film topography after 2 h immersion. Large islands are now present which measure up to 500 nm in height. Note that the z-scale of Figure 2.4B is 800 nm compared to 50 nm for Figure 2.4A. Also, after 2 h I observe a significant amount of precipitate in the oil solution. Further evolution in thermal film morphology is observed in Figure 2.4C. After 3 h immersion in 150°C ZDDP/EHC 45, the density of islands increases slightly while their average height remains similar to that in Figure

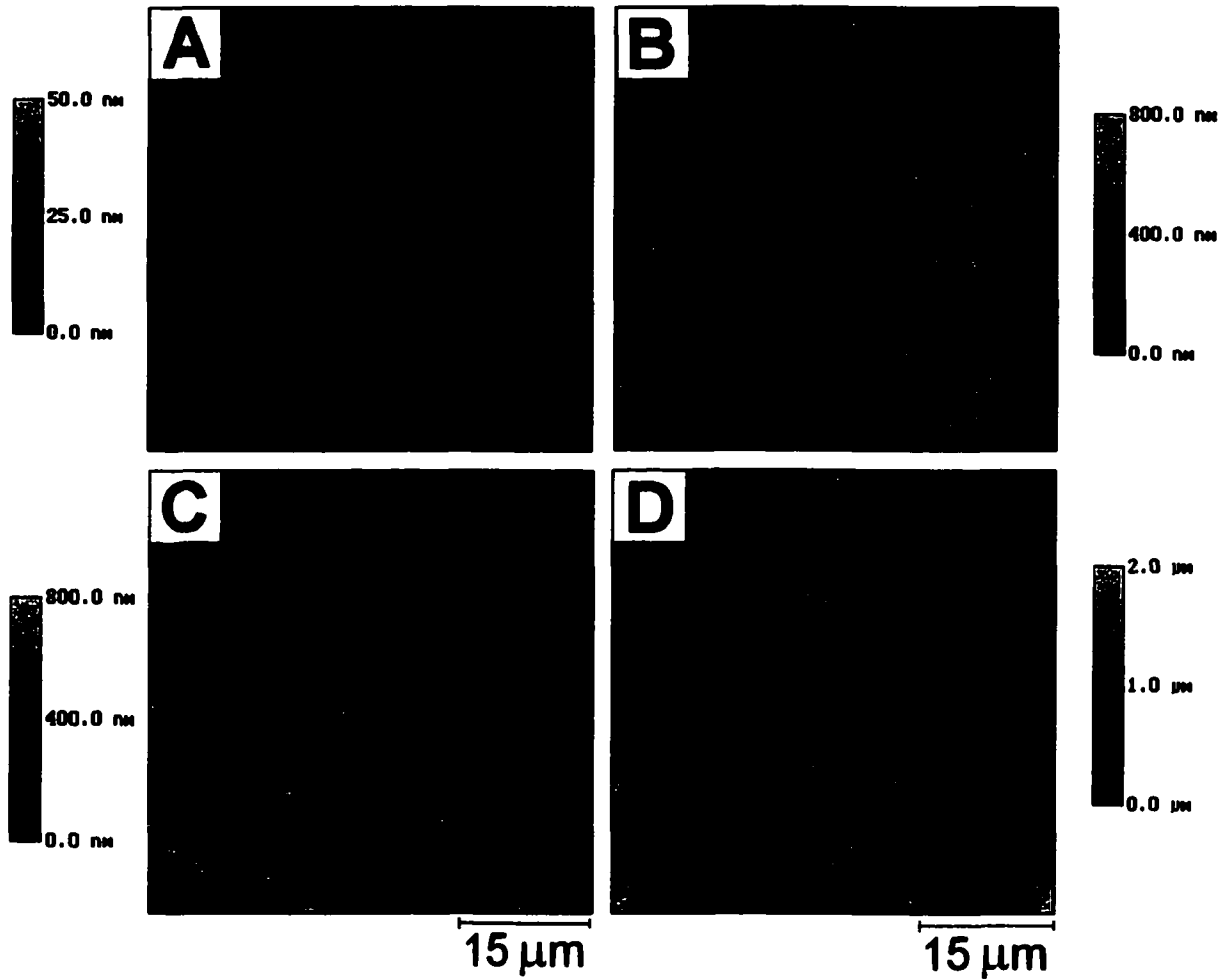
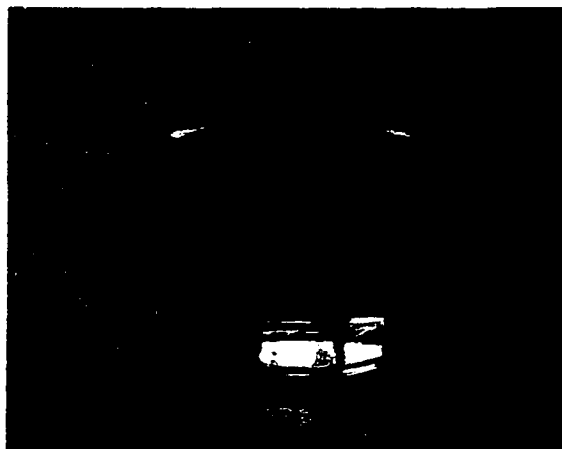


Figure 2.4. Topographic $50 \times 50 \mu\text{m}$ images of substrate immersed in a 1.5 wt.% ZDDP solution for various lengths of time held at 150°C . Image (A) is for 1 h (z-scale = 50 nm), (B) is for 2 h (z-scale = 800 nm), (C) is for 3 h (z-scale = 800 nm), (D) is for 6 h (z-scale = 2 μm).

2.4B. Figure 2.4D depicts the topography of thermal ZDDP films on Au after 6 h. The height of the islands increases to $>1 \mu\text{m}$. Several islands in Figure 2.4D appear to have coalesced to form crystals with lateral dimensions of 5 to $10 \mu\text{m}$. Following 6 h the oil solution is extremely turbid due to precipitation. The appearance of the islands in Figure 2.4 corresponds to the observance of oil insoluble decomposition products. Photographs of heated ZDDP oil solutions before and after the formation of the precipitate is shown in Figure 2.5. Before ~ 2 h of heating the solution is translucent and similar in color to the original blend. With further heating (after 2 h) the solution becomes opaque and turbid as a precipitate begins to settle along the walls of the beaker. Thus, the islands in Figure 2.4B – D originate from the precipitate observed in the oil solutions. The aggregated decomposition products bind tightly to the substrate and dominate the film topography at mesoscopic length-scales.

Careful consideration of the images in Figure 2.4 reveals that the structure of thermal films consists of two components: a) the large islands noted above; and b) a relatively smooth and uniform layer that forms first (Figure 2.4A). In an attempt to ascertain the chemical composition of each of these components, I also examined ZDDP films formed thermally on Au with IRRAS. Figure 2.6 contains spectra of films formed after 1, 2, 3, and 6 h immersion. Spectrum D of Figure 2.6, which corresponds to the 6 h film, contains several bands diagnostic of phosphorous containing functional groups between 800 and 1300 cm^{-1} . The intense band at 1250 cm^{-1} is assigned to a P=O stretch, diagnostic of the presence of phosphate in the film. The band at 950 cm^{-1} results

Less than 2 h. heating



Greater than 2 h. heating



Figure 2.5. ZDDP oil solutions heated for less than 2 h (left image) and greater than 2 h (right image).

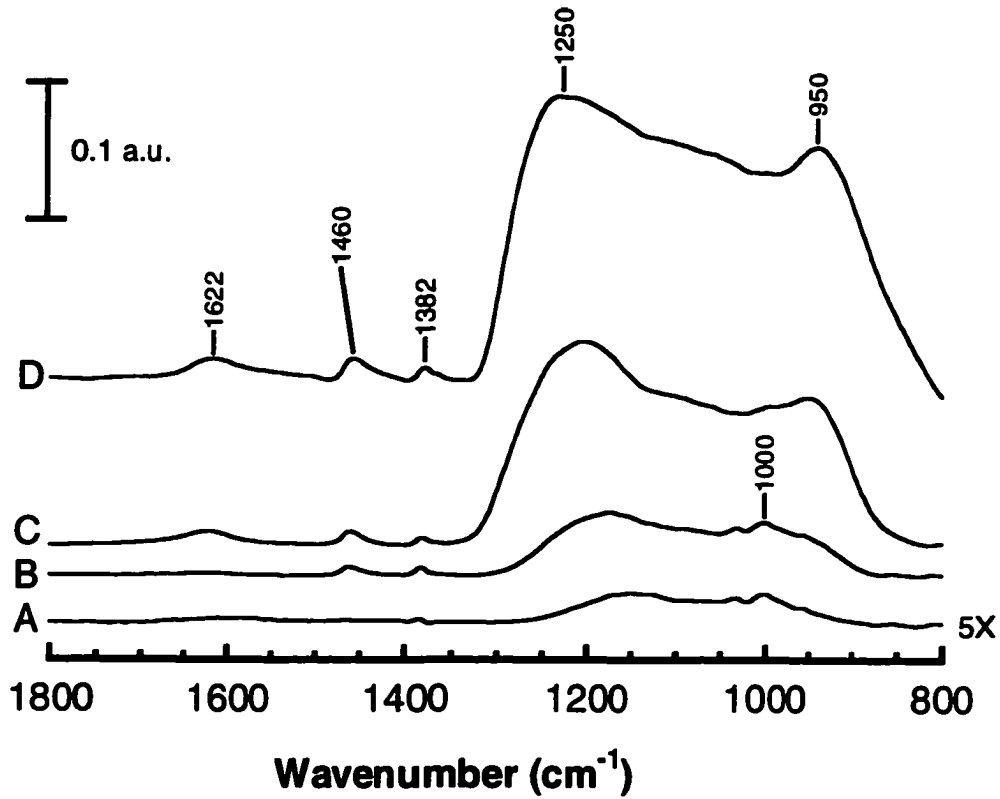


Figure 26. IRRAS spectra of Au substrate immersed in a 1.5 wt.% ZDDP solution held at 150° C. Spectrum A, B, C, and D are for 1, 2, 3, and 6 h immersion times respectively.

from the asymmetric P-O-P stretch of a lengthy phosphate chain backbone. These combined features are consistent with a polyphosphate-like structure[16]. The bands in the 1300-1600 cm^{-1} regions are assigned to CH_2 and CH_3 functionalities. The band at 1622 cm^{-1} likely corresponds to a C=C stretch from organic material deposited from the base oil. Overall, spectrum D of Figure 2.6 is similar to spectra of thermal ZDDP films in previous reports[16].

Insights into the evolution of thermal films can be gained by considering the changes in spectra in Figure 2.6 due to immersion time. The spectra corresponding to short immersion times (Figure 2.4A and 4B) contain a noticeable band at 1000 cm^{-1} corresponding to the P-O-C stretch. This band is the main feature in spectra of the ZDDP starting material [16]. In Figure 2.6, the band at 1000 cm^{-1} becomes obscured at longer times (spectra C and D) by the asymmetric P-O-P stretch at 950 cm^{-1} . The band at 950 cm^{-1} is a major feature in the infrared spectra of phosphate glasses and development of this band in spectra C and D of Figure 2.6 is consistent with the formation of a greater number of chain backbone phosphorous-oxygen bonds [16]. The appearance and growth of this band in the 2, 3 and 6 h films (spectra B through D) correlates with the appearance and growth of the island structures in Figure 2.4. I thus believe that the islands observed in Figure 2.4 are composed of aggregated polyphosphate glass material. Further analysis of the spectra reveals a shift in the P=O stretch to higher frequencies as a function of immersion time. The positions of this band are 1150, 1175 and 1204 cm^{-1} for the 1, 2 and 3 h immersions, respectively. Importantly, the position of the P=O stretch in the 6 h

film (1250 cm^{-1}) is similar to that observed in phosphate glasses. Thus, the evolution of the spectra in terms of the P=O stretch is also consistent with the formation of a polyphosphate glass material.

In summary, the spectral features for thermal ZDDP films formed at short immersion times (1 h, Figure 2.6A) resemble those in reported spectra of the starting material. I believe this stage of the film is comprised of short chain length polyphosphate material and exhibits the morphology shown in Figure 2.4A. At longer heating times (2 – 6 h) I observe large islands in the film structure (Figure 2.4) and the IR spectra indicate the presence of material comprised of longer polyphosphate chains. Also during this time scale I observe the precipitation of oil insoluble decomposition products. Bancroft et al. have shown by XANES analysis that the bulk structure of the precipitate formed from heating ZDDP oil solutions is comprised of a long chain polyphosphate structure [4]. Thus, the islands observed in Figure 2.4 are likely polyphosphate aggregates that form via the thermooxidative decomposition of ZDDP.

The effect of immersion time on thermal film thickness was examined by a scratch test. Regions of the film were displaced from the Au substrate with a TriboScope® nanoindentation system. Figure 2.7 contains an image of a scratched region in a 1 h film formed by raster scanning the nanoindenter tip over a $5 \times 5\ \mu\text{m}$ region at a force of $\sim 100\ \mu\text{N}$. After 1 cycle (up and down), the force was decreased and the image size increased to produce the image in Figure 2.7. The film material is displaced to the edges of the scan region as evidenced by the buildup in topography. The total displacement of the film from

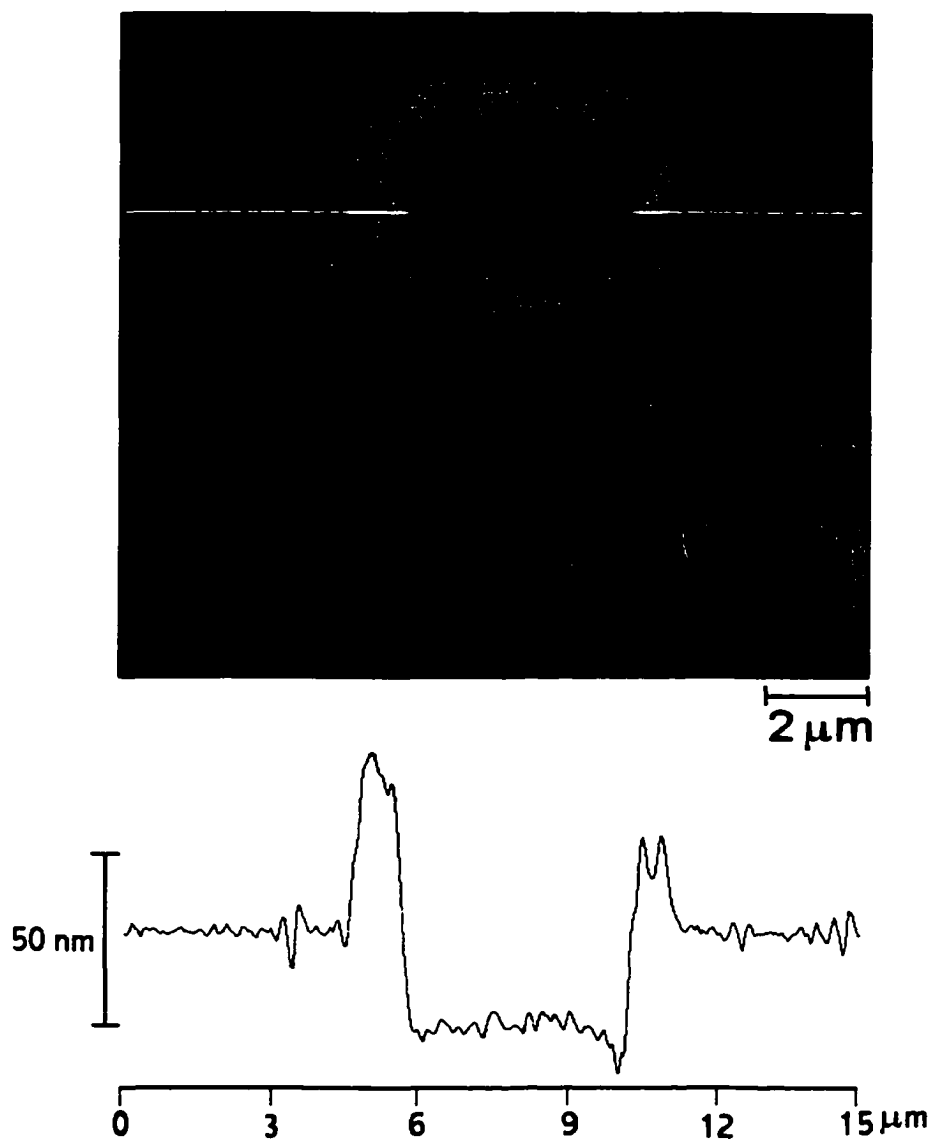


Figure 2.7. Topographic $15 \times 15\ \mu\text{m}$ image obtained with a TriboScope® nanoindentation system. The bottom portion of the image is a topographic line trace across the image as indicated by the white trace on the image.

the Au substrate was verified by imaging the bottom of the scratched area. I note that removal of the Au substrate material during scratching will introduce significant error in our thickness measurements. However, in all cases the topography of the bottom of the scratched region was characteristic of the sputtered Au film and no evidence of damage to the substrate was observed. Cross sectional profiles similar to that shown in Figure 2.7 were collected and analyzed to estimate film thickness.

Results for each immersion time are shown in Figure 2.8. These results correspond to the thickness of the initial, smooth layer and do not include the height of the islands, which measure up to 2 μm for the 6 h film as indicated in Figure 2.4. Consistent with the IRRAS analysis presented here (Figure 2.5) and with XANES results reported previously [4], the thickness of thermal films increases with oil solution heating time. However, the values measured here are significantly higher than those estimated from XANES peak heights. I observe a film thickness over 400 nm for a 6 h immersion. In contrast a thickness of 200 nm was reported for a thermal film formed for 24 h [4]. These results are also inconsistent with those from a recent study of the nanomechanical properties of ZDDP films [21]. From the analysis of indentation studies, Warren et al. predict that thermal films formed for 1 h at 200 °C are greater than 160 nm thick. I feel our scratch method is a more direct measure of thermal film thickness although differences in film preparation from lab-to-lab make direct comparisons difficult.

Figure 2.4 provides a mesoscopic perspective of the structure of thermal ZDDP films. I also examined these films at microscopic length scales. Part A

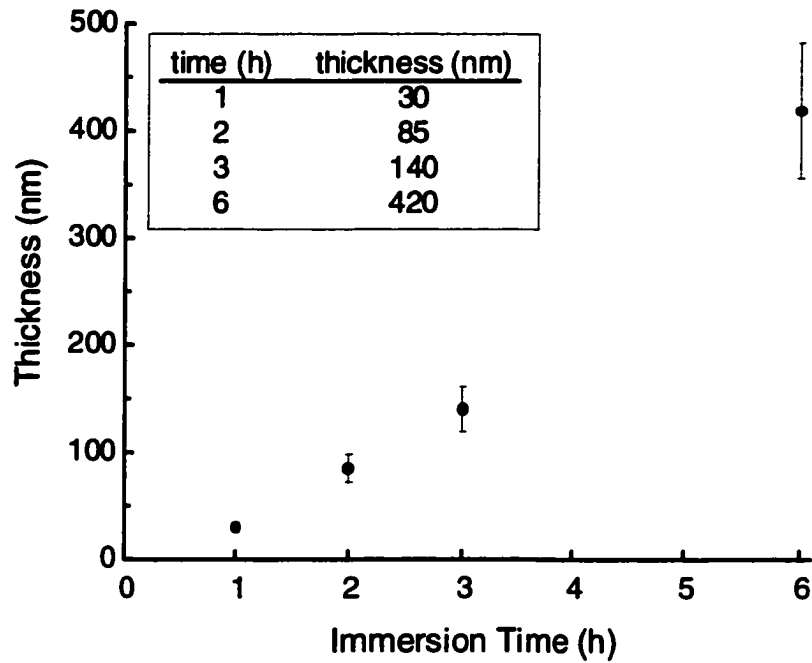


Figure 2.8. Plot of thickness against immersion time for ZDDP thermal films formed on Au substrates. The inset is the raw data used to construct the plot.

of Figure 2.9 is a $1 \times 1 \mu\text{m}$ image of a 1 h thermal film that shows a textured topography distinct from the underlying Au. Image analysis reveals an average grain diameter of 32 nm. This type of structure is observed at several spots on different samples prepared in a similar manner. I believe the image in Figure 2.9A represents the beginning stages of thermal film formation and is composed of a polyphosphate structure. As shown in Figure 2.4 the observed island structures begin to form following 2 h immersion of the Au substrate. The morphology of a 2 h thermal film between the islands is depicted in Figure 2.9B. Comparing parts A and B of Figure 2.9 reveals a development in the film structure as reflected in an increase in the diameter of the observed grains from 32 to 117 nm. Similar to the morphology observed after 1 h, the topography in Figure 2.9B seems to be consistent from spot-to-spot between the large islands.

An interesting development in the sub-micron topography is observed for thermal films formed for 3 and 6 h. Figure 2.9C is a $1 \times 1 \mu\text{m}$ image of a 3 h thermal film showing the morphology to consist of relatively smooth terraces and an array of 15 nm deep pits that range in diameter from 10 to 100 nm. Based on a comparison of Figure 2.9C with Figure 2.9B, I believe that thermal films anneal between 2 and 3 h resulting in the coalescence of grains and the creation of smooth domains. After 6 h evidence for further annealing is apparent. Figure 2.9D illustrates an area that appears relatively flat and featureless. Evidently, after 6 h the pits observed in the 3 h film (Figure 2.9C) have healed resulting in a flat and featureless topography. Considering Figures 2.4 and 2.9 together our results show that the topography of thermal ZDDP films evolve at

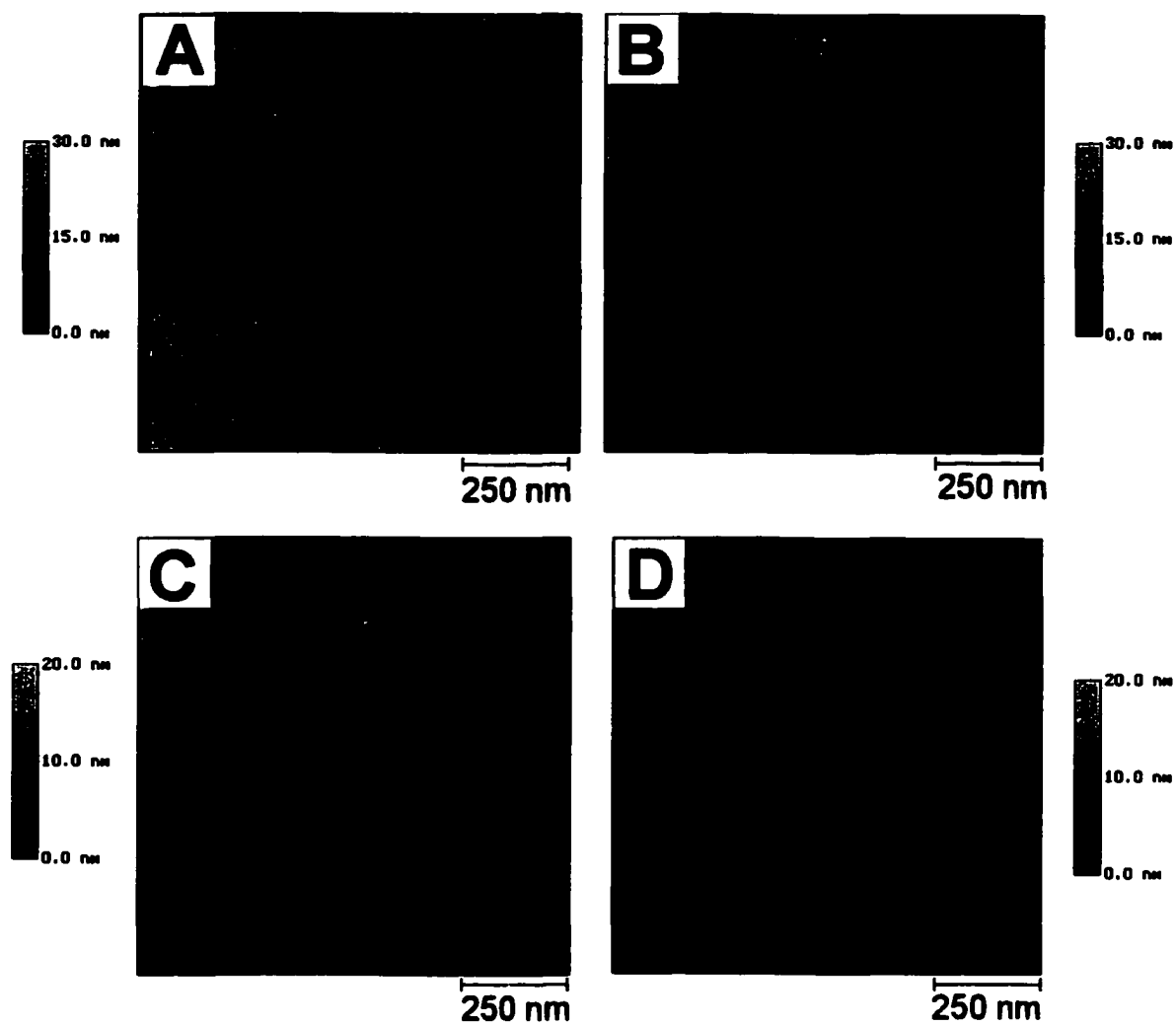


Figure 2.9. Higher resolution $1 \times 1 \mu\text{m}$ images of Au substrates similar to Figure 2.4. Image (A) 1 h (z-scale = 30 nm), (B) 2 h (z-scale = 30 nm), (C) 3 h (z-scale = 20 nm), (D) 6 h (z-scale = 20 nm).

both mesoscopic and sub-micron length scales as a function of heating time. In Figure 2.10, a model representing the film structure after 6 h is depicted. A relatively flat and featureless polyphosphate film is shown to cover the Au substrate. I believe that the growth and evolution of this layer is responsible for the morphological changes in the images of Figure 2.9A – D. Large aggregates of polyphosphates represented by spheres are shown to sit over this first layer. I believe the aggregates originate from the precipitate after ~ 2 h of heating and are responsible for the morphology of the films at the mesoscopic scale as shown in Figure 2.4A – D.

Conclusions

I have used SFM and IRRAS to probe the topography and structure of films formed by the thermal decomposition of ZDDP on Au substrates. The topography of thermal films on both a mesoscopic and sub-micron scale evolves with oil heating time. The mesoscopic morphology is highlighted by the formation and growth of islands. These islands likely result from the precipitation of ZDDP decomposition products and are composed of long chain polyphosphate material. An underlying layer, composed of shorter chain phosphates, surrounds and perhaps embeds these islands. The topography of this underlying layer transforms from a grain structure for 1 and 2 h films to smooth and featureless for 3 to 6 h thermal films. Correlation between thermal film topography observed here and that for tribochemically generated films are currently being developed and will be presented in Chapters III and IV.

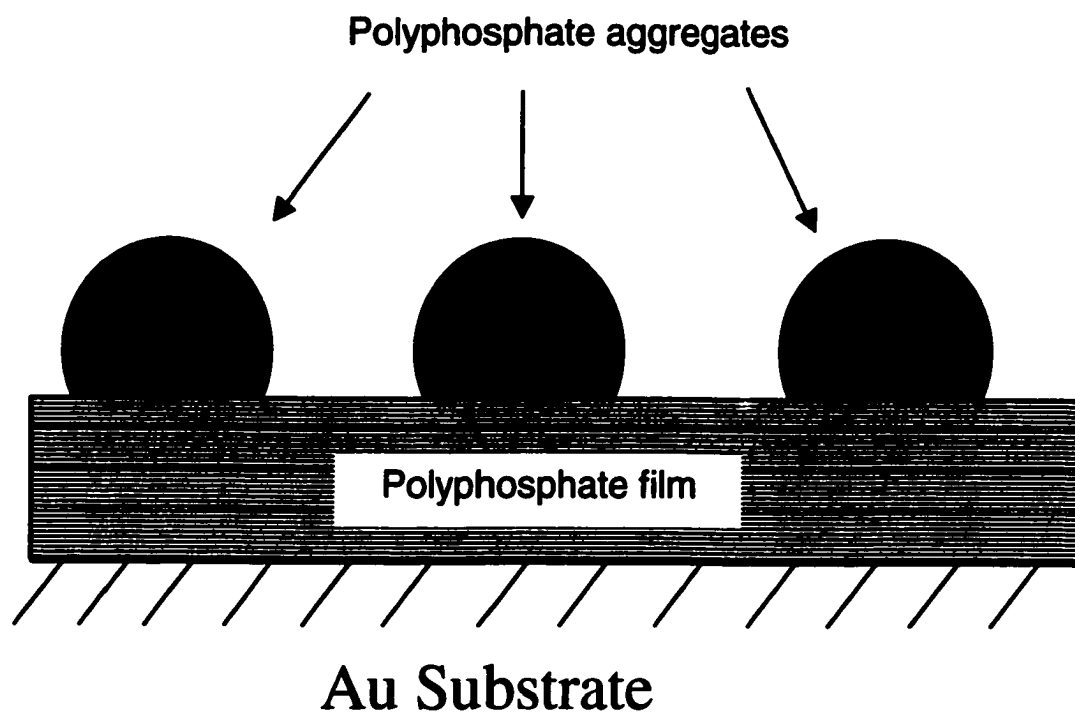


Figure 2.10. A model representing the morphology of the film after 6 h of immersion in a heated oil bath of ZDDP.

References:

1. A. G. Papay, *Lubrication Sci* 10:209 (1998).
2. Z. Yin, M. Kasrai, M. Fuller, G. M. Bancroft, K. Fyfe, and K. H. Tan, *Wear* 202:172 (1997).
3. G. M. Bancroft, M. Kasrai, M. Fuller, Z. Yin, K. Fyfe, and K. H. Tan, *Tribol. Lett.* 3:47 (1997).
4. M. L. S. Fuller, M. Kasrai, G. M. Bancroft, K. Fyfe, and K. H. Tan, *Tribol. Int.* 31:627 (1998).
5. J. M. Martin, *Tribol. Lett.* 6:1 (1999).
6. F. G. Rounds, *ASLE Trans.* 18:79 (1975).
7. R. C. Coy and R. B. Jones, *ASLE Trans.* 24:77 (1981).
8. R. B. Jones and R. C. Coy, *ASLE Trans.* 24:91 (1981).
9. H. Spedding and R. C. Watkins, *Tribol. Int.* 15:9 (1982).
10. B. H. Dacre and C. Bovington, *ASLE Trans.* 24:546 (1981).
11. S. Plaza, *ASLE Trans.* 30:233 (1987).
12. M. Fuller, Z. Yin, M. Kasrai, G. M. Bancroft, E. S. Yamaguchi, P. R. Ryason, P. A. Willermet, and K. H. Tan, *Tribol. Int.* 30:305 (1997).
13. Z. Yin, M. Kasrai, G. M. Bancroft, K. F. Laycock, and K. H. Tan, *Tribol. Int* 26:383 (1993).
14. M. Fuller, M. Kasrai, J. S. Sheasby, G. M. Bancroft, K. Fyfe, and K. H. Tan, *Tribol. Lett.* 1:367 (1995).
15. G. H. Harrison and P. Brown, *Wear* 148:123 (1991).
16. P. A. Willermet, R. O. Carter, and E. N. Boulos, *Tribol. Int.* 25:371 (1992).

17. P. A. Willermet, D. P. Dailey, R. O. Carter III, P. J. Schmitz, W. Zhu, J. C. Bell, and D. Park, *Tribol. Intern* 28:163 (1995).
18. N. E. Lindsay, R. O. Carter III, J. Schmitz, L. P. Haack, R. E. Chase, J. E. de Vries, and P. A. Willermet, *Spectrochimica. Acta.* 49A:2057 (1993).
19. I. R. Barkshire, M. Prutton, and G. C. Smith, *Appl. Surf. Sci.* 84:331 (1995).
20. A. J. Pidduck and G. C. Smith, *Wear* 212:254 (1997).
21. O. L. Warren, J. F. Graham, P. R. Norton, J.E. Houston, and T. A. Michalske, *Tribol. Lett.* 4:189 (1996).

Chapter III

Morphology and Nanomechanical Properties of ZDDP Tribofilms*

Introduction

This chapter will detail our efforts in studying the morphology and nanomechanical properties of ZDDP derived tribofilms prepared in a Cameron – Plint (C – P) wear tester on steel coupon substrates. These studies will build upon the results of Chapter II towards our objective to understand and model the antiwear action of ZDDP in the engine. The C – P wear tester is designed to simulate the temperature, pressure, and sliding velocity of engine components during operation. Tribofilms prepared in the wear tester are thought to resemble those that deposit at the interface of stressed junctions in the engine. Thus the C – P is a convenient bench top test that will provide insight about the nature of the tribofilms on contacting engine components.

A cross sectional schematic view of the C – P wear tester is presented in Figure 3.1A. A cylindrical steel pin is clamped to the end of a reciprocating rod, which is connected on the opposing end to an electric motor. The cylindrical pin is placed firmly over a steel coupon substrate by the application of a loading force. The whole assembly is placed in a temperature controlled oil bath that houses the lubrication blend. The experiment is initiated by engaging the reciprocating motor until the desired sliding speed of the pin is attained over the

* A form of this Chapter has been published as: M. Aktary, M.T. McDermott, and G.A. MacAlpine, Trib. Lett. In Press.

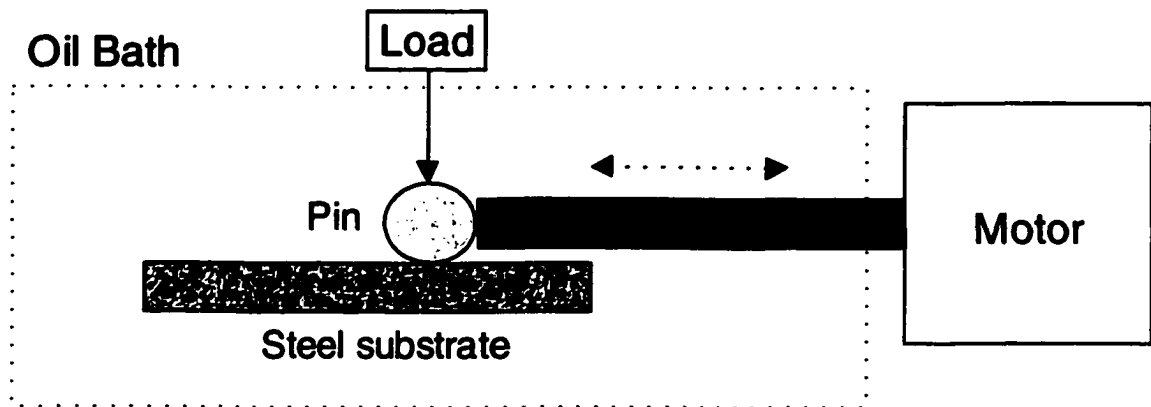


Figure 3.1A. Cross sectional view of the Cameron - Plint (C - P) wear tester used to prepare the tribofilm samples.



Figure 3.1B. Photograph of a 1 × 1 cm steel coupon after the deposition of a tribofilm. The film formed on the upper half of the coupon can be clearly distinguished from the rest of the coupon.

substrate. After a selected time, a macroscopically visible film deposits on regions of the steel coupon that were in contact with the sliding pin. A photograph of a steel coupon run for 1 h. in the C – P wear tester is presented in Figure 3.1B. The light region towards the top half of the coupon is where the tribofilm has deposited and is clearly distinguishable from the rest of the coupon. These tribofilms are thought to originate from tribochemical reactions between the thermooxidative decomposition products of ZDDP and the steel substrate.

A variety of techniques have been employed to gain an understanding of the chemical composition of ZDDP antiwear films formed in different wear testers. Infrared spectroscopy [1-3], X-ray photoelectron spectroscopy (XPS) [4-8], Auger spectroscopy [9, 10], and mass spectrometry [11] have all provided insights into their average chemical composition. In particular, X-ray absorption near-edge spectroscopy (XANES) has been valuable in elucidating the structure and formation mechanism of ZDDP tribofilms. The combined results of these studies have led to the understanding that film formation results from a combination of the thermo-oxidative and friction induced breakdown of ZDDP [12-19]. The overall composition of the films can be described as a glassy polyphosphate material chemisorbed to the iron oxide film of the steel surface. Specifically, it is believed that the bulk of the films are composed of short chain polyphosphates whereas longer chain polyphosphate species predominate on the surface [13, 14].

With the increased level of understanding of the composition of ZDDP derived tribofilms, recent studies have attempted to address questions

concerning local composition, morphology and nanomechanical properties. These latter properties will likely dictate the macroscopic antiwear performance of the films. Scanning force microscopy (SFM) and the related technique, interfacial force microscopy (IFM), are both excellent methodologies for high resolution mapping of the morphology and determination of nanomechanical properties of thin films [20-24]. The topography of tribofilms prepared in a wear tester [21] and by thermooxidative decomposition of ZDDP (thermal films) [20] has been investigated with SFM. Recent studies have highlighted the importance of nanomechanical properties to the antiwear performance of ZDDP films [23, 24]. Graham et al. reported that the aggregates of material characterizing the topography of tribofilms, which they termed "pads", display large spatial variations in nanomechanical properties [24]. The centers of the pads exhibit high elasticity and reduced plastic deformation, similar to the steel substrate, while the pad edge is softer. This study was extended by Canning et al. who used localized XANES to detect a greater percentage of long chain polyphosphates toward the center of the pads relative to the edges. Thus, a relationship between function and the chemical structure of the films was established [25].

In this work, we extend these previous studies by using SFM and nanoindentation analysis to examine the effect of rubbing time on the morphology and nanomechanical properties of ZDDP derived antiwear films. Previous XANES studies have shown that there is a large dependence of the chemical composition of the tribofilms on rubbing time, showing them to be

composed of a high percentage of intact ZDDP at early times, which decomposes to a polyphosphate tribofilm at longer times [14]. In this chapter we will further explore the dynamic nature of the tribofilms by tracking their morphology and nanomechanical properties as a function of rubbing time. Preliminary results on the effect of sliding velocity and the presence of soot impurities on the morphology and nanomechanical properties of the tribofilms will also be presented.

Experimental

Reagents and materials: A solvent refined base oil with a viscosity at 100°C of about 5 mm²/s (referred to as MCT 10), and a commercial ZDDP (15% isooctyl and 85% isobutyl) antiwear additive concentrate, along with coupons of 52100 steel were obtained from Imperial Oil (Samia, ON).

Sample preparation: Sample coupons were polished to a mirror finish with diamond paste and inserted in a Cameron-Plint wear tester. A 1.5 wt.% ZDDP oil solution in MCT 10 was poured into the sample compartment of the Cameron-Plint wear tester. The bath temperature was set to 100 °C. A stainless steel pin was then tightened into position and a force of 225 N was applied between the pin and the coupon. The coupon was rubbed at 25 Hz. The coupon was withdrawn after various lengths of time and rinsed with a low-molecular weight hydrocarbon industrial solvent and dried.

SFM imaging: Topographic SFM images were collected using a Nanoscope III (Digital Instruments, Santa Barbara, CA) scanning force

microscope (SFM) using triangular Si_3N_4 cantilevers (spring constant, $k \sim 0.06$ N/m). Images presented here were captured continuously at a scan rate of 7.8-10.2 Hz at a normal force of <10 nN. The images were software flattened and are otherwise shown unfiltered.

Nanoindentation experiments: Nanoindentation experiments were performed with a Triboscope® (Hysitron Inc., Minneapolis, MN) nanomechanical testing instrument interfaced to a Digital Instrument (Santa Barbara, CA) Dimensions 3100™ scanning probe microscope controller. A schematic of the SFM – nanoindenter system is presented in Figure 3.2. The nanoindenter transducer consists of two outer drive plates and a center “pick up” electrode where the tip is attached. The load is generated electrostatically by applying a voltage between one of the drive plates and the center electrode. The displacement is determined by measuring the voltage between the center electrode and the opposite drive plate. The whole transducer is attached to the piezo tube of the SFM allowing x – y translation. This allows in-situ imaging of the sample before and after an indent. Indents were performed with a cube corner diamond tip (half angle = 90°) (Hysitron Inc) at a force of ~ 100 μN and a loading rate of 10 $\mu\text{N} / \text{sec}$.

Many different regions of each tribofilm sample were analyzed. The nanomechanical properties of the tribofilms were evaluated from their nanoindentation profiles. The elastic modulus (E) and hardness (H) were calculated with the Hysitron analysis software, using an algorithm (refer to Chapter I) based on the method of Oliver and Pharr [26]. To calculate E, the

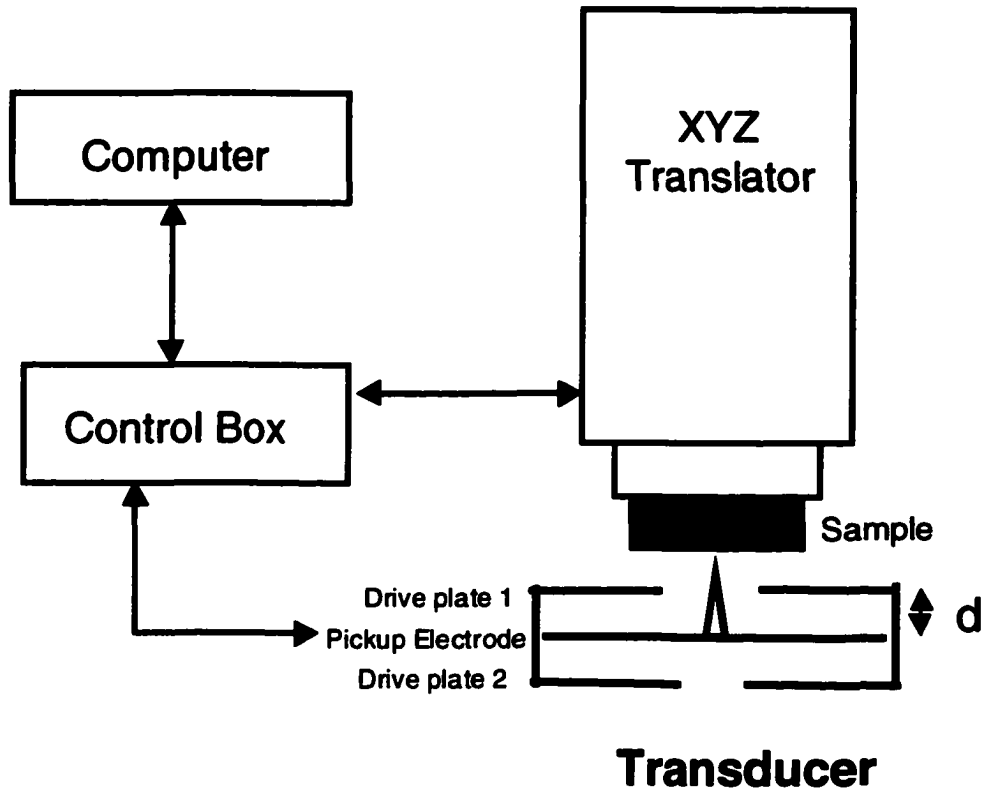


Figure 3.2. Schematic of the nanoindentation system used to determine the nanomechanical properties of the tribofilms.

Poisson ratio (ν) of the material must be known. Since ν is unknown for ZDDP derived tribofilms, we report the indentation modulus ($E^* = E/(1-\nu^2)$) for the films.

SEM and EDX analyses: Secondary electron images and energy dispersive X-ray spectra were collected with a JEOL model 6301FXV scanning electron microscope at accelerating voltages between 5 - 20 kV and a working distance of 4-5 mm.

Results and Discussion

1. Film structure as a function of rubbing time

Scanning electron microscopy (SEM) and energy dispersive X-ray (EDX) analysis provides initial assessment of the effect of rubbing time on film coverage. Figure 3.3A is a SEM image of a tribofilm that has been prepared from 5 min of rubbing. Observed is a pattern of light and dark contrast where the darker regions correspond to the tribofilm and the lighter regions are the underlying steel substrate. This contrast is attributed to the lower conductivity and atomic number of the film relative to the steel substrate. To confirm the assignment of each region, EDX spectra were collected at the spots marked 1 and 2 of Figure 3.3A and are shown in Figure 3.4. Spectra 1 and 2 correspond to the regions in Figure 3.3A labeled 1 and 2, respectively. Spectrum 3 results from subtraction of spectrum 1 from 2 and is shown to highlight the compositional differences between the regions. The dominant features in spectrum 1 are the Cr and Fe K_{α} lines at 5.2, 6.2, and 6.8 keV arising from the steel substrate. In addition to the signals due to Fe and Cr, spectrum 2 contains peaks at 1.9, 2.2,

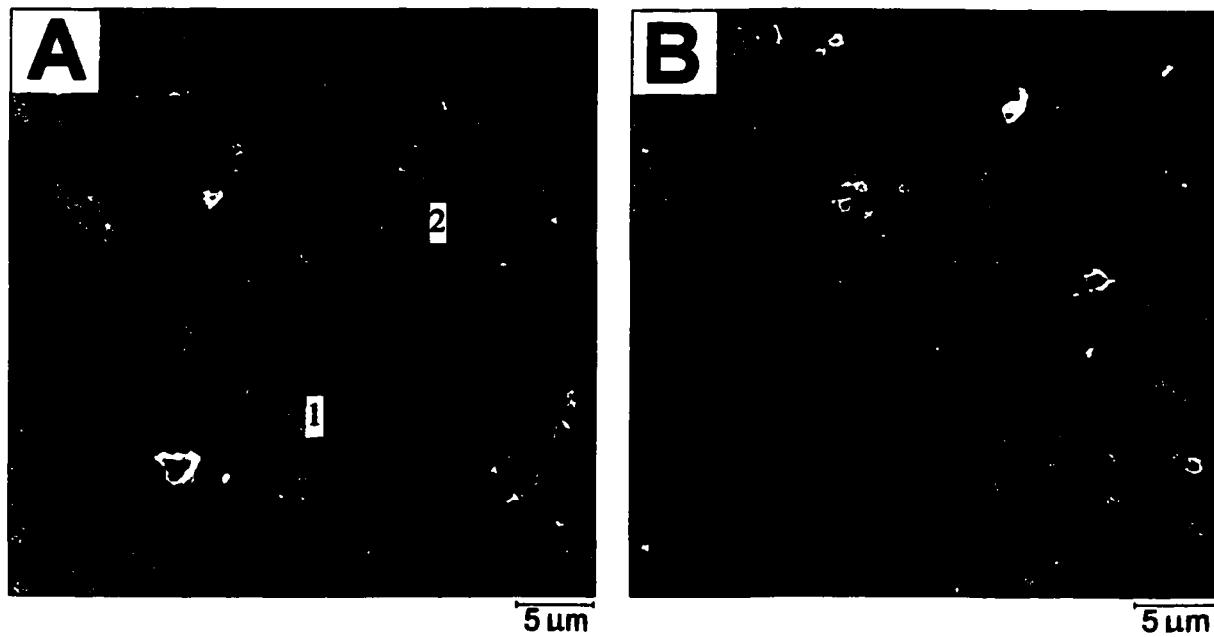


Figure 3.3. SEM images of tribofilms prepared from 5 min (panel A) and 40 min (panel B) of rubbing contact in a C - P wear tester.

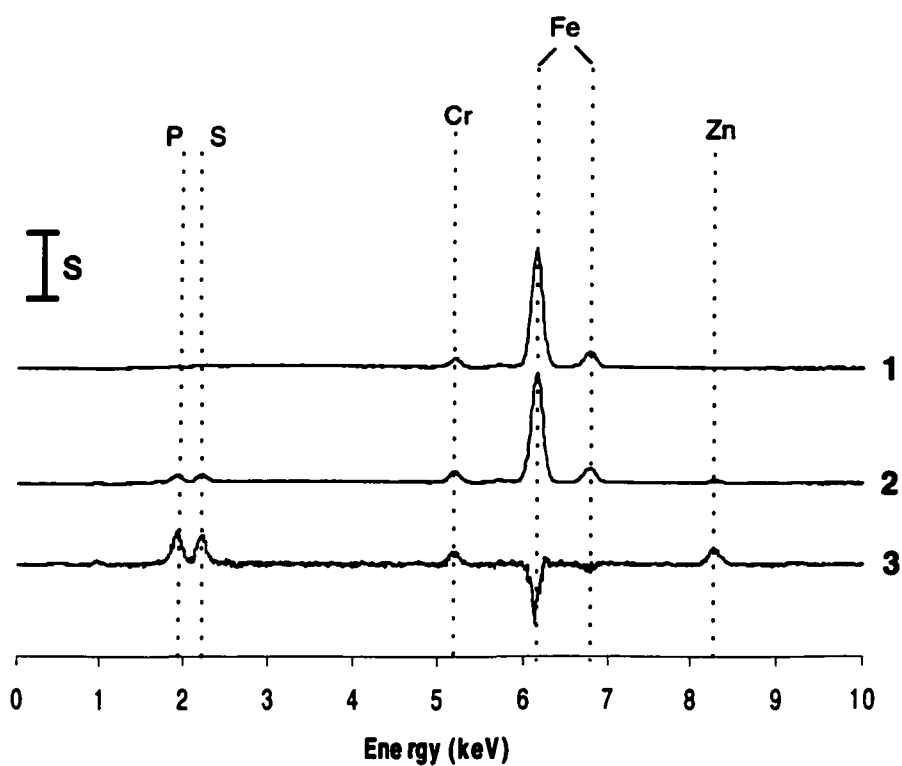


Figure 3.4. EDX spectra collected from the 5 min. tribofilm sample. Spectrum 1 and 2 correspond to the labels 1 and 2 in Figure 3A. Spectrum 3 results from the subtraction of 1 from 2. $S = 5000$ counts for all spectra.

and 8.3 keV that correspond to P, S, and Zn, respectively. The P, S and Zn signals are seen more clearly in spectrum 3 and must originate from the ZDDP starting material. These spectra confirm that the regions exhibiting dark contrast in the SEM image are derived from the starting ZDDP compound while the brighter contrast regions are mainly steel substrate. The Fe and Cr peaks in spectrum 2 are present because the penetration depth of the EDX analysis is ~10 μm , greater than the estimated thickness of the film (hundreds of nanometers).

Figure 3.3A suggests that a film generated for 5 min is comprised of isolated islands or pads in agreement with SFM observations by Graham *et al.* [24]. However, after short rubbing times a significant amount of the steel substrate is exposed as evidenced by the regions of brighter contrast in Figure 3.3A. As rubbing time is increased, film coverage becomes greater and the amount of exposed steel decreases. This is illustrated in Figure 3.3B, which is a SEM image of a film formed for 40 min. The regions of brighter contrast (steel substrate) occupy a smaller percentage (< 5%) of the total image area. In general, complete 2-dimensional coverage of the steel substrate requires 30-40 min rubbing times.

The effect of rubbing time on the morphology of tribofilms was examined in more detail with SFM. In all SFM images presented here, bright contrast will depict regions of high topography and the sliding direction of the pin over the substrate is from top to bottom on the images. The images in Figure 3.5 are representative of the morphology of tribofilms after 10 min (A), 40 min (B), 60

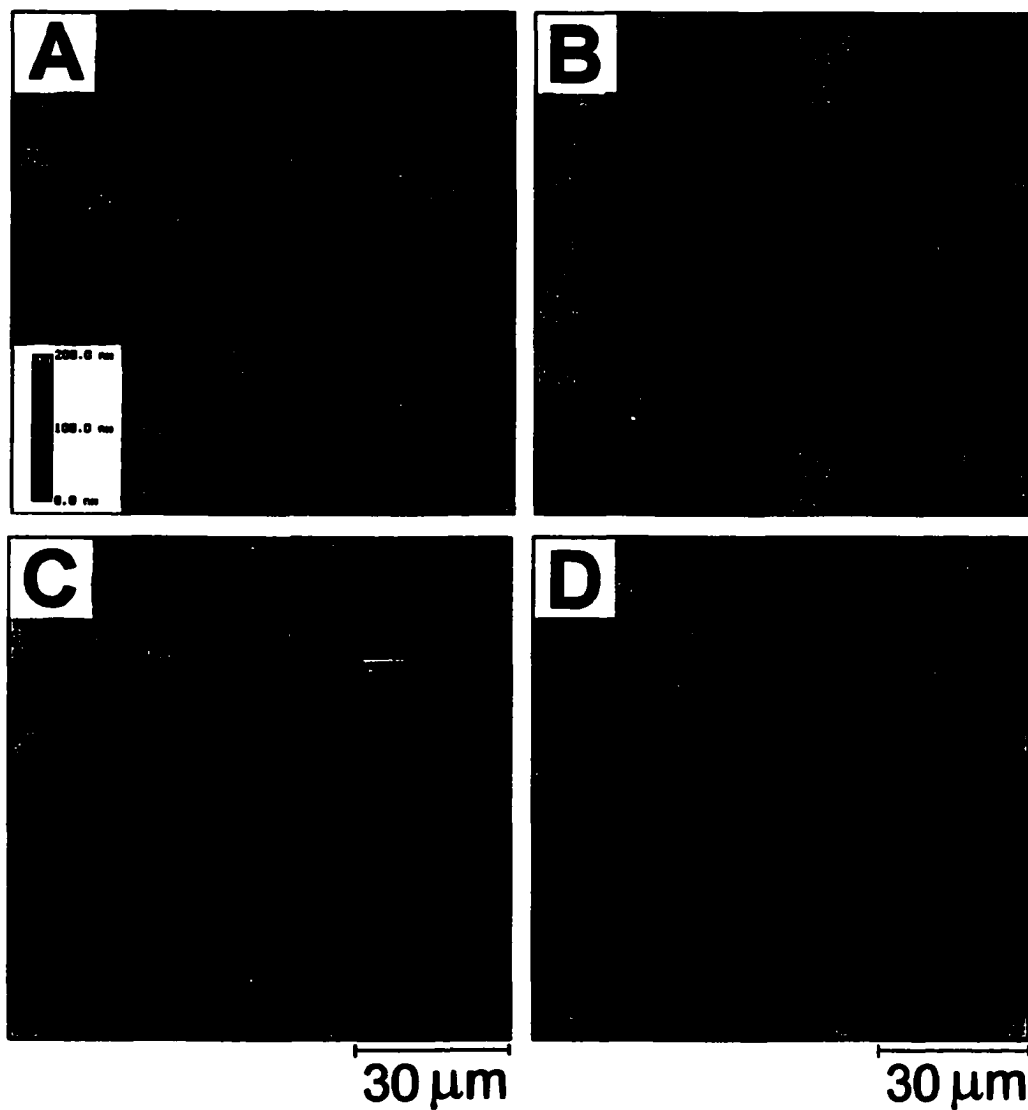


Figure 3.5. Topographic $100 \times 100 \mu\text{m}$ contact mode SFM images (z-scale = 200 nm) of tribofilms formed in a Cameron-Plint wear tester for different times. (A) 10 min, (B) 40 min, (C) 60 min, and (D) 120 min. The inset in panel represents the color scheme for the z-scale on all the images.

min (C), and 120 min (D) of rubbing. The morphology of the 10 min film in Figure 3.5A is dominated by large grains that measure up to 30 μm in diameter and 200 nm in height. This morphology resembles that of the 5 min film observed in the SEM image of Figure 3.3A. The trough running from top to bottom of Figure 3.5A separates the wear tracks, which are the machine marks of the reciprocating pin. The dimension of the grains in Figure 3.5A are similar to that for the load carrying pads that were observed by Graham et al. [24]. The surface coverage is not uniform and regions much lower in topography (represented by dark contrast) are present. As indicated by Figure 3.3A, for samples prepared for less than ~30 min the lower regions are comprised of the steel substrate.

Images collected on samples rubbed for longer periods of time reveal an evolution in the morphology. After 40 min (Figure 3.5B) the surface coverage increases dramatically, and is highlighted by smooth continuous regions that are elongated in the sliding direction (left of the image), and more rough and discontinuous regions (right of the image). Also present on the surface are high, nodular structures that are likely wear debris. An additional 20 min of rubbing imparts yet further morphological changes (Figure 3.5C). A network of larger irregular islands and smaller pads, elongated in the sliding direction, characterizes the surface rubbed for 60 min. Finally after 120 min of rubbing (Figure 3.5D) the surface transforms into a densely packed series of pads that are concatenated in the sliding direction, and form an almost complete film over the underlying substrate. The majority of the grains are less than 5 μm in diameter while a number of larger grains are also present. Once again wear

debris is present on the surface and can be differentiated from the film topographically. After 120 min of rubbing, the morphology of the tribofilms is invariant with time and resembles Figure 3.5D.

The images in Figure 3.5 are representative of the general trend in the morphology of the tribofilms with rubbing time. These trends were observed on a number of samples prepared in the similar manner on different days. A point worthy of note however, is that tribofilm samples prepared in a wear tester can exhibit a marked degree of topographic heterogeneity from spot to spot. This is especially true for films formed for intermediate periods of time, whereas films prepared for short or long periods of time (5 and 120 min respectively) are generally more uniform. To illustrate this point further, several images were collected randomly from the rubbed region on the 40 min sample and are presented in Figure 3.6. In Figure 3.6A, the pads are visible towards the right half of the image, but have not formed throughout the other regions in the image. Figure 3.6B is a reproduction of Figure 3.5B and represents the morphology of the 40 min throughout the majority of the surface. In Figure 3.6C however, large topographic features are present along with smaller pads that have formed on the wear tracks, which measure approximately 25 μm in length and are an imprint of the machine marks from the reciprocating pin. In the region depicted by Figure 3.6D, although some material is present on the surface and wear tracks can be identified, the pads have not formed. The heterogeneity in morphology in some films is most likely due to the contact geometry between the

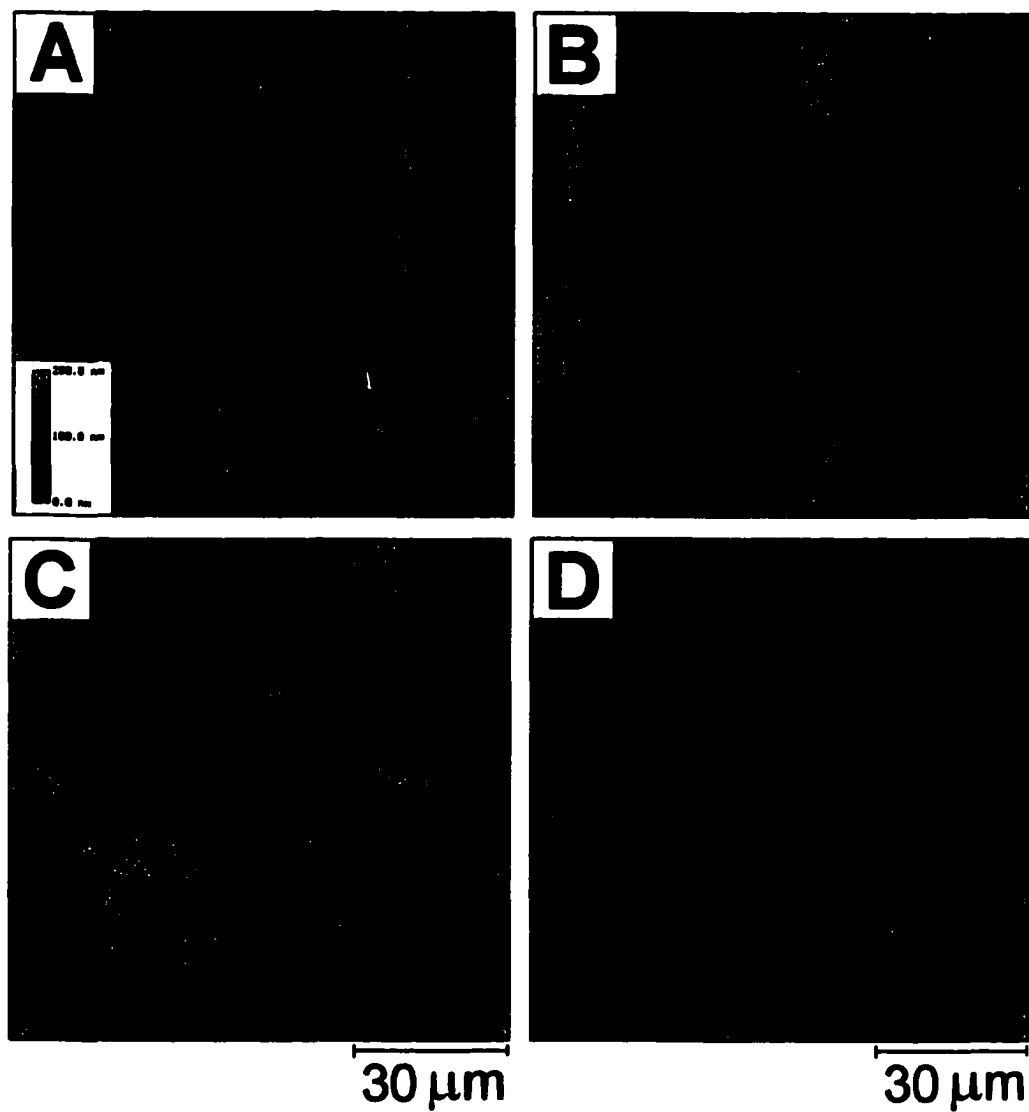


Figure 3.6. Topographic $100 \times 100 \mu\text{m}$ contact mode SFM images (z-scale = 200 nm) of the 40 min. tribofilm illustrating the morphological heterogeneity on different regions of the film. The inset in panel A represents the color scheme for the z-scale on all the images.

pin and the coupon in the Cameron-Plint wear tester. We have found that a slight misalignment in the setup of the pin will result in the absence of a tribofilm.

From the SFM images, a general model for the effect of rubbing time on the morphology of the tribofilms may be formulated and described by three stages. In the first stage, the growth mechanism begins with distinct nucleation events on active sites at the steel surface leading to distinct segregated pads. These nucleation events may be initiated from adsorption of ZDDP or a chemical interaction between ZDDP or decomposition products of ZDDP and iron oxide moieties on the steel surface. The other, and perhaps more likely, scenario is that the nucleation sites are defined by micro-asperities at the surface. The initial nucleation sites grow to form the isolated pads after 5 or 10 min of rubbing. In the second stage, the pads continue to grow and coalesce such that after 30 - 40 min of rubbing, a complete tribofilm forms over the surface. At this time scale, and perhaps even earlier, the morphological characteristics of the tribofilm become dependent on the contact geometry. This statement is validated in the anisotropy associated with the morphology of the tribofilm, where the majority of the pads are preferentially oriented in the sliding direction. In the final stage, the continuous rubbing of the surfaces causes shearing and spreading of the tribofilm to form progressively smaller ($< 5\mu\text{m}$) pads after 60 and 120 min of rubbing. The formation of small pads at long rubbing times was observed on several samples prepared on different days.

As was pointed out, the morphology of the final film is vital when evaluating antiwear performance. These images reveal that a film formed from 5

or 10 min of rubbing will provide good wear protection if most of the load is carried on the pads. The films formed after 40 min should provide even superior wear protection as the surface coverage approaches 100 percent.

2. Nanomechanical properties as a function of rubbing time

Next I evaluate the nanomechanical properties of the tribofilms as a function of rubbing time. In the study of nanomechanical properties, two important parameters will be evaluated. The first is the modulus of elasticity (E), which is proportional to the force required to deform a sample elastically. The indentation modulus ($E^* = E/(1-\nu^2)$) will be reported since the Poisson ratio (ν) is not known for the films. The second parameter is the hardness (H), which is a measure of a material's resistance to plastic flow. In predicting the overall deformation characteristic of the films, the ratio of the indentation modulus to the hardness, E/H will also be evaluated, as was first suggested by Oberle [27], and which has been the basis of the plasticity index [28]. It is generally desirable for boundary films to have a low E/H ratio so that most frictional energy is accommodated by elastic deformations, with negligible plastic flow.

Each sample was first imaged with the Triboscope nanoindenter using a diamond cube-corner tip ($E = 1100$ GPa, $\nu = 0.07$) to generate a topographic contour of the surface before performing the indent over a feature of interest. Figure 3.7 is topographic image of a 10 min tribofilm obtained with the SFM – nanoindenter assembly. The pads are well resolved and can be differentiated from one another. The ability to map the mechanical properties of a surface on

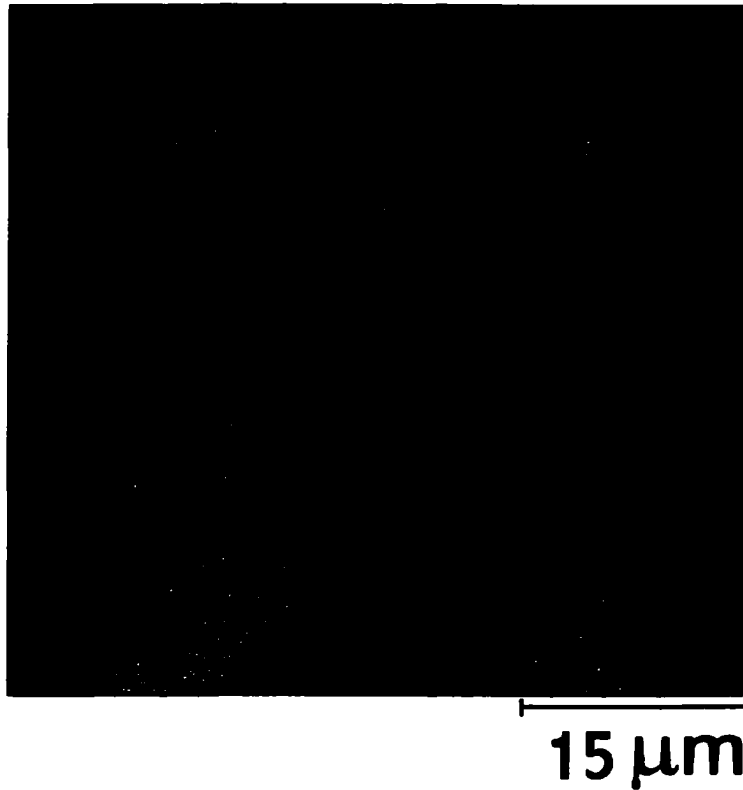


Figure 3.7. Topographic $50 \times 50 \mu\text{m}$ image (z -scale = 300 nm) of a 10 min. tribofilm obtained with the nanoindentation system using a cube corner diamond tip.

the microscopic scale requires that the lateral resolution of instrumentation be better than the smallest features on the surface. The image in Figure 3.7 demonstrates that the SFM – nanoindenter used in these experiments satisfies this requirement.

In Figure 3.8, a series of nanoindentations carried over the film region on each sample is shown, where curves B and C correspond to the 120 min and 10 min tribofilms, respectively. Also for comparison, the nanoindentation profile of the steel substrate is presented by curve A. For clarity, profiles for films prepared for 5, 40 and 60 min films are omitted because they essentially retrace curve B and C. Using the method of Oliver and Pharr, and a Poisson ratio (ν) of 0.3 [29], E of the steel substrate is 214 ± 21 GPa, a value statistically equivalent to the literature value of 207 GPa for stainless steel [29]. The indentation moduli of all tribofilms are listed in Table 3.1. These values are consistent with the reported indentation modulus of a tribofilm formed from 60 min of rubbing [23, 24] and are within the range of known polymeric glass materials [29].

Figure 3.8 and Table 3.1 generate three points that are worthy of note. First, the tribofilms exhibit lower elastic constant than the steel substrate, and should therefore strain plastically under load before the substrate. This leads to the film's sacrificial nature. A second result is that the average indentation moduli of all the tribofilm samples are identical at the 95 % confidence interval (Student's t distribution). That is, the nanomechanical properties of ZDDP tribofilms are for the most part independent of the time in which the surfaces are in tribological contact. This was not anticipated in part because XANES results

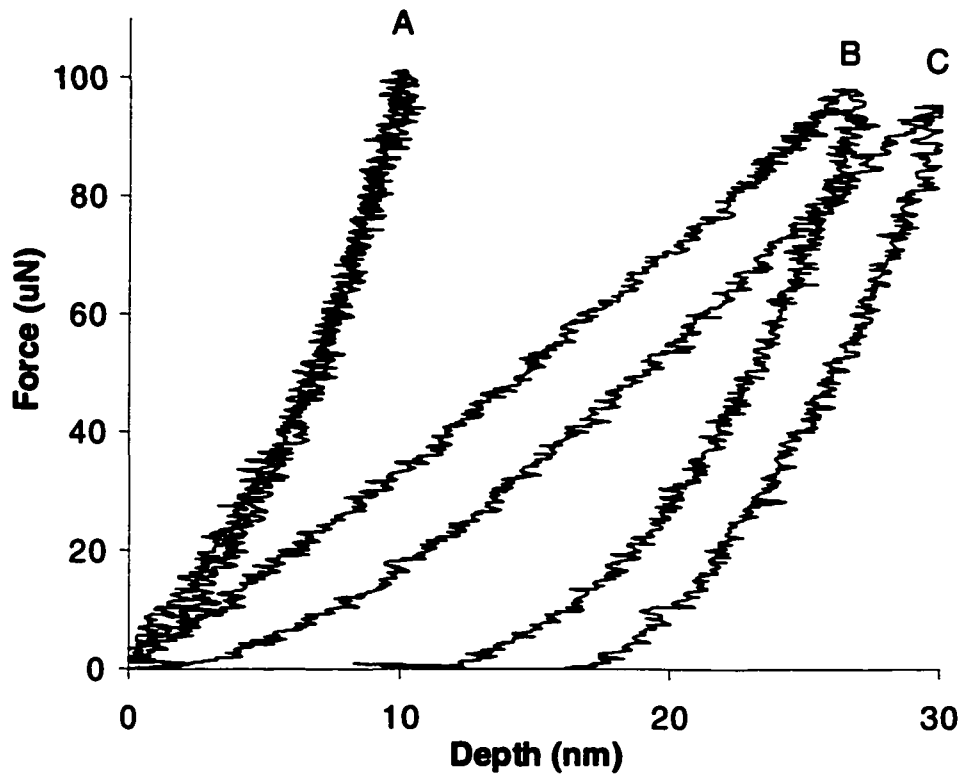


Figure 3.8. Nanoindentation profiles up to a maximum force of 100 μN of (A) steel substrate, (B) 120 min. film and (C) 10 min. film.

Table 3.1. Indentation moduli and Hardness of ZDDP tribofilms prepared in a C – P wear tester as function of time (the numbers in brackets indicates the number of indentations from which E^* and H are derived).

Sample	E^* (GPa)	H (GPa)	E^*/H
52100 Steel	214 ± 21.3^1 (7)	15.6 ± 1.3	13.7 ± 1.8^1
5 min Tribofilm	88.5 ± 23.7 (16)	3.4 ± 1.4	26.0 ± 10.9
10 min Tribofilm	92.8 ± 18.6 (10)	5.0 ± 0.9	18.6 ± 5.0
40 min Tribofilm	88.6 ± 29.9 (15)	2.3 ± 0.6	38.5 ± 16.4
60 min Tribofilm	88.9 ± 12.1 (16)	3.4 ± 0.6	26.1 ± 5.8
120 min Tribofilm	96.1 ± 25.7 (15)	3.9 ± 1.0	24.6 ± 9.1
3 h. Thermal Film	34.8 ± 9.7 (6)	1.5 ± 0.2	23.2 ± 7.2

1. For the steel substrate, the elastic modulus (E) is shown.

have indicated that the surface of ZDDP films varies in composition with rubbing time [14]. Our indentation results are more consistent with what is known about the bulk of the films, which is composed of a short chain polyphosphate structure that is relatively invariant with rubbing time [14].

The third point deals with the high standard deviation in E^* for each film listed in Table 3.1. The indentation profiles in Figure 3.8 are representative of many different regions on each sample. However the relatively large standard deviations (20 - 30 %) in Table 1 reflect the degree of variance in the nanomechanical response from spot-to-spot on the samples. This behavior is better illustrated by the nanoindentation profiles in Figure 3.9. Curve A is the profile representing the majority of the 5 min tribofilm, with an average indentation modulus of 88 GPa. Curve B is another profile measured on the same film. For comparison, an indentation profile of a thermal ZDDP film that was formed from 3 h. of static immersion of a steel coupon in a heated oil bath of ZDDP is also shown (curve C). The large difference between profile A and B illustrates the heterogeneity of the surface with respect to nanomechanical properties for the 5 min film. The softer material from which profile B is compiled ($E^* = 50.2$) is either unreacted ZDDP or a transition material exhibiting properties that lie between a thermal ZDDP film (curve C) and a fully formed tribofilm. The large change in slope at approximately 23 nm in curve B likely results from layers with different mechanical properties comprising the film in this region, that is, a hard layer deposited on top of a more compliant base. The large variation in measured E^* values is attributed to the heterogeneity on contact pressures

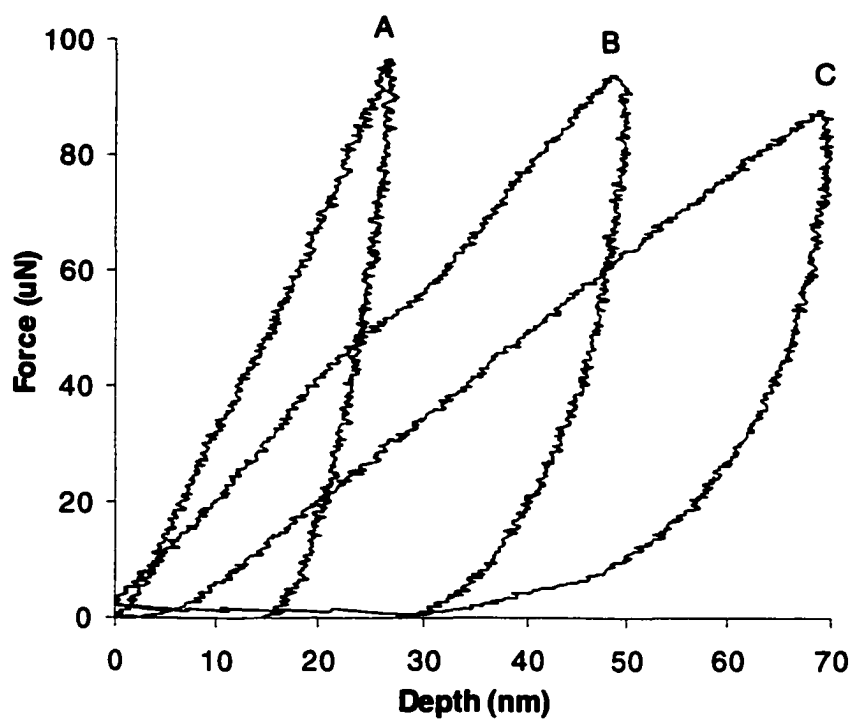


Figure 3.9. (A) and (B) Nanoindentation profiles from different regions of a 5 min. tribofilm. (C) The profile of a thermo-oxidative ZDDP film formed from 3 h. static immersion of a steel coupon in a heated oil bath containing ZDDP.

generated at the interface of the microscopically rough pin and coupon.

After considering the high variability in our nanoindentation results, I employed the imaging capability of the nanoindenter to select specific locations on a pad and to probe for nanomechanical heterogeneity across the pads, as was reported by Graham et al. [24]. For this analysis the 10 min tribofilm was studied because the surface features were well resolved with respect to the resolution of the instrument. Several indents were performed across a number of pads and all generated very similar nanoindentation profiles. In each case the indentation modulus did not vary statistically from the average value of 93GPa. Indentations were also performed in regions between the pads (i.e. regions of low topography), which yielded nanoindentation profiles resembling the steel substrate. It is possible that the radius of curvature of the cube-corner diamond tip is too large to spatially resolve any nanomechanical differences across the pads. Similar experiments performed on the 120 min tribofilm also did not reveal spatially segregated differences in mechanical properties. We note that the error interval derived from indents on a single pad is much lower than the error intervals in Table 3.1, which represents indents from several different pads on each sample.

A general description of the overall mechanical properties of the films can be formulated by considering the ratio of the modulus to the hardness (E^*/H). The hardness values were calculated from the nanoindentation profiles of each sample and are listed in Table 3.1 along with E^*/H values. An average value for E^*/H of 27, for the five tribofilms is determined that is characteristic of relatively

soft materials and modest indentation modulus. By comparison, hardness coatings such as TiAlN have an E/H ratio of 5 [30]. These differences must reflect the mechanism by which the two coatings provide wear protection. In the case of hardness coatings, one desires that the deformation characteristics be highly elastic with only minor plastic flow. ZDDP derived tribofilms are however continuously formed and consumed at the interface of the metal contacts. In this situation a substantial degree of plastic flow will be desired, similar to soft metal coatings that sacrifice themselves in the place of a harder substrate [31].

Depending on the application, effective boundary films may exhibit very distinct mechanical properties. Either the film must be extremely hard so that frictional energy is dissipated by mostly elastic asperity contacts, or it must be susceptible to high plastic flow to be sacrificed in the place of the underlying substrate. Our data shows that ZDDP tribofilms are characteristic of materials that exhibit high plasticity, consistent with past knowledge of the sacrificial nature of the films. Another essential feature of a sacrificial film is that it must accommodate frictional energy through easily sheared layers with respect to the underlying substrate. For most materials the shear modulus, G , can be approximated by the relationship $G \approx 0.4E$ [29]. Using this approximation the shear modulus of the tribofilms is between 35-40 GPa - about half the shear modulus of steel.

3. Effect of soot impurities on the tribofilms.

Soot is a by-product of the incomplete combustion of hydrocarbon fuels and is a major cause of automotive engine wear. Soot consists of agglomerates of carbonaceous particles with dimensions varying from 20 – 500 nm in diameter depending on the formation process [32, 33]. Elemental analysis has shown soot to consist of primarily C, H, and O with traces of Ca, Zn, P, and S. Three mechanisms have been proposed to explain why soot promotes wear. The first mechanism states that soot particles act as abrasives to remove the protective antiwear film from the surface [34]. The second mechanism proposes that ZDDP and its decomposition products irreversibly adsorb onto soot particles in a process that depletes ZDDP from solution [35]. And finally it has also been proposed that soot modifies the physical and mechanical properties of the antiwear films by co-adsorbing with ZDDP on the surface and becoming incorporated in the antiwear film [33]. In this next section we will describe some preliminary SFM and nanoindentation results that support the first and third mechanisms as plausible explanations for the detrimental effect of soot on engines.

The effect of soot was studied by preparing films in a C – P wear tester in the presence of a known concentration of ZDDP and soot in base oil. Figure 3.10A is a topographic image of a coupon rubbed for 1 h. in a blend containing 1.5 and 3.5 weight percent ZDDP and soot respectively. Figure 3.10B is a topographic image of a standard 40 min tribofilm that has subsequently been rubbed in blend containing 1.5 weight percent ZDDP and 3.5 weight percent soot

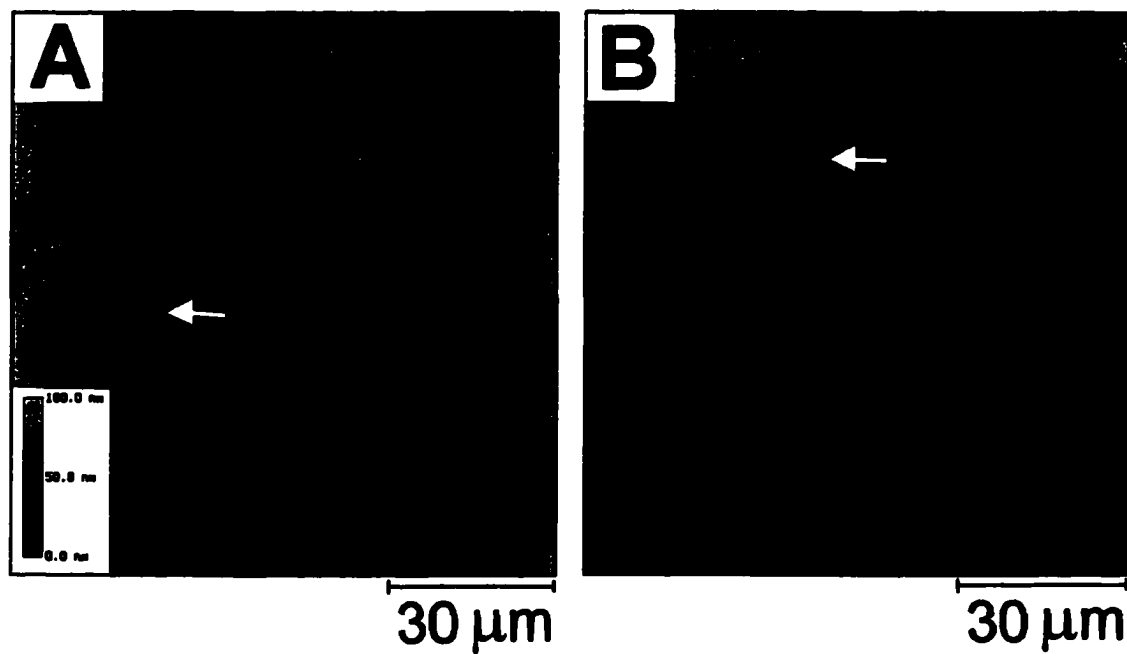


Figure 3.10. (A) Topographic $100 \times 100 \mu\text{m}$ SFM image (z -scale = 100 nm) of a steel coupon rubbed in a blend consisting of 1.5 wt.% ZDDP and 3.5 wt.% soot. (B) Topographic $100 \times 100 \mu\text{m}$ SFM image (z -scale = 100 nm) of a 40 min tribofilm rubbed in the presence of a blend consisting of 3.5 wt. % soot.

for 20 min for a total rubbing time of 60 min. Immediately evident from both images is the almost complete absence of the antiwear film from the surface as compared to a standard 60 min tribofilm (see Figure 3.5). However ridges corresponding to the antiwear film are present on both samples and are marked by arrows. These ridges are aligned in the direction of sliding, which runs from top to bottom on the images. The regions lower in topography are exposed steel where scratch marks also running in the direction of sliding are also discernible. As well, both surfaces are riddled with holes and cavities, which may be a result of wear damage. Interestingly in Figure 3.10A, a series of uniformly sized particles (~ 1 μm in diameter) that are segregated in a circular domain to the right of the image. It is possible that these are aggregate soot particles. The particles were stable to imaging forces of up to 100 nN suggesting strong adhesion to the surface.

The depletion in the amount of film as revealed by the images in Figure 3.10 is conclusive evidence for the abrasion theory of soot induced wear. This is especially true in Figure 3.10B where a previously formed tribofilm is almost completely displaced by rubbing for 20 min in the presence of soot. While the abrasion theory is substantiated it is important to point out that these results do not preclude the theory of adsorption of ZDDP to the soot particles. Adsorption of ZDDP onto the soot particles may be operative in conjunction with the abrasive action of soot. A control experiment was conducted (not shown) whereby a previously deposited antiwear film was rubbed in pure base stock oil

(i.e. no soot present) and there was no evidence of film removal. Thus the removal of the antiwear film is a result of the action of soot.

The nanomechanical properties of the antiwear film remaining on the samples were determined by nanoindentation. Curve A represents a region where the antiwear film is absent and yields an indentation modulus of 212 GPa similar to that of the substrate. Curve B and C of Figure 3.11 are nanoindentation profiles collected from the film regions in Figure 3.10A and B respectively. Curve D is the nanoindentation profile of a standard 60 min tribofilm prepared in the absence of soot. Two important points arise from the plots in Figure 3.11. First the films prepared in the presence of soot exhibit higher mechanical strength than the standard tribofilm. The indentation moduli calculated from curves B and C are 170 and 149 GPa respectively. The indentation modulus of the 60 min tribofilm (curve D) is approximately 90 GPa as before. The second point of interest is the similarity in the mechanical response of the soot samples (curves B and C) even though they were prepared differently. It should be noted that careful attention was given to make certain that the indentations were not influenced by the underlying substrate. Such an effect would manifest itself as a large slope change in the nanoindentation profile.

The nanoindentation results support the mechanism of Berbezier et al. who proposed that the physical and mechanical properties of the tribofilms are modified by the presence of soot. It is difficult to foresee that the stiffer response is a result of changes in the chemical composition of the films because soot is a

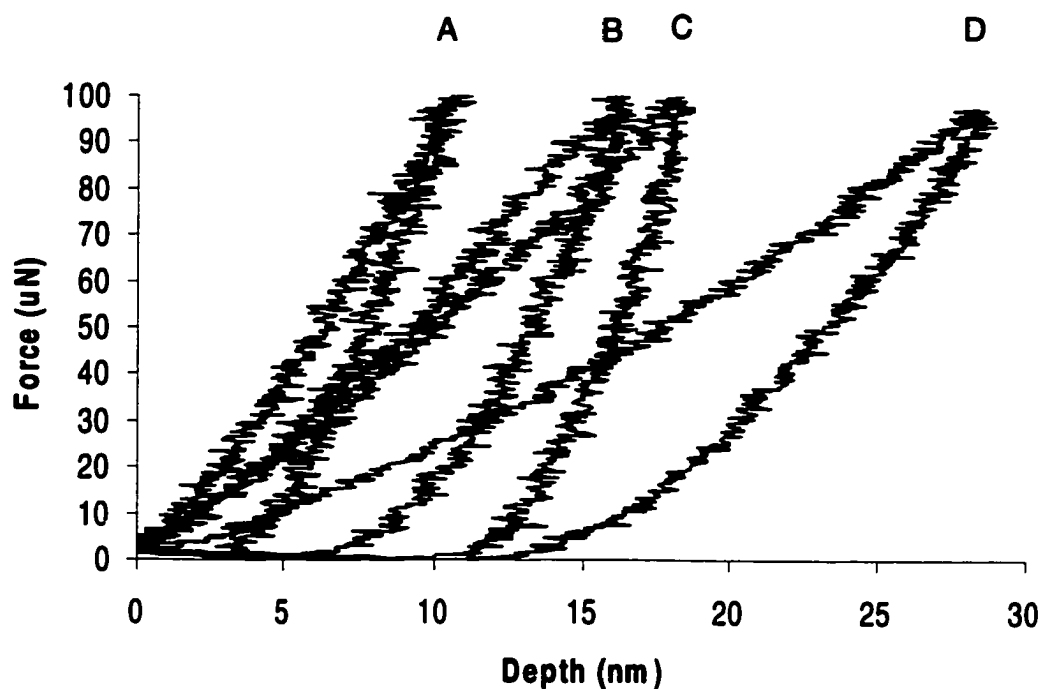


Figure 3.11. Nanoindentation profiles of film prepared in the presence of soot particles. Curve A and C are from regions of low and high topography of a 40 min tribofilm rubbed in the presence of soot. Curve B is from a 60 min film prepared from a blend containing ZDDP and soot. Curve D is a 60 min tribofilm.

relatively inert material. However it is possible to envisage that the greater mechanical strength is a result of the inclusion of soot particles in the polyphosphate film matrix. Soot is regarded to be a hard material [36] with Rockwell Hardness (R.H.) values ranging from 30 – 60 [37]. By comparison the R.H. of Fe_2O_3 and Al_2O_3 is 51 and 70 respectively [37]. Thus the incorporation of a hard material such as soot in the matrix of the antiwear film will give rise to a stiffer response. Attempts were made to find individual soot particles with the nanoindenter in the hope of measuring their elasticity. However repeated trials were unsuccessful as the particles could not be located with the diamond tip.

The combined SFM and nanoindentation studies lead to two major conclusions. The first is that soot is indeed a “pro-wear” agent such that the antiwear capabilities of ZDDP are dramatically reduced when soot is present in the lubrication blend. The abrasion theory is at least one mechanism that plays a role, although the adsorption theory cannot be ruled out by our results. The nanoindentation results suggest that the mechanism whereby soot modifies the properties of the antiwear is also operative. The film regions on samples prepared in the presence of soot are mechanically stiffer than standard tribofilms. We propose that stiffness is a result of the inclusion of soot in the polyphosphate film matrix. A preliminary XPS survey of tribofilms prepared in the presence of soot indicate a larger carbon content versus tribofilms prepared from neat ZDDP blends. Although soot is a primary cause of engine wear, it is interesting that a mechanically stronger antiwear film forms in its presence. The latter effect is

however completely outweighed by the depletion in the amount of film material on the surface.

4. Effect of sliding speed on the tribofilms.

Sliding speed is an important parameter in hydrodynamic lubrication as was pointed out in Chapter I. In this section we present some very preliminary results to argue that sliding speed has an effect on the morphology of ZDDP tribofilms. This will also serve as a means to gauge the effect of local interfacial temperature on the tribofilm. A sample was prepared under the same condition as those in Figure 3.5 with the difference that the reciprocating frequency was lowered to 10 Hz from the standard 25 Hz. Figure 3.12A and B are topographic SFM images of a 2 h. tribofilm rubbed at a sliding frequency of 10 Hz. The film does not exhibit the distinct grain structure that was observed in the 2 h. film formed at 25 Hz (Figure 3.5A) and is instead morphologically more heterogeneous. In a number of regions pad-like structures have formed, whereas the rest of the film shows no clear definition. Also evident throughout the image is a series of particles with diameters of less than 1 μm , that appear to be wear debris. Using Rabinowicz's approximation [38], with the assumption that all other variables are constant, the temperature rise of two steel contacts is related to their rubbing velocity by $0.75\text{ }^{\circ}\text{C}/\text{cm}/\text{sec}$. This value is used as a first approximation to calculate the temperature differences between films formed at 10 and 25 Hz. If it is assumed that the pin travels a distance of 1 cm over the coupon (from the macroscopic dimensions of the tribofilm), the rubbing velocity will equal $(2 \times 1\text{ cm} \times 10\text{ Hz})$ 20 cm/sec, while at 25 Hz, the velocity will be 50

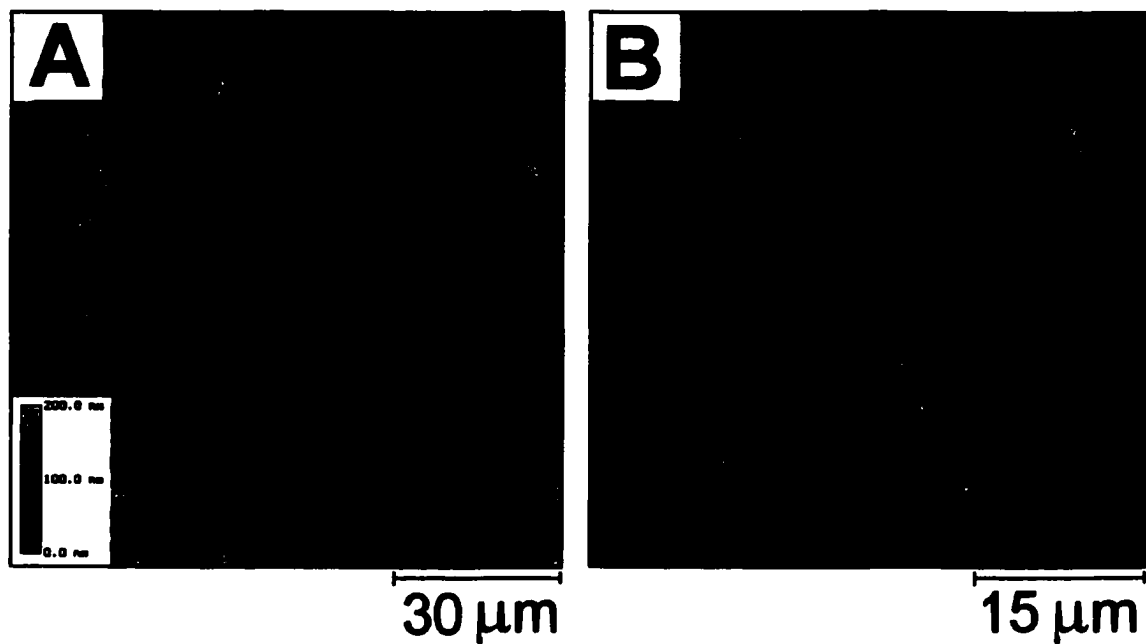


Figure 3.12. Panel A is a topographic $100 \times 100 \mu\text{m}$ (z-scale = 200 nm) SFM image of a tribofilm prepared from 2 h. of rubbing at a reciprocating frequency of 10 Hz. Panel B is a $50 \times 50 \mu\text{m}$ (z-scale = 200 nm) of the same sample. The inset in panel A represents the color scheme for the z-scale on both images.

cm/sec. This will yield an interfacial temperature difference of $(0.75^{\circ}\text{C} / \text{cm/sec} \times 30 \text{ cm/s}) 23^{\circ}\text{C}$. The contrast in the morphology of the films formed at the two frequencies may be in part, due to the temperature difference at the interface of the metal contacts. These results are preliminary and more work will be required to fully understand the effect of rubbing frequency on the morphological characteristics of the tribofilms. The SFM images in Figure 3.12 are however evidence that sliding speed does influence the morphology of the tribofilms to some degree. Nanoindentation experiments of the tribofilm resulted in profiles that essentially retraced those of film formed at 25 Hz. Thus the sliding speed does not appear to affect the mechanical properties of the films.

Conclusions

I have shown that the morphology of ZDDP derived tribofilms evolve with rubbing time, such that at lower times, distinct segregated pads form, which at longer times transform to a more even and morphologically smoother coating over the steel substrate. Although rubbing time affects the morphology, it was shown through nanoindentation studies that the nanomechanical properties of the film are for the most part unaffected. The indentation modulus and hardness of a tribofilm formed after 5 min are similar to a tribofilm formed from 120 min of rubbing. The tribofilms form very rapidly as evidenced by the observation of a high density of well-formed pads after 5 and 10 min of rubbing (Figures 3.3A and 3.5A). The hardness and indentation moduli are characteristic of soft polymeric materials and rank higher in plasticity as compared to the steel substrate,

consistent with past knowledge about the sacrificial nature of the films. It was also found that both the morphology and nanomechanical properties can vary from spot-to-spot and film-to-film. This is likely due to the heterogeneity in contact pressures when two microscopically rough surfaces are rubbed together.

The effect of soot was shown to markedly decrease the amount of film on the surface. The most likely mechanism appears to be abrasion. The films prepared in the presence of soot were mechanically stiffer than those prepared in the absence of soot. This is a result of the soot particles becoming incorporated in the matrix of the antiwear films.

Preliminary studies showed that sliding velocity influences the morphology of the tribofilms. This may be a result of the lower interfacial temperature at the lower reciprocating frequency. Sliding velocity does not however affect the nanomechanical properties of the tribofilms under these experimental conditions. My next experiments are directed towards evaluating the effect of detergents and dispersants on the morphology and nanomechanical properties of ZDDP tribofilms. These results will be presented in Chapter IV.

Reference:

1. P. A. Willermet, J. M. Pieprzak, D. P. Dailey, R. O. Carter III, N. E. Lindsay, L. P. Hack, and J. E. de Vries, *ASME Trans.* 113:38 (1991).
2. P. A. Willermet, R. O. Carter, and E. N. Boulos, *Tribol. Int.* 25:371 (1992).
3. G. H. Harrison and P. Brown, *Wear* 148:123 (1991).
4. H. Spedding and R. C. Watkins, *Tribol. Int.* 15:9 (1982).

5. B. Cavdar and K. C. Ludema, *Wear* 148:305 (1991).
6. N. E. Lindsay, R. O. Carter III, J. Schmitz, L. P. Haack, R. E. Chase, J. E. de Vries, and P. A. Willermet, *Spectrochimica. Acta.* 49A:2057 (1993).
7. S.-H. Choa, K. C. Ludema, G. E. Potter, B. M. DeKoven, T. A. Morgan, and K. K. Kishore, *Wear* 177:33 (1994).
8. R. J. Bird and G. D. Galvin, *Wear* 37:143 (1976).
9. S. Jahanmir, *J. Tribol.* 109:577 (1987).
10. P. A. Willermet, D. P. Dailey, R. O. Carter III, P. J. Schmitz, W. Zhu, J. C. Bell, and D. Park, *Tribol. Int.* 28:163 (1995).
11. J. C. Bell, K. M. Delargy, and A. M. Seeney, in Proc. 18th Leeds-Lyon Symp. on Tribology, Elsevier, Lyon, France, 1991, p. 387.
12. Z. Yin, M. Kasrai, G. M. Bancroft, K. F. Laycock, and K. H. Tan, *Tribol. Int* 26:383 (1993).
13. G. M. Bancroft, M. Kasrai, M. Fuller, Z. Yin, K. Fyfe, and K. H. Tan, *Tribol. Lett.* 3:47 (1997).
14. Z. Yin, M. Kasrai, M. Fuller, G. M. Bancroft, K. Fyfe, and K. H. Tan, *Wear* 202:172 (1997).
15. M. L. S. Fuller, M. Kasrai, G. M. Bancroft, K. Fyfe, and K. H. Tan, *Tribol. Int.* 31:627 (1998).
16. D. R. Armstrong, E. S. Ferrari, K. J. Roberts, and D. Adams, *Wear* 217:276 (1998).
17. E. S. Ferrari, K. J. Roberts, M. Sansone, and D. Adams, *Wear* 236:259 (1999).

18. M. Kasrai, J. N. Citler, K. Gore, G. Canning, and G. M. Bancroft, *Tribol. Trans.* 41:69 (1998).
19. K. Varlot, M. Kasrai, J. M. Martin, B. Vacher, G. M. Bancroft, E. S. Yamaguchi, and P. R. Ryason, *Trib. Lett.* 8:9 (2000).
20. M. Aktary, M. T. McDermott, and J. Torkelson, *Wear* 247:172 (2001).
21. A. J. Pidduck and G. C. Smith, *Wear* 212:254 (1997).
22. O. L. Warren, J.F. Graham, and P. R. Norton, *Phys. in Can.* March / April:122 (1998).
23. O. L. Warren, J. F. Graham, P. R. Norton, J.E. Houston, and T. A. Michalske, *Tribol. Lett.* 4:189 (1998).
24. J. F. Graham, C. McCague, and P. R. Norton, *Trib. Lett.* 6:149 (1999).
25. G. W. Canning, M. L. S. Fuller, G. M. Bancroft, M. Kasrai, J. N. Cutler, G. De Stasio, and B. Gilbert, *Trib. Lett.* 6:159 (1999).
26. W. C. Oliver and G. M. Pharr, *J. Mater. Res.* 7:1564 (1992).
27. T. L. Oberle, *J. Metals* June:438 (1951).
28. J. A. Greenwood and J. B. P. Williamson, *Proc. Roy. Soc.* A295:300 (1966).
29. W. D. Callister Jr., *Materials Science and Engineering: An Introduction*, John Wiley & Sons, Inc., New York, 1994.
30. A. Leyland and A. Mathews, *Wear* 246:1 (2000).
31. W. A. Glaeser, *Materials For Tribology*, Elsevier, Amsterdam, 1992.
32. F. G. Rounds, *SAE* 810499:1 (1981).
33. I. Berbezier, J. M. Martin, and P. Kapsa, *Tribol. Int.* 19:115 (1986).

34. D. Godfrey, SAE Trans. 87:2870 (1978).
35. F. G. Rounds, SAE 770829:1 (1977).
36. P. R. Ryason, I. Y. Chan, and J. T. Gilmore, Wear 137:15 (1990).
37. R. J. Mayer, in International Tribology Conference, Melbourne, 1987, p. 1.
38. E. Rabinowicz, Friction and Wear of Materials, John Wiley and Sons, Inc., New York, 1965.

Chapter IV

The Effect of Detergents and Dispersants on the Morphology and Nanomechanical Properties of ZDDP Tribofilms

Introduction

Modern engine oil formulations are constituted from numerous additives that include detergents, dispersants, antioxidants, and antiwear agents blended in a matrix of highly refined petroleum oil [1]. The additives maintain a level of cleanliness, oxidation stability, and antiwear action in protecting engines from damage and ensuring their smooth operation [2]. While each additive is designed to function independently, the presence of such a diverse number of chemical species in the same matrix opens the possibility of chemical interactions among the additives. This concern is highlighted by the fact that engine oils operate at high temperatures where chemical reactions are facile. The end result may be a reduction in the potency and effectiveness of the blend as a whole.

Thus far my research efforts have concentrated on employing modern analytical surface techniques to understand the chemical composition, surface morphology, and nanomechanical properties of tribological antiwear films derived from the antiwear agent zinc dialkyldithiophosphate (ZDDP). My preliminary investigations in Chapter II explored the evolution of films formed from the thermooxidative decomposition of ZDDP on Au surfaces [3]. Later studies in Chapter III detailed the effect of physical parameters and impurities on the morphology and nanomechanical properties of films prepared in a Cameron –

Plint (C-P) reciprocating wear rig on steel coupons. The motivation behind my current investigations derives from the fact that certain detergents and dispersant have shown a propensity to interact with and alter the solution phase and tribo chemistry of ZDDP [2, 4-13]. In some reports these interactions have been deemed synergistic [10] while others have argued that the presence of detergents and dispersants is detrimental to the antiwear function of ZDDP [11].

While ZDDP protects engine components from wear by forming sacrificial boundary films at the interface of contact, detergents and dispersants function to prevent oil insoluble by-products of combustion from adsorbing onto the surface of engine components by keeping them in suspension [14]. Detergents are metal salts of organic acids and are prepared from the reaction of metal oxide with an organic acid [15]. They are comprised of a long chain aliphatic (hydrophobic) tail to ensure solubility in the oil and a polar head group that functions to isolate polar contaminants by forming reverse micelles. Their micellar size is small with typical aggregation numbers of 10 - 30 [4]. Examples include Mg, Na and Ca salts of sulphonates, phenates, and salicylates. The structure of several alkylbenzene detergents is shown in Figure 4.1 where M represents a monovalent or divalent cation. Detergent additives may be neutral or overbased where the level of overbasing is a measure of the alkalinity of the additive. The alkalinity is governed by the presence of an excess base in the additive package such as CaCO_3 to neutralize acidic by-products of combustion such as sulfuric and nitric acid.

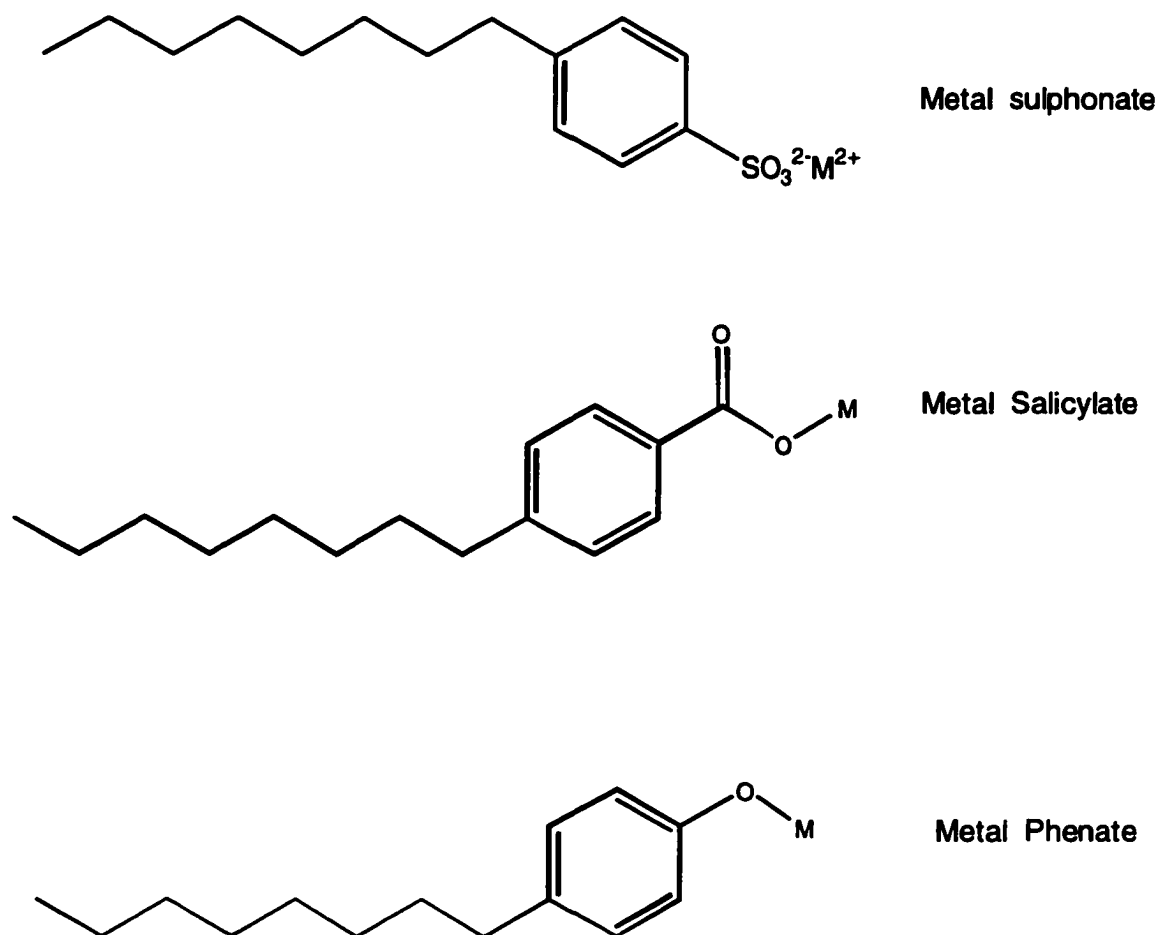


Figure 4.1. Structure of several automotive engine oil detergents where **M** is a monovalent or divalent atom such as Na or Ca.

Dispersants are organic analogues of detergents whose primary function is to prevent the formation of sludge by removing and isolating moisture and soot from the lubricant [15, 16]. Dispersants were developed primarily for colder running gasoline engines because detergents (developed for hotter running diesel engine) were insufficient to prevent water from contaminating the lubricant [1]. Dispersants are also high molecular weight compounds constituted from a hydrophobic tail for solubility and a polar head group that interacts with water by hydrogen bonding. The most widely used dispersant is polyisobutylene succinic anhydride polyamine (PIBSA). This additive is prepared from the reaction of maleic anhydride with polybutene to give polyisobutenyl succinic anhydride, which is further reacted with polyalkylene polyamine to give PIBSA [1, 15]. The structure of PIBSA is presented in Figure 4.2 showing the hydrophilic polyamine head group and the hydrophobic polybutenyl tail while the succinimide moiety acts as a linker.

Two mechanisms have been proposed that describe the interference of detergents and dispersants with the boundary lubricating properties of ZDDP [2, 4, 5]. The first mechanism entails direct chemical association in the solution matrix by means of intermolecular forces such as dipole-dipole interactions and hydrogen bonding leading to complexation and a reduction in the solution concentration of ZDDP. The second mechanism involves competition for adsorption sites on the rubbing surfaces that will result in a reduction in the surface concentration of ZDDP. This mechanism is especially of concern on metal surfaces if the additives are polar [2, 5].

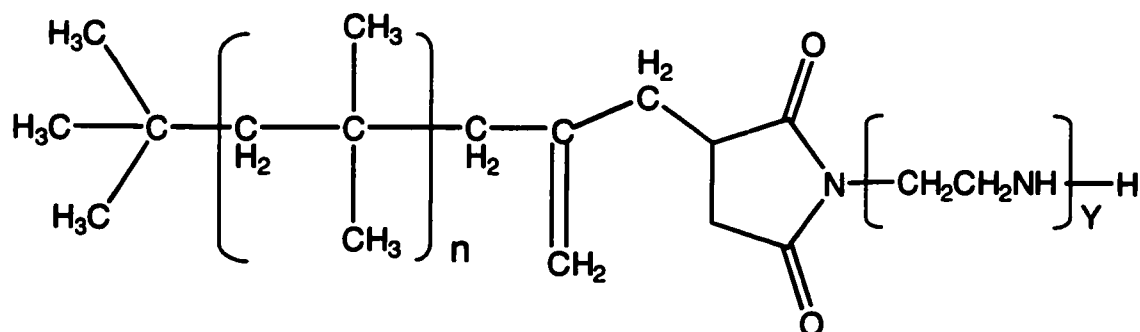


Figure 4.2. Structure of the dispersant polyisobutenyl succinic anhydride polyamine (PIBSA). $n = 11 - 52$.

A well studied system is the interaction of calcium sulphonate detergents with ZDDP. Initially sulphonates were thought to be hostile to the formation of the antiwear film because they retarded the solution phase decomposition of ZDDP [2] and through adsorption studies were shown to be more surface active than ZDDP [4]. Furthermore, empirical wear measurements had shown a larger tendency for material loss when sulphonate was present in the lubrication blend [2, 5]. The effect of an overbased calcium sulphonate detergent on the antiwear action of ZDDP is however not fully understood and some controversy exists. For example it has been proposed that overbasing agents such as CaCO_3 aid the formation of the antiwear film by forming a seeding layer over the contact zone that would catalyze antiwear film formation [5]. In a later study the synergy was associated with the presence of residual calcium hydroxide in the additive package from the synthesis process [10]. The same conclusions were not found in the electric contact resistance studies of Yamaguchi et al. who reported that overbasing agents significantly retard the formation of ZDDP boundary films [11]. Thus, the issue is not fully resolved and more studies are warranted.

Although the issue of synergism and antagonism between sulphonate and ZDDP is not completely understood several independent groups have confirmed that the presence of overbased Ca sulphonate alters the chemical composition of the antiwear films [5, 7, 17, 18]. For example both X-ray and infrared studies of ZDDP films prepared in the presence of overbased Ca sulphonate have shown a reduction in the length of the polyphosphate chains that constitute the films [9, 17]. It was proposed that it is actually Ca from the overbasing agent and not the

detergent that reacts with the polyphosphate film to form species such as Ca phosphate and Ca pyrophosphate [9].

Numerous studies have shown that the dispersant PIBSA significantly retards the formation of ZDDP films through complexation reactions with ZDDP in solution and by adsorbing on acidic sites on metals and carbon [2, 4, 17, 19]. The complexation has been attributed to acid - base interactions between N groups of the dispersant and P groups of ZDDP and also to coordination of N from the polyamine residues to Zn [4, 8]. Still other studies have proposed reactions between ZDDP and the dispersant to produce phosphorodithioates [7]. Recent XANES analysis indicated that films prepared in the presence of PIBSA were much thinner than films prepared from neat ZDDP blends [18]. The study also found that the length of the polyphosphate chain was reduced in the presence of PIBSA.

The aim here is to apply the techniques described in Chapter III to evaluate the extent to which detergent and dispersant additives affect the morphology and nanomechanical properties of ZDDP films. This will be evaluated by preparing films in a Cameron Plint (C – P) reciprocating wear tester from two blends. The first blend will contain ZDDP and an overbased calcium sulphonate detergent and the second blend will contain ZDDP and PIBSA in a concentration range that will reflect commercial engine oil blends.

Experimental

Reagents and materials: A solvent refined base oil with a viscosity at 100°C of about 5 mm²/s (referred to as MCT 10), a commercial ZDDP (15% isooctyl and 85% isobutyl) antiwear additive, a commercial alkyl aryl Ca sulphonate detergent (TBN 300) and a commercial polyisobutenyl succinimide polyalkenylamine (PIBSA) concentrate, along with coupons of 52100 steel were obtained from Imperial Oil (Samia, ON).

Sample Preparation: Sample coupons were polished to a mirror finish with diamond paste and inserted in a Cameron-Plint wear rig. A 1.5 wt.% ZDDP + 2 wt.% Ca sulphonate or 7.0 wt.% PIBSA oil solution in MCT 10 was poured into the sample compartment of the C – P wear tester. The bath temperature was set to 100 °C. A stainless steel pin was then tightened into position and a force of 225 N was applied between the pin and the coupon. The coupon was rubbed at 25 Hz. The coupon was withdrawn after various lengths of time and rinsed with a low-molecular weight hydrocarbon industrial solvent and dried.

SFM imaging: Topographic SFM images were collected using a Nanoscope III (Digital Instruments, Santa Barbara, CA) scanning force microscope (SFM) using triangular Si₃N₄ cantilevers (spring constant, k ~ 0.06 N/m). Images presented here were captured continuously at a scan rate of 7.8-10.2 Hz at a normal force of <10 nN. The images were software flattened and are otherwise shown unfiltered.

Nanoindentation experiments: Nanoindentation experiments were performed with a Triboscope® (Hysitron Inc.) nanomechanical testing instrument

interfaced to a Digital Instrument (Santa Barbara, CA) Dimensions 3100™ scanning probe microscope controller. Refer to Chapter III for details.

SEM and EDX analyses: Secondary electron images and energy dispersive X-ray spectra were collected with a JEOL model 6301FXV scanning electron microscope at accelerating voltages between 5 - 20 kV and a working distance of 4-5 mm.

Results and Discussion

As demonstrated in Chapter III SEM analysis in concert with EDX is an effective means to spatially probe the elemental composition of the antiwear films. The protocol will be similar to that of Chapter III where the samples will first be imaged by the SEM and subsequently analyzed by EDX on localized regions. Panels A and B of Figure 4.3 are SEM images of steel coupons that have been rubbed in a blend of 1.5 weight percent ZDDP and 2 weight percent overbased Ca sulphonate detergent for 5 and 40 min respectively. In the 5 min sample, regions corresponding to the substrate are easily differentiated from the film where, as in Figure 3.3 of Chapter III, the dark regions correspond to the film and the lighter regions to the underlying substrate. This contrast originates from the lower conductivity and atomic number of the elements constituting the film in relation to the substrate. The film coverage after 5 min of rubbing is substantial but not complete, leaving regions of steel exposed. The film coverage increases at 40 min of rubbing (panel B) leaving no regions of the substrate exposed.

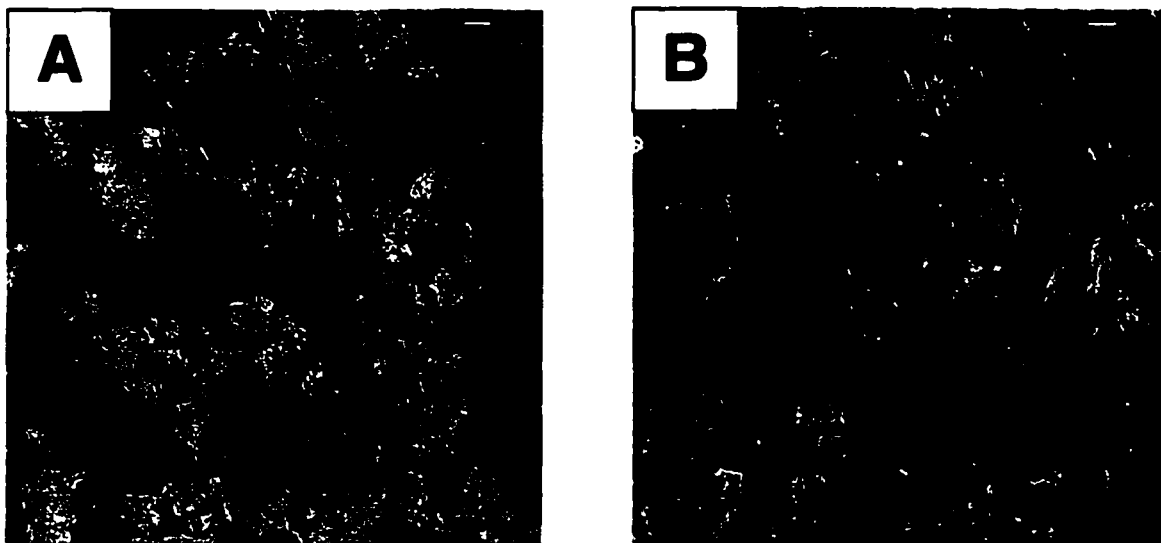


Figure 4.3. SEM images of films prepared from 5 min (panel A) and 40 min (panel B) of rubbing in a lubrication blend consisting of 1.5 wt.% ZDDP + 2.0 wt.% overbased Ca sulphonate detergent. Scale bar = 1 μm .

EDX spectra were collected from selected regions of the surface and the results are presented in Figure 4.4. Spectra A and B correspond to the film regions of the 5 and 40 min samples respectively. The dominant peaks in the spectra are the Fe and Cr K_{α} lines originating from the underlying steel substrate. Also present in the spectra are the P, S, and Zn lines that originate from the ZDDP precursor as before. The novel feature of the spectra is the Ca line at 3.8 keV, verifying that Ca (or Ca^{2+}) is incorporated throughout the films. Either Ca is embedded in the film as colloidal $CaCO_3$ particles as proposed by Kapsa et al. [5] or Ca is chemically bonded to the phosphate film in the form of $Ca_2P_2O_7$ and $Ca(PO_3)_2$ [6, 9, 17]. EDX analysis of the exposed substrate regions in the 5 min film (not shown) revealed detectable amounts of Ca and S. Adsorption isotherms have shown that detergents are very surface active [4] and the presence of Ca and S on these regions is attributed to physisorbed Ca sulphonate. Therefore it is likely that the steel surface is coated with a layer of detergent before the antiwear films of ZDDP begin to form.

The effect of Ca sulphonate on the morphology of ZDDP films at different intervals of rubbing time was investigated by SFM. Figure 4.5A – C are 50 x 50 μm topographic SFM images of films rubbed for 5, 40, and 120 min respectively. The morphology of the 5 min film consists mainly of pads that measure approximately 5 μm in diameter and are 200 nm thick. The majority of pads are elongated tangential to the sliding direction of the pin over the coupon, which runs from top to bottom on the images. The coverage is substantial but not complete where regions low in topography (dark contrast) that correspond to the

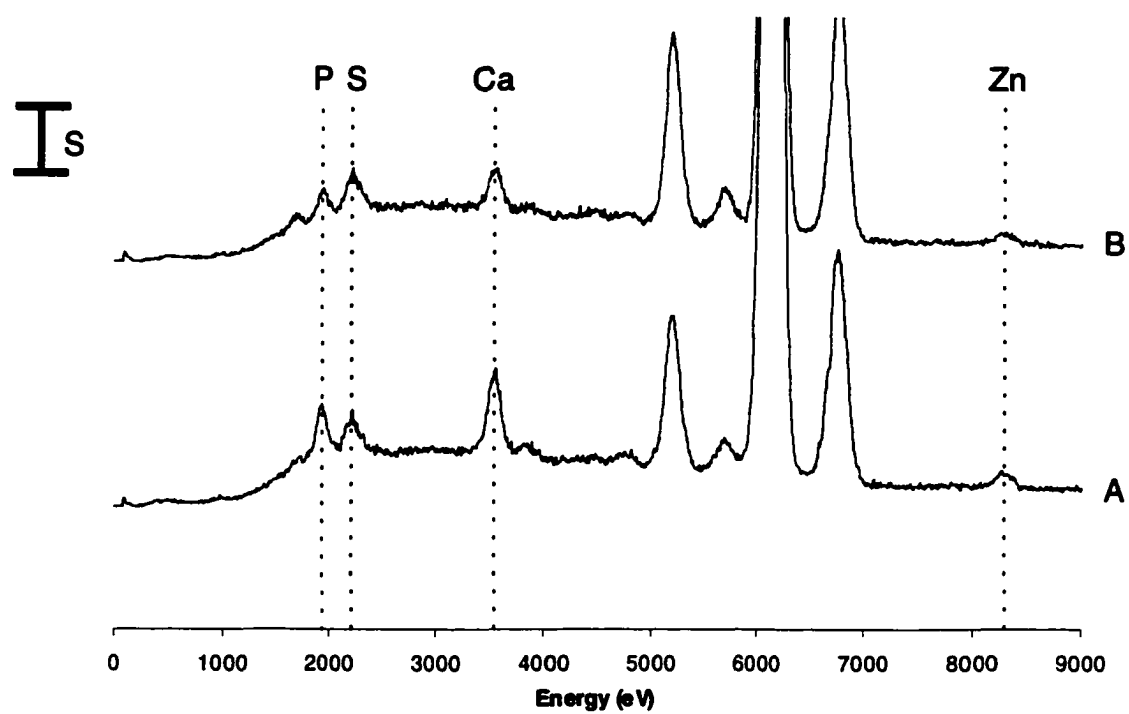


Figure 4.4. EDX spectra of film prepared from a blend consisting of 1.5 wt.% ZDDP + 2 wt.% overbased Ca sulphonate rubbed for 5 min (spectrum A) and 40 min (spectrum B). $S = 500$ counts.

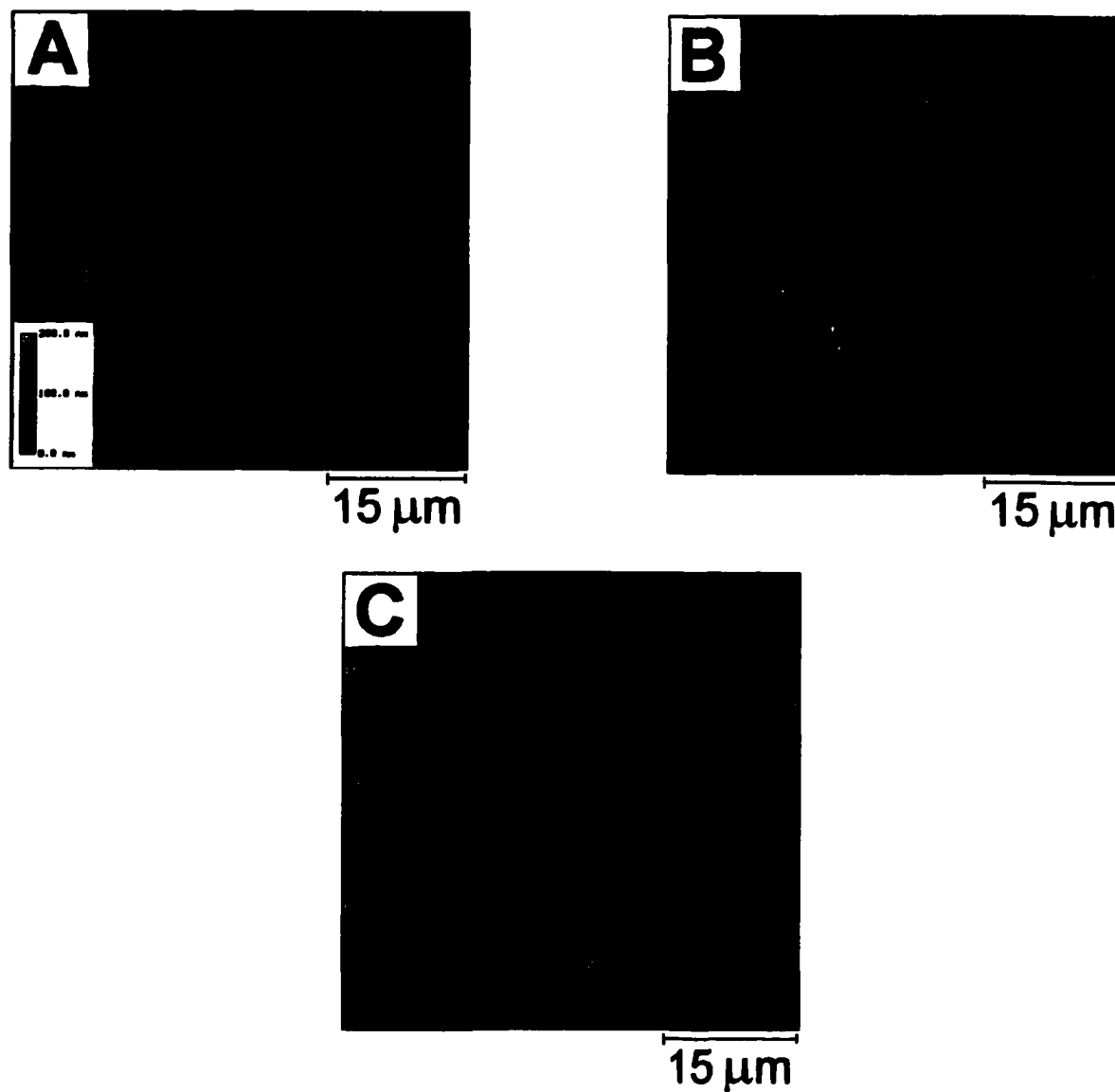


Figure 4.5. Topographic 50 x 50 μm SFM images (z-scale = 200 nm) of films prepared in a blend consisting of 1.5 wt.% ZDDP + 2 wt.% Ca sulphonate rubbed for: (A) 5 min (B) 40 min (C) 120 min. The inset in panel A represents the color scheme for the z-scale on all the images.

exposed substrate are present throughout, consistent with the SEM image in Figure 4.3A. An important feature revealed by Figure 4.5A is that the film coverage is comparable to neat ZDDP films formed from 5 – 10 min of rubbing (e.g. Figure 3.3A and 3.5A). Therefore based solely on the grounds of film structure and coverage, the antagonism theory [2] between overbased Ca sulphonate and ZDDP may be ruled out. Instead the results imply synergism and affirm the theory of Rounds who proposed that overbased sulphonate detergents aid the antiwear action of ZDDP [10].

The films prepared from 40 and 120 min of rubbing (panels B and C, Figure 4.5) are morphologically similar where the pads have coalesced from the 5 min interval to form a more homogeneous coating over the steel substrate. The films exhibit a marked degree of unevenness at the 50 μm field of view as evidenced by regions of low and high topography throughout the images. The root mean square roughness (RMS) of the 40 and 120 min films are 39 and 46 nm respectively, and slightly higher than the 5 min tribofilm (RMS = 36 nm). Regions lower in topography in the images are not exposed steel because the film coverage is nearly complete after 40 min of rubbing (Figure 4.3B). These images reveal that the morphology of the films evolves in the early stages of rubbing and remains constant after 40 min. The overriding conclusion from the SEM and SFM images is that overbased Ca sulphonate does not hamper the ability of ZDDP to form effective antiwear films.

Conclusions with respect to the antiwear action of ZDDP in the presence of detergents are not complete solely on morphological grounds because the

nanomechanical response of the films under load plays a crucial role in wear protection. It has been proposed and shown by EDX analysis that Ca is incorporated in the film. In this next section nanoindentation will be employed to evaluate whether changes in the chemical composition of the films brought about by the overbased detergent has any effect on the nanomechanical properties of the films.

Several indents were executed on topographically high features on the entire samples using triangular and trapezoid load functions. The maximum indentation force was 100 μN in all cases. Using the compliance method of Oliver et al. [20] the indentation modulus ($E^* = E/(1-\nu^2)$) of each sample was calculated and is presented in Table 4.1. Comparison of the E^* values in Table 4.1 with films prepared from neat ZDDP solutions in Chapter III indicates a larger average E^* at all time intervals within a 95 % confidence (Student's t distribution) interval except for the 120 min films. For these samples the mean E^* is differentiable at the 80 % confidence interval. The relative error is between 10-20 % for all the values and reflects both the heterogeneity of the samples and problems associated with surface roughness and pile up on the calculations. The stiffer response of the films in relation to those prepared from neat ZDDP is especially pronounced for the 40 min sample where the average E^* was 127 GPa. The nanoindentation profile of the 40 min film is presented as curve A in Figure 4.6 against the more compliant ZDDP film from Chapter III in curve B with $E^* = 88$ GPa. I propose that the enhanced stiffness as illustrated by Curve A

Table 4.1. Indentation moduli of ZDDP tribofilms prepared in the presence of 2.0 wt. % Ca sulphonate detergent, 7.0 wt. % PIBSA dispersant, and 1.5 wt. % ZDDP as a function of rubbing time in a C – P wear tester. The brackets indicate the number of indents from which the average moduli were determined.

Time (min)	ZDDP + Ca Sulphonate	ZDDP + PIBSA	ZDDP
5	112 ± 17 (18)	98 ± 11 (11)	88.5 ± 23.7 (16)
20	120 ± 16 (15)	***	***
40	127 ± 16 (17)	102 ± 14 (7)	88.6 ± 29.9 (15)
60	***	102 ± 9 (13)	88.9 ± 12.1 (16)
120	109 ± 25 (15)	114 ± 14 (16)	96.1 ± 25.7 (15)

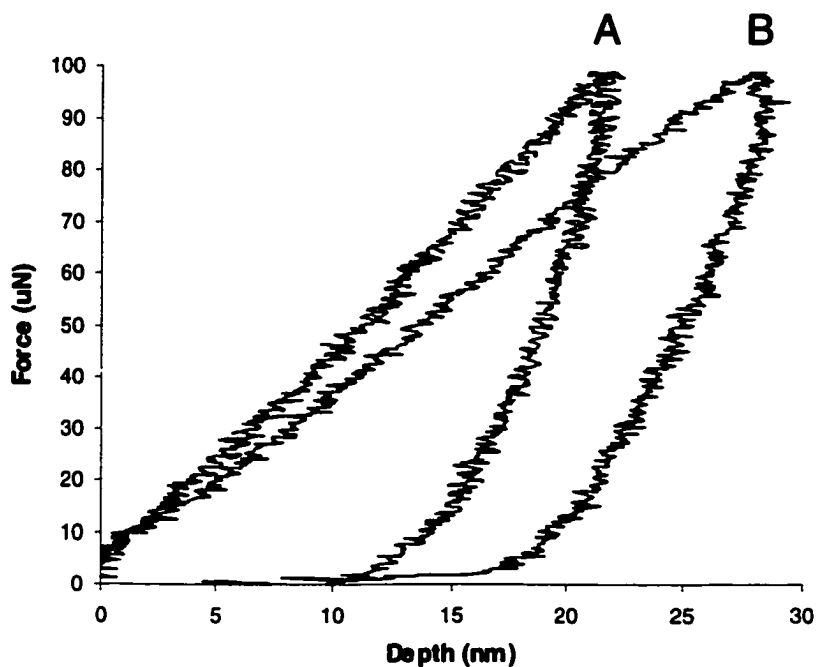


Figure 4.6. Nanoindentation profiles of ZDDP films prepared from 40 min. of rubbing in the presence (curve A) and absence (curve B) of overbased Ca sulphonate.

derives from the presence of Ca in the films that originates from the detergent in the lubricant. The Ca is either present as CaCO_3 particles interspersed in the film and /or results from the transformation of the long chain polyphosphate film to species such as CaP_2O_7 and $\text{Ca}_3(\text{PO}_3)_2$. One may also speculate that the increased stiffness results from an increase in the ordering of the polyphosphate chains after reacting with Ca^{2+} to form shorter chain polyphosphates.

Effect of Dispersants on ZDDP Films

PIBSA is a popular dispersant additive in engine oil blends that helps to isolate moisture and prevent formation of soot and sludge. The dispersant is known to primarily reduce the solution concentration of ZDDP by forming complexes through acid-base type interactions [4]. The protocol for studying the effect of PIBSA on ZDDP is similar to the previous section and consists of rubbing steel coupons in a C-P wear rig for various lengths of time in a blend containing 1.5 and 7 weight percent of ZDDP and PIBSA concentrates respectively.

SEM images of films prepared from 5 and 40 min of rubbing are presented in Figure 4.7. The contrast mechanism is similar to the previous SEM images (e.g. Figure 4.3) where regions of the substrate (bright contrast) are clearly distinguishable from the film (dark contrast). Notice also that the field of view in these images is much larger than the previous SEM images that were presented. This is because the film coverage varies significantly from spot to spot and a smaller field of view would not be representative of the morphology. Observed

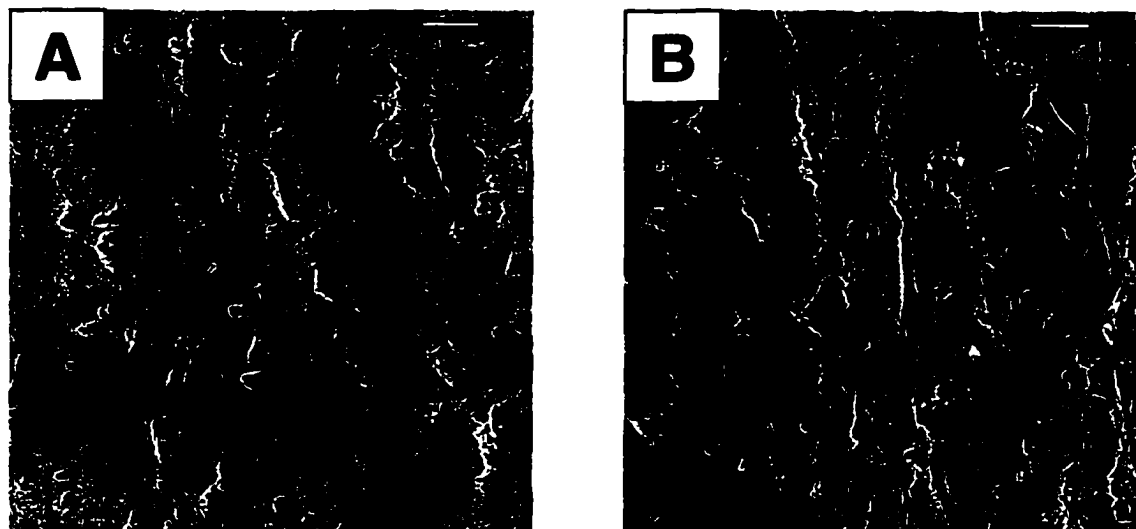


Figure 4.7. SEM images of films prepared from 5 min (panel A) and 40 min (panel B) of rubbing in a lubrication blend consisting of 1.5 wt.% ZDDP + 7.0 wt.% PIBSA dispersant. Scale bar = 10 μm .

throughout the images are numerous pits that become larger from the 5 min to 40 min interval. EDX analysis from the film region in the 5 min sample is presented in Figure 4.8 where the P, S, and Zn peaks confirm the elemental composition of the films. In contrast to films prepared in the presence of Ca sulphonate, the EDX spectrum of films prepared in the presence of PIBSA are similar to the spectra of films prepared from neat ZDDP solutions (Figure 3.4).

The effect of PIBSA on the morphology of the films at different time intervals is illustrated by the SFM images in Figure 4.9. Panel A is a topographic image of the 5 min film and panels B, C, and D are for films prepared from 40, 60, and 120 min of rubbing. In all cases, dark regions corresponding to exposed steel (from EDX analysis) separate regions of the film with a height difference of about 300 nm. The morphology of the 5 min film is comparable to films prepared from neat ZDDP solutions with the difference that there is a larger aggregation of the pads. The pads are approximately 2 - 5 μm in diameter and preferentially oriented in the sliding direction, which runs from top to bottom on the image. While the 5 min films show similarity, films formed from 40 and 60 min of rubbing (panels B and C) are markedly different from films of neat ZDDP solutions (Figure 3.5). The difference is in the surface coverage and density of the film such that in the presence of the dispersant a complete film is not established even after 60 min of rubbing. Only after 120 min of rubbing (panel D) does the film provide complete coverage. In contrast, films prepared from neat ZDDP blends as in Chapter III and those that were prepared in the presence of Ca sulphonate provide total coverage after 40 min of rubbing.

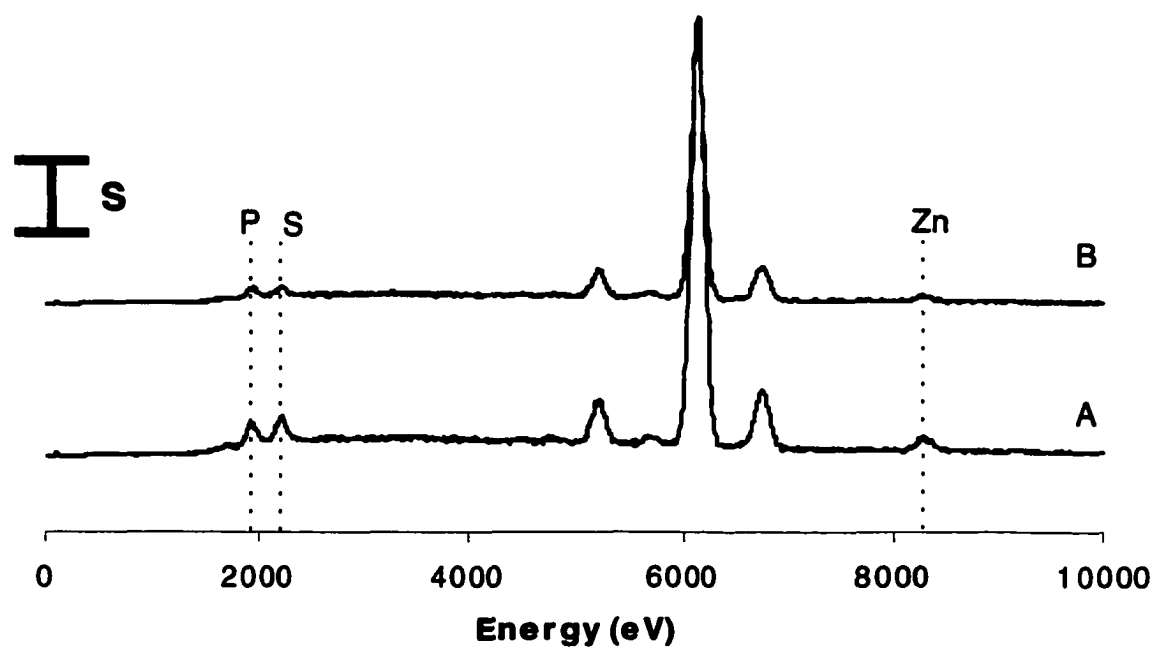


Figure 4.8. EDX spectra of film prepared from a blend consisting of 1.5 wt.% ZDDP + 7 wt.% PIBSA dispersant rubbed for 5 min (spectrum A) and 40 min (spectrum B). S = 1000 counts.

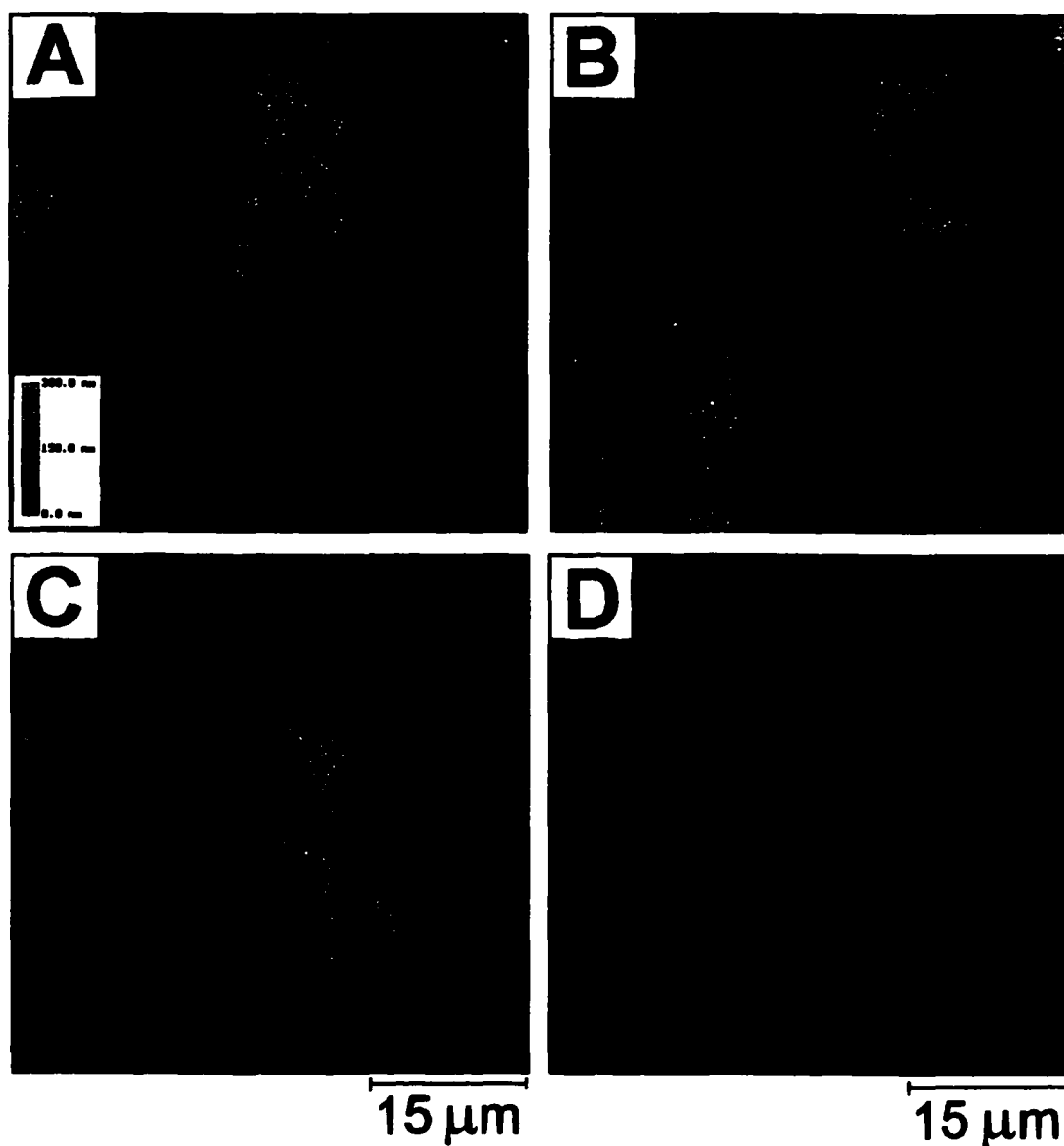


Figure 4.9. Topographic 50 x 50 μm SFM images (z-scale = 300 nm) of films prepared in a blend consisting of 1.5 wt.% ZDDP + 7 wt.% PIBSA dispersant rubbed for: (A) 5 min. (B) 40 min. (C) 60 min. (D) 120 min. The inset in panel A represents the color scheme for the z-scale on all the images.

The SEM and SFM images in Figures 4.7 and 4.9 are in my belief the first direct evidence that PIBSA antagonizes the antiwear action of ZDDP. The images also confirm the work of Yin et al. who observed a reduction in the X-ray absorption peaks of P and S when the films were prepared in the presence of the dispersant [18]. Their conclusion was that the films must be thinner than films formed from neat ZDDP solutions. However the results indicate that the coverage is diminished in the presence of the dispersant whereas in region where the film has deposited the thickness is comparable to films prepared from neat ZDDP blends.

The general consensus so far with films prepared from neat solution or those in the presence of detergent is that film morphology evolves with rubbing time such that the coverage approaches 100 percent after 40 min of tribological contact. The fact that large gaps and discontinuities exist in the films prepared in the presence of PIBSA is evidence that the dispersant impedes the formation of the antiwear film. Clearly, the results imply that the morphology of ZDDP film is affected when PIBSA is present in the lubrication blend.

The nanomechanical properties of the films are evaluated in the same manner as before and presented in Table 4.1. Analysis of the modulus values of the films formed in the presence and absence of the dispersant indicate similar nanomechanical properties. This is further illustrated in Figure 4.10 where the nanoindentation profiles of ZDDP films prepared in the presence (curve A) and absence (curve B) of PIBSA are plotted to show their resemblance. Although the presence of the dispersant does not change the composition of the antiwear

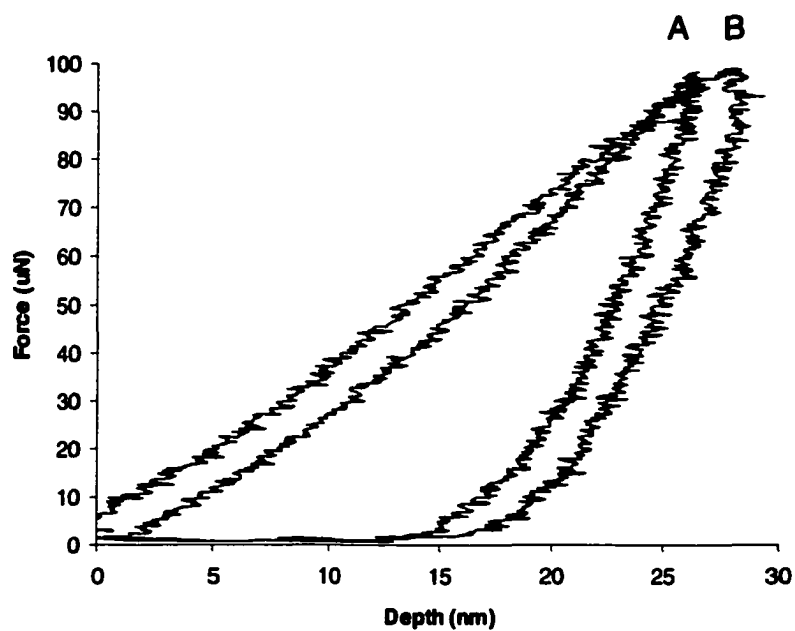


Figure 4.10. Nanoindentation profiles of ZDDP films prepared from 40 min of rubbing in the presence (curve A) and absence (curve B) of PIBSA dispersant.

films, it does result in a higher percentage of short chain polyphosphates [18]. This does not however seem to affect the nanomechanical properties of films.

An interesting result over a small fraction of the 40 min film, as revealed by nanoindentation, is the presence of very stiff regions with $E^* \cong 180$ GPa. These regions were found serendipitously through numerous indentations on this sample. In Figure 4.11 curve B, an example of this behavior is shown alongside the profile of a steel substrate (curve A). Curve C is an average profile of films prepared in the presence of PIBSA with $E^* = 102$ GPa. The proximity between curves A and B highlight the increased stiffness of these regions versus the rest of the film. Although it is difficult to speculate the origins of such a high mechanical strength it is important to note that similar observations were reported in the IFM work of Graham et al. with films prepared from neat ZDDP solutions [21]. They attributed their findings to differences in the chemistry from spot to spot on the samples, which was partially confirmed recently by localized XANES analysis [22].

Conclusion

The results of the analysis of films prepared in the presence of overbased Ca sulphonate detergent and the dispersant PIBSA indicate that there is indeed interaction between the two additives and ZDDP. In the case of the detergent the film coverage at early times is comparable to films prepared from neat ZDDP. The presence of large quantities of Ca in the lubrication blend affects and modifies both the chemistry and nanomechanical properties of the films. The

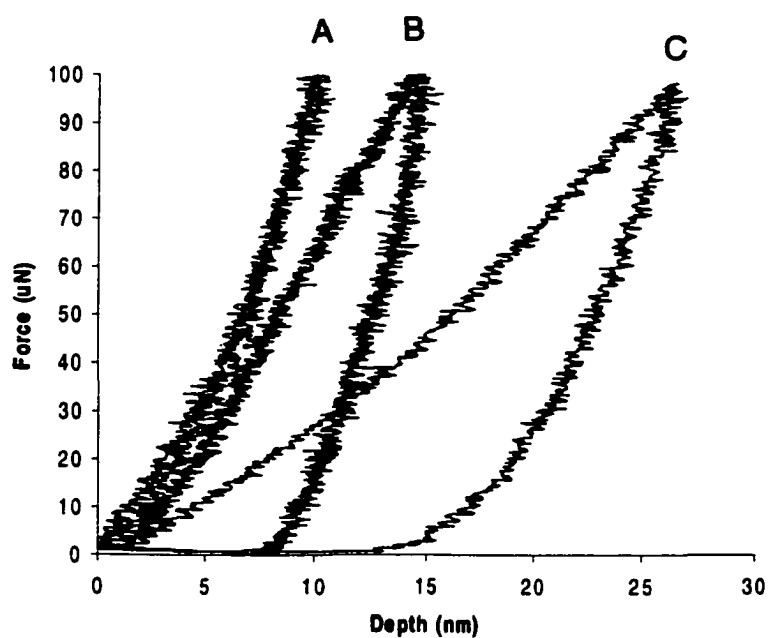


Figure 4.11. Nanoindentation profiles of stainless steel (curve A), a high modulus region (curve B) and low modulus region (curve C) of a film prepared in a blend consisting of 1.5 wt.% ZDDP + 7.0 wt.% PIBSA dispersant rubbed for 40 min.

presence of the dispersant in the lubrication blend impedes the formation of the film but does not alter the elemental composition and mechanical strength of the films.

Reference:

1. A. Caines and R. Laycock, in Automotive Lubricants Reference Book, SAE, 1996, p. 49.
2. F. G. Rounds, ASLE Trans. 21:91 (1978).
3. M. Aktary, M. T. McDermott, and J. Torkelson, Wear 247:172 (2001).
4. K. Inoue and H. Watanabe, ASLE Trans. 26:189 (1981).
5. P. Kapsa, J. M. Martin, C. Blanc, and J. M. Georges, Trans. ASME. 103:486 (1981).
6. F. T. Barcroft and D. Park, Wear 108:213 (1986).
7. N. E. Gallopoulos and C. K. Murphy, ASLE Trans. 14:1 (1991).
8. P. G. Harrison, P. Brown, and J. McManus, Wear 156:345 (1992).
9. M. Kasrai, M. Vasiga, M. S. Fuller, G. M. Bancroft, and K. Fyfe, J. Synchrotron Rad. 6:719 (1999).
10. F. R. Rounds, Lubr. Eng. 45:761 (1989).
11. E. S. Yamaguchi and P. R. Ryason, Tribol. Trans. 2:262 (1998).
12. S. S. V. Ramakumar, A. Madhusudhana Rao, and S. P. Srivastava, Wear 156:101 (1992).
13. J.-M. Martin, C. Grossiord, K. Varlot, B. Vacher, and J. Igarashi, Tribol. Lett. 8:193 (2000).

14. T. V. Liston, *Lubr. Eng.* May:389 (1992).
15. S. Q. A. Rizvi, *Amer. Soc. Metals. Handbook* 18:98 (1992).
16. R. J. Mayer, in International Tribology Conference, Melbourne, 1987, p. 1.
17. P. A. Willermet, D. P. Dailey, R. O. Carter III, P. J. Schmitz, W. Zhu, J. C. Bell, and D. Park, *Tribol. Intern.* 28:163 (1995).
18. Z. Yin, M. Kasrai, G. M. Bancroft, K. Fyfe, M. L. Colaianni, and K. H. Tan, *Wear* 202:192 (1997).
19. M.-C. Dubois-Clockard, J.-P. Durand, B. Delfort, P. Gateau, L. Barre, I. Blanchard, Y. Chevalier, and R. Gallo, *Langmuir* 17:5901 (2001).
20. W. C. Oliver and G. M. Pharr, *J. Mater. Res.* 7:1564 (1992).
21. J. F. Graham, C. McCague, and P. R. Norton, *Trib. Lett.* 6:149 (1999).
22. G. W. Canning, M. L. Suominen Fuller, G. M. Bancroft, M. Kasrai, J. N. Cutler, G. De Stasio, and B. Gilbert, *Trib. Lett.* 6:159 (1999).

Chapter V

Morphology and Nanomechanical Properties of Automotive Engine Components*

Introduction

Although engine wear is an inevitable process, the degree of wearing can be minimized with the correct lubrication blend. For many years the primary anti-wear additive in commercial automotive engine oil formulations has been zinc dialkyldithiophosphate (ZDDP). ZDDP reduces wear by forming sacrificial boundary films at the interface of sliding steel contacts [1]. These boundary films, referred to as tribofilms, are composed of long and short chain polyphosphate glasses and exhibit a lower indentation and shear modulus than the underlying steel substrate [2-5].

In laboratory studies, tribofilms are prepared in reciprocating wear testers on steel coupons and are believed to resemble films that form on real engine components. A drawback to these studies is that bench top wear testers (such as the Cameron – Plint) are not able to accurately generate the interfacial geometry and pressure that engine components will encounter. Therefore caution must be exercised when making any deductions with regards to engine wear from bench top experiments. A second drawback is that these experiments do not account for issues such as oxidation and aging of the lubricant as it undergoes numerous heating and cooling cycles in the crankcase of an engine.

* A form of this Chapter has been published as: M. Aktary, M.T. McDermott, and G.A. MacAlpine, Surf. Eng. In Press.

The majority of published results on ZDDP describe tribofilm samples that were prepared from freshly formulated blends. Finally, while bench top tests run for only a few hours, engine components are in operation for several hundred thousand kilometers that may span over several years. Hence a one or two hour wear experiment may not be sufficient to provide insight about the tribology of a component throughout its operational lifetime.

In this chapter I will attempt to address the above concerns by studying components that have been removed directly from automotive engines. These studies are the first of their kind and will demonstrate the utility of scanning force microscopy (SFM) and nanoindentation to the study of non-ideal industrial samples. They will also serve as a means to assess the validity of bench top wear experiments in providing insight about the antiwear action of ZDDP in an engine.

The analysis will focus on two components that were removed from a heavy-duty diesel truck engine. The components, which are referred to as rocker arm bridges, are part of the valve train assembly in automotive combustion engines.. The intake and exhaust rocker arm bridges control the reciprocating motion of the intake and exhaust valves at the appropriate times in the combustion cycle. The motion of the rocker arm bridge is coupled to the cam and forms a sliding contact that causes the surface of the bridge to wear. The contact zone between the cam and the rocker arm is lubricated by the crankcase oil in order to control wear and thus to ensure proper operation of the valves. Since the crankcase oil contains ZDDP, an anti-wear film is expected to be

present on the surface of the rocker arm bridges. Figure 5.1 is a conceptual illustration of a typical valve train geometry showing the relative position of the rocker arm in relation to the cam. My investigations will focus on regions of the rocker arm bridge that were in contact with the cam.

Experimental Methods

Reagents and materials. MCT 10 base oils, and the commercial ZDDP concentrate, ECA 6654 (15% iso-octyl and 85% iso-butyl dithiophosphate), along with 52100 stainless steel coupons were obtained from Imperial Oil of Canada, Samia Division. Hysitron Inc. (Minneapolis, MN) supplied the cube corner tip used in the nanoindentation experiments.

Sample preparation. The rocker arm bridges come from the valve train of a Cummins N-14 heavy duty diesel engine that has been in service for about 330,000 kilometers. In this particular case, the engine was lubricated with a commercially available API CH-4 quality engine oil that was regularly changed every 35,000 kilometers. The elemental composition of the API CH-4 engine oil is given in Table 5.1 based on the specification of the manufacturer. The rocker arm bridges were cut by the Chemistry glass shop here in the University of Alberta using a diamond cutting wheel so as to isolate the complete wear zone from the rest of the component. This was necessary because of size limitations in the sample holder on the SFM and the nanoindenter.

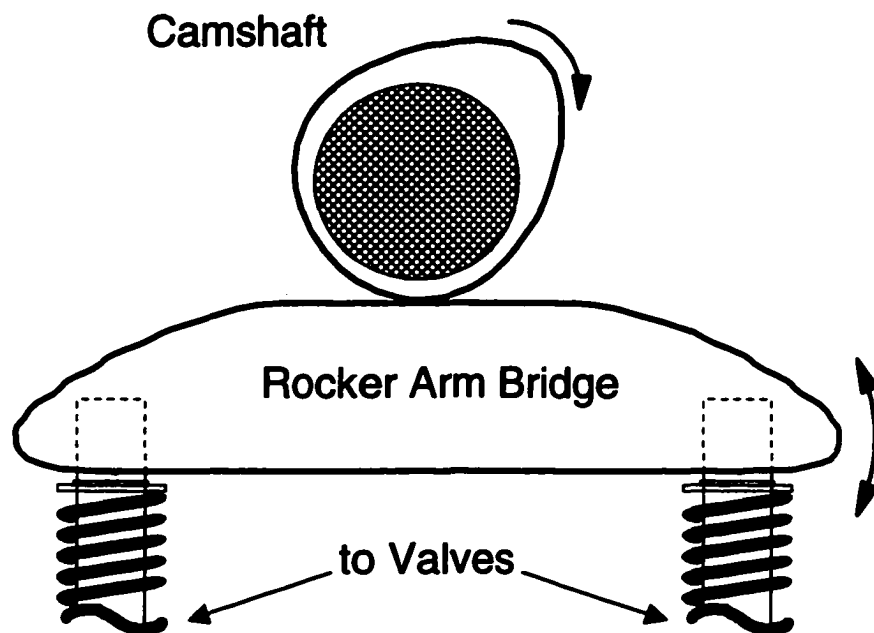


Figure 5.1. Cross sectional schematic illustrating the components that collectively comprise the valve train of a two or four stroke combustion engine. The analyses presented here will be concerned with regions of the rocker arm bridge that are in contact with the opposing cam.

(Reproduced with permission from Dr. Mark T. McDermott)

Table 5.1. Elemental composition of the API CH - 4 engine oils used to Lubricate the rocker arm bridges. The designation API CH – 4 implies that the oil meets the American Petroleum Institute (API) requirements for 1998 low emission diesel engine oils.

Element	Concentration (PPM)
Ca	2830
Mg	Trace
P	1250
S	*
Si	< 20
Zn	1410

* The S content was not cited by the manufacturer.

SFM imaging. Topographic SFM images were collected using a NanoScope IIIa or a Dimensions 3000 (Digital Instruments, Santa Barbara, CA) scanning force microscope (SFM) using triangular Si₃N₄ cantilevers (spring constant, $k \sim 0.06$ N/m). Images presented here were captured continuously at a scan rate of 2 - 8 Hz at a normal force of no more than 10 nN. The images were software flattened both in the X and Y and are otherwise untreated.

Nanoindentation. Nanoindentation experiments were performed with a TriboScope® (Hysitron Inc) nanomechanical testing instrument interfaced to a Digital Instrument (Santa Barbara, CA) Dimensions 3000 SFM controller allowing in-situ imaging of the sample before and after an indent. Indents were performed with a cube corner diamond tip (Hysitron Inc. Minneapolis, MN) at a force of ~ 100 μ N and a loading rate of 10 μ N / sec. The indentation modulus was calculated based on the method of Oliver et al. [6]. Many different regions of each sample were analyzed.

SEM and EDX analyses. Secondary electron images and energy dispersive X-ray spectra were collected with a JEOL model 6301FXV scanning electron microscope at accelerating voltages between 5 - 20 kV and a working distance of 4-5 mm.

Results and Discussions

Photographs of the rocker arm bridges are shown in Figure 5.2 where panel A is the intake bridge (I – bridge) and panel B is the exhaust bridge (E – bridge). A rectangular wear scar forming the contact zone with the cam is

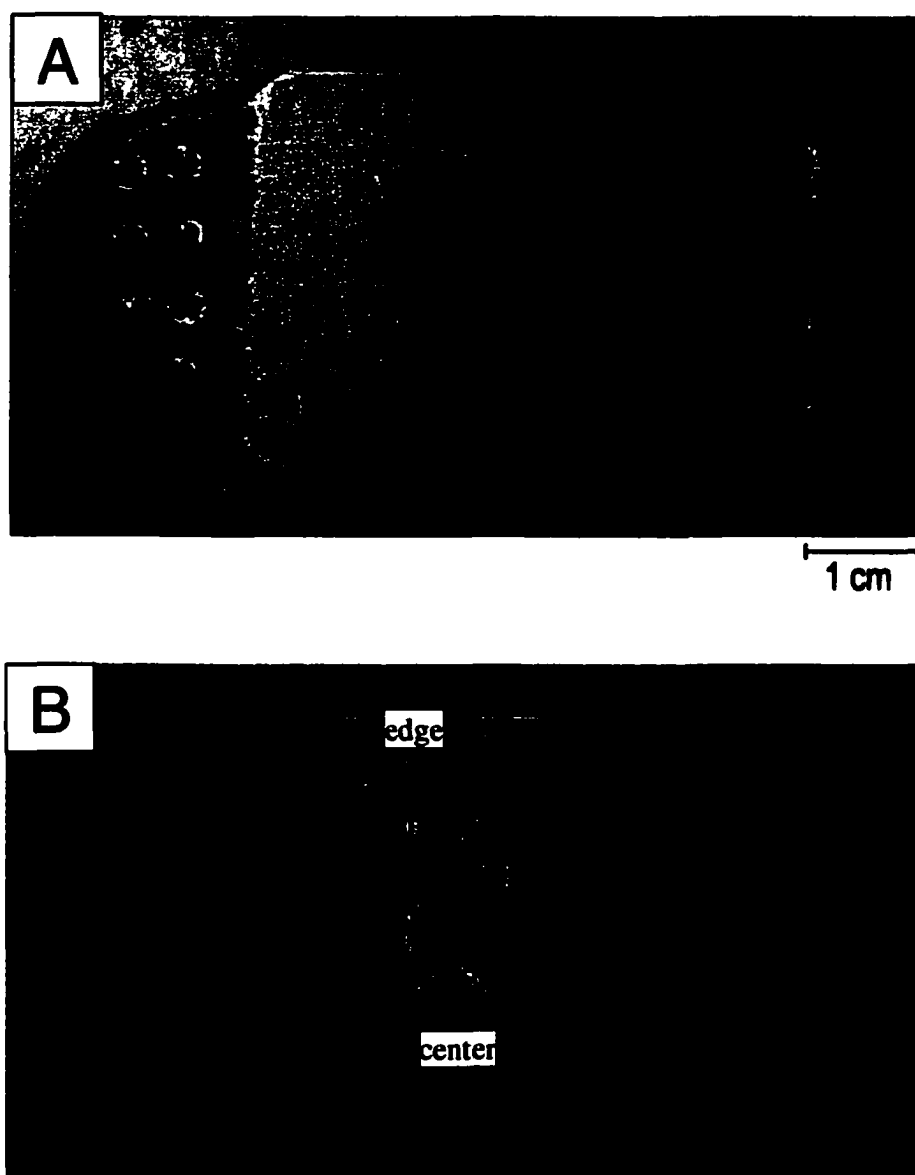


Figure 5.2. Photographs of the crosshead bridges removed from a heavy duty diesel engine. Panel A is removed from the intake manifold (I - bridge) and panel B is removed from the exhaust manifold (E-bridge).

situated at the center of the images and is clearly visible on both components. The wear scar on the E – bridge will be further differentiated with respect to lateral location as center and edge, where the edge represents regions at the periphery of the contact zone. The reason for this classification will become evident later.

I first present result from the analysis of the wear scar on the I – bridge component. Figure 5.3A and 5.3B are 100 and 30 μm topographic SFM images (z – scale = 200 nm) of the center region of the wear scar. The surface consists of smooth terraces along with a series of pits that measure 200 – 300 nm in depth. The pits exhibit random shapes and do not appear to be oriented in any particular direction. Higher resolution images ($1 \times 1 \mu\text{m}$) of the two regions are shown in Figure 5.4 where panel A depicts the morphology at the bottom of the pit and panel B represents the terraces. The terraces exhibit a relatively smooth and featureless topography, in comparison to the bottom of the pits. The root mean square roughness (RMS) is 38.4 nm for the pit (Figure 5.4A) and 1.8 nm for the terrace (Figure 5.4B) respectively. From previous studies of tribofilms prepared in the C – P wear tester, the images in Figures 5.3 and 5.4 initially led me to assign the terrace region as a tribofilm and the pits as the underlying steel substrate. It was assumed that the pressure from the opposing cam had removed parts of the tribofilm leaving regions of the substrate exposed.

This initial assignment was however invalidated after SEM and EDX analysis failed to show any traces of P, S, or Zn on the terraces (see below). Instead contrary to expectation, relatively large quantities of P and S were

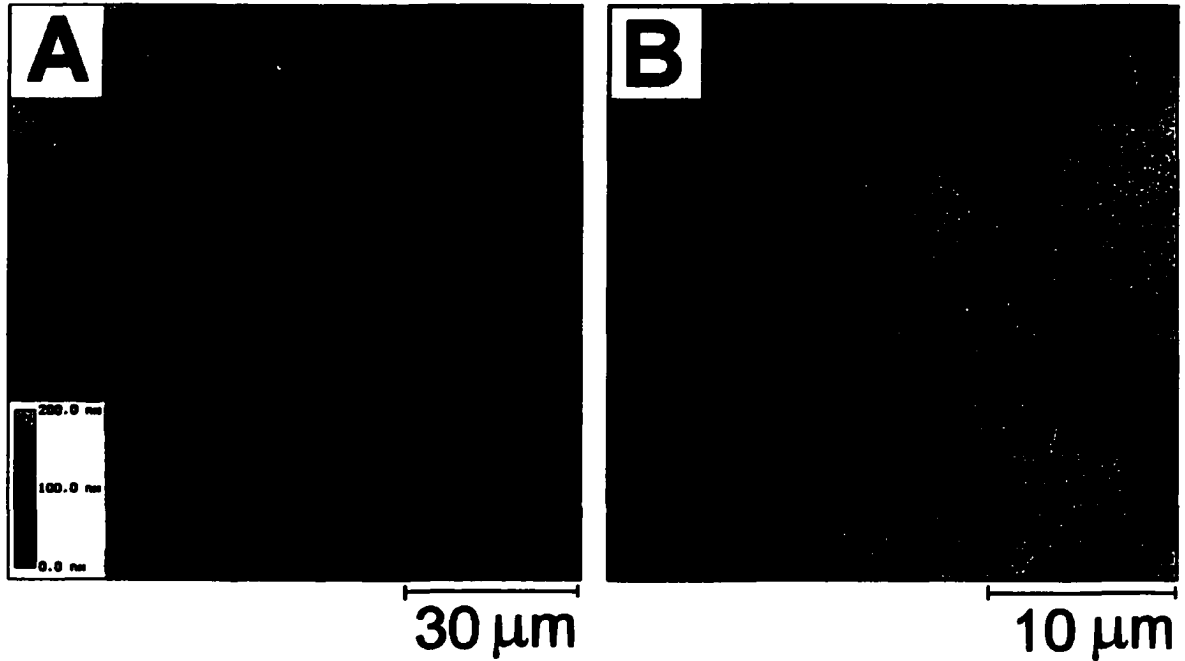


Figure 5.3. Topographic SFM images (z- scale = 200 nm) of the center region of the intake crosshead bridge. Panel A and B are at 100 and 30 μm fields of view respectively. The inset in panel A represents the color scheme for the z-scale on both images.

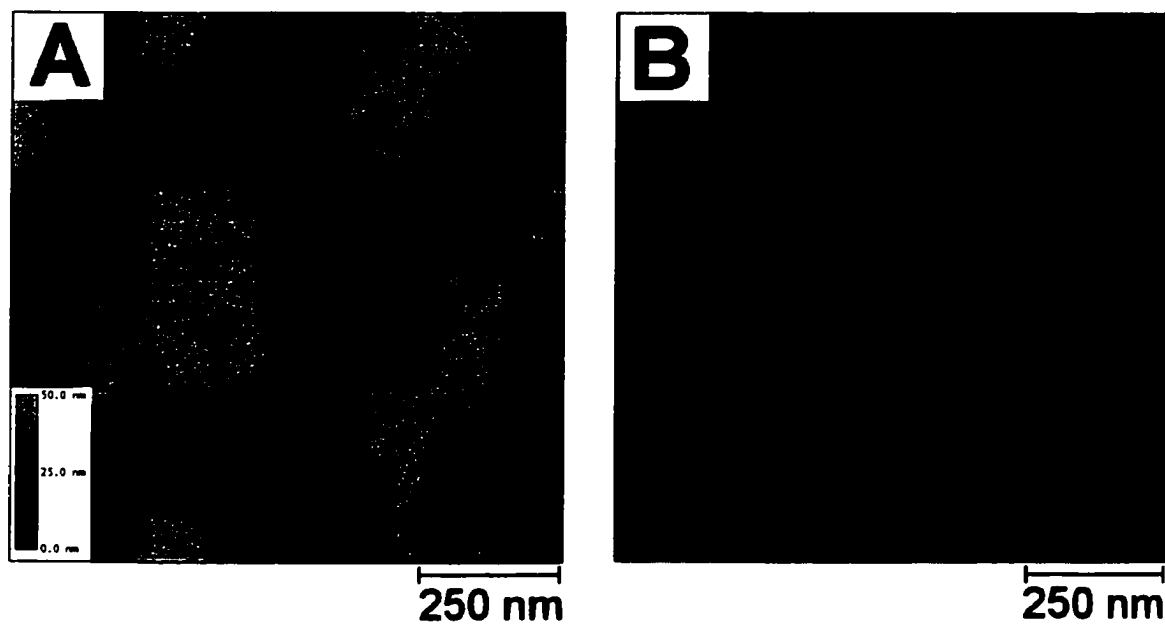


Figure 5.4. Topographic $1 \times 1 \mu\text{m}$ SFM images (z- scale = 50 nm) of the center region of the intake crosshead bridge. Panel A represents the topography of the bottom of the pits and panel B represents the terraces. The inset in panel A represents the color scheme for the z-scale on both images.

present in the material bound within the pits. Figure 5.5A and B are secondary electron SEM images of the wear zone in the I – bridge. The terraces appear as light contrast whereas the pits are dark regions scattered throughout the image. This contrast is due to difference in the topography and composition of the terraces in relation to the pits.

EDX spectra obtained from regions representing the terraces and the pits are presented in Figure 5.6. The intense peaks located at the position of the Fe K lines and as well as the Cr peaks on the lower spectrum confirm that the terraces are composed of steel. However, no evidence of ZDDP decomposition products is observed in the terrace spectrum. The top spectrum however reveals that a wide range of elements constitute the material within the pits. In addition to Fe and Cr, large amounts of Ca, K, Cl, S, P, Si, and Al are also present. The peaks were assigned using an archived database of the atomic energy levels of the elements. The experimental and literature values for the K – shell energy levels of the above elements are presented in Table 5.2 and show good agreement. The presence of Ca, S, P, and Si arise from additives such as overbased detergents, ZDDP, and silicone antifoam agents present in the engine oil lubricant (see Table 5.1). However the origins of Al, Cl, and K cannot be attributed to the lubricant and likely arise from impurities ingested by the air intake (dirt, road salt, dust, etc.). Aluminum may also originate from wearing of components that are manufactured from aluminum metal.

The EDX results provide direct evidence for the presence of lubricant derived materials along the bottom of the pits. It is believed that these materials

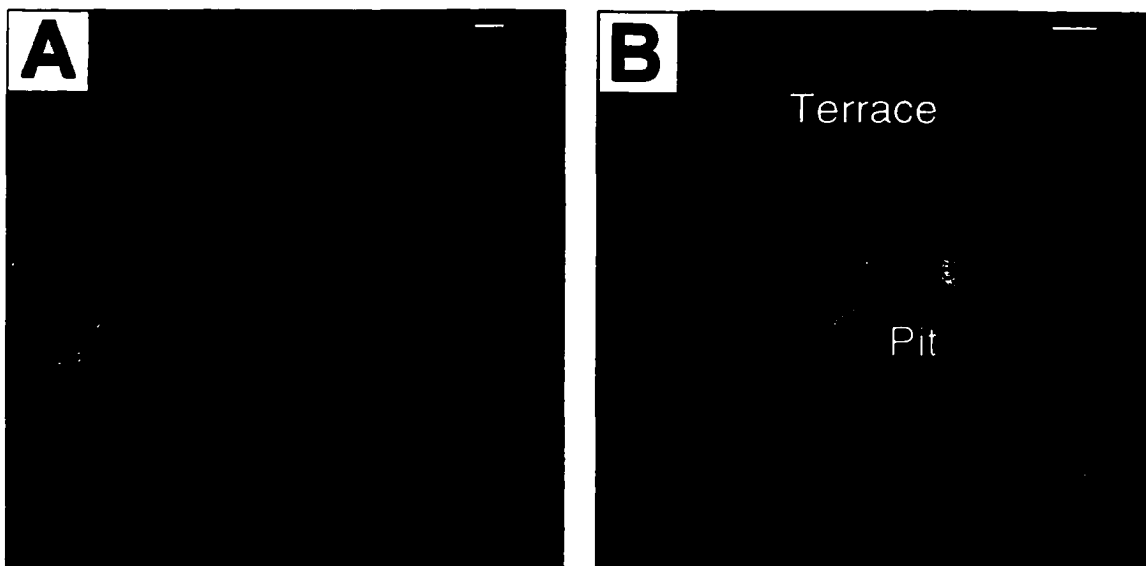


Figure 5.5. SEM images of the center region of the intake crosshead bridge. The terrace and pit as marked in panel B correspond to the EDX spectra in Figure 5.6.

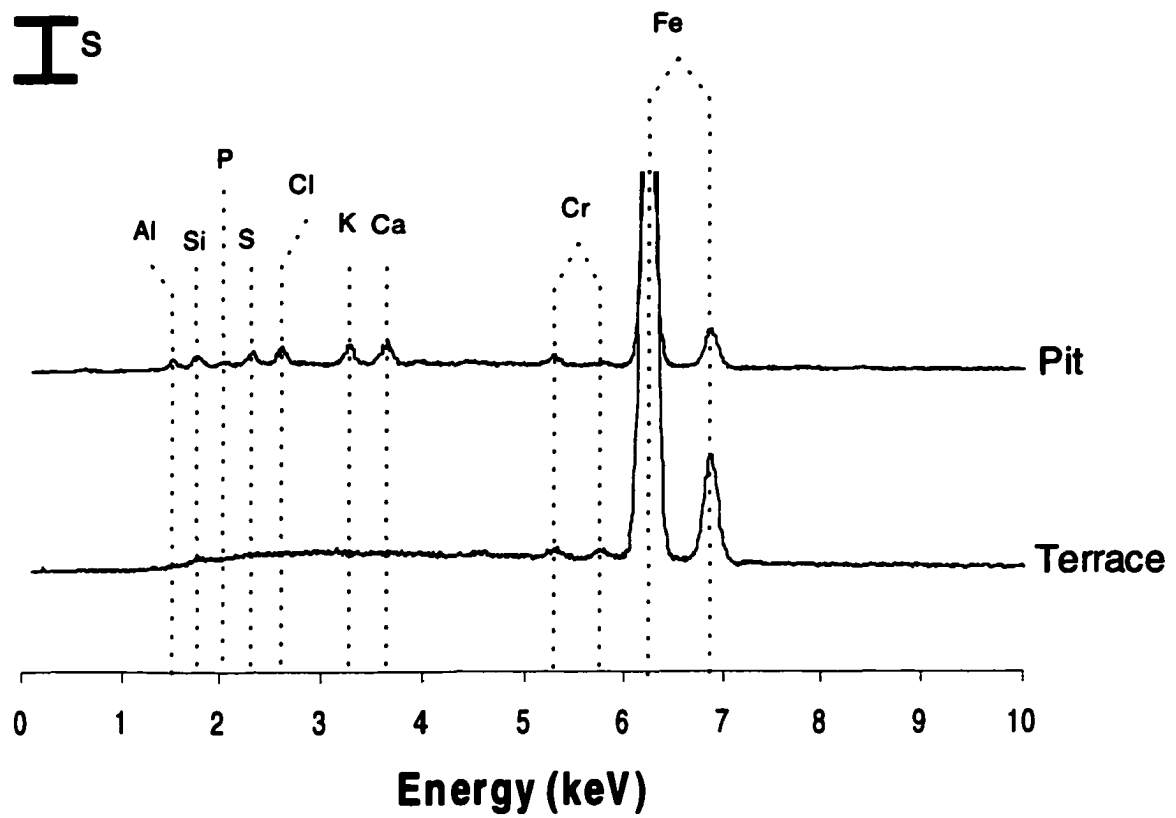


Figure 5.6. EDX spectra of the intake crosshead obtained from the terraces and the pits as marked in Figure 4B. ($S = 500$ counts).

Table 5.2. Comparison of the experimental X-ray energy levels with literature values taken from the CRC Handbook of Chemistry and Physics 64th Edition (1983-1984).

Element	Experimental (keV)	Literature (keV)
Al	1.53	1.49
Si	1.77	1.74
P	2.06	2.01
S	2.33	2.31
Cl	2.61	2.62
K	3.29	3.31
Ca	3.61	3.69
Cr	5.30	5.40
	5.80	5.95
Fe	6.30	6.39
	6.88	7.06

are adsorbed decomposition products of the base oil and other additives present in the blend used to lubricate the engine. The terraces however are exposed steel and do not contain an antiwear film as was first assumed.

Nanoindentation analysis was next employed to investigate the nanomechanical properties of the different regions on the wear scar. The wear zone was first imaged with the nanoindenter to differentiate the pits from the terraces before an indent was performed. The results are presented in Figure 5.7, where curves A and B represent the regions corresponding to the terraces and pits respectively. For comparison, nanoindentation curves for an unmodified steel substrate (curve C) and a thermooxidative ZDDP film (curve D) prepared by exposing a steel coupon to a heated solution of ZDDP in base oil for 3 h. are also plotted in Figure 5.7. The nanoindentation profile of the terrace (curve A) is very similar to that of the standard steel coupon (curve C). The calculated elastic modulus of the terrace region is approximately 200 GPa, equal to that of the reference steel coupon. These observations agree with EDX results in Figure 5.6 and imply that little ZDDP film exists on the terraces.

The nanoindentation profile of the material within the pits is markedly different from the terraces (compare curves A and B). This material is much softer and exhibits a high degree of plastic flow. This is evident by the large indentation depth (~75 nm) and by the width of the hysteresis loop in curve B. The indentation modulus calculated from curve B (25 GPa) is less than that of a thermooxidative ZDDP film (curve D), which is 35 GPa. It must be pointed out however that the nanoindentation profile depicted by curve B was not the same

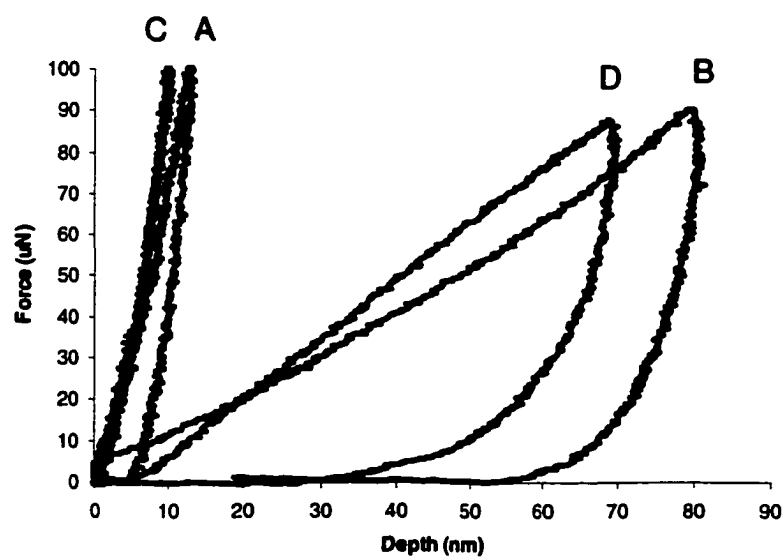


Figure 5.7. Nanoindentation profiles of a steel coupon (curve C), the terrace region of the intake crosshead bridge (curve A), a 3 h thermooxidative ZDDP film (curve B), and the pit region of the intake crosshead bridge (curve D).

throughout all of the pits and occasionally a stiffer response was observed. Nonetheless this discrepancy may be a result of topographic discontinuities along the bottom of the pits and not reflect the composition of the pits.

The model that emerges from the combined analyses on this component is as follows. The terraces are exposed steel that may be sheltered by a tenuous film. An antiwear film that may have protected these regions was not sufficient to overcome the stresses from the opposing surface causing metal contact. The presence of wear pits and depressions detected by both SFM and SEM support that wear damage must have occurred. The pits do not originate from the inherent surface morphology of the rocker arm bridge as will be shown later. EDX and nanoindentation both provide conclusive evidence that the bottom of the pits is covered with other materials besides steel. It is proposed that these materials are products of the thermooxidative decomposition of the base oil and other additives used to formulate the lubrication blend. These materials become immobilized within the pits and are not in contact with the opposing surface as the terraces shelter them.

While the wear scar on the I – bridge featured similar morphology throughout, the wear zone on the E – bridge exhibits differences in morphology and composition laterally across the wear scar. The E – bridge is macroscopically distinguishable from the I – bridge by the presence of crescent shaped wear scars above and below the central wear zone (refer to Figure 5.2B). The extra wear patterns result from the loading of an air brake mechanism that utilizes the pressure from the exhaust gases to slow the vehicle. To help the

discussion the central wear zone is divided into center and edge regions as marked in Figure 5.2B. Analyses of the crescent shaped wear scars and the center of the main wear zone revealed very similar characteristics to those of the I – bridge. The morphology along these regions consisted of an array of terraces and pits with the pits consisting of a soft material as before and the terraces being exposed steel. These results will not be shown for the sake of brevity and the reader may refer to Figures 5.3 – 5.7 for a complete description of these regions.

The remainder of this discussion will focus on results that have been obtained on the edge region of the E – bridge as marked in Figure 5.2B. Figure 5.8A and B are SEM images with a field of view of 145 and 90 μm respectively of this region. Film material highlighted by dark contrast is visible running diagonally from top to bottom on the image similar to ZDDP tribofilms prepared on steel coupons. The lighter regions are topographically smooth at this length scale and are more prevalent on the images. EDX spectra collected from the light regions produce only Fe and Cr peaks and thus is characteristic of steel alloys. An EDX spectrum obtained from the dark regions is presented in Figure 5.9. In addition to the steel background, elements such as Ca, Si, and S are also present. Thus it is envisaged that the film has originated from ZDDP and other decomposition products of the lubricant.

The topography and nanomechanical properties of the edge region were studied in detail by SFM and nanoindentation. Figure 5.10A and B are 100 and 30 μm topographic SFM images that were obtained by macroscopically

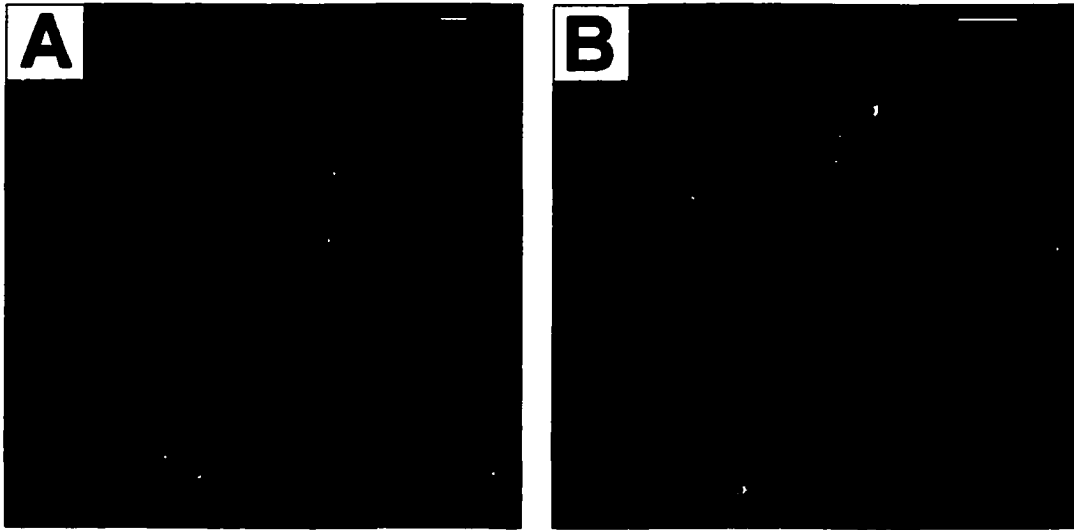


Figure 5.8. SEM images from the edge of the exhaust crosshead bridge. The light regions are the steel alloy used to manufacture the component and

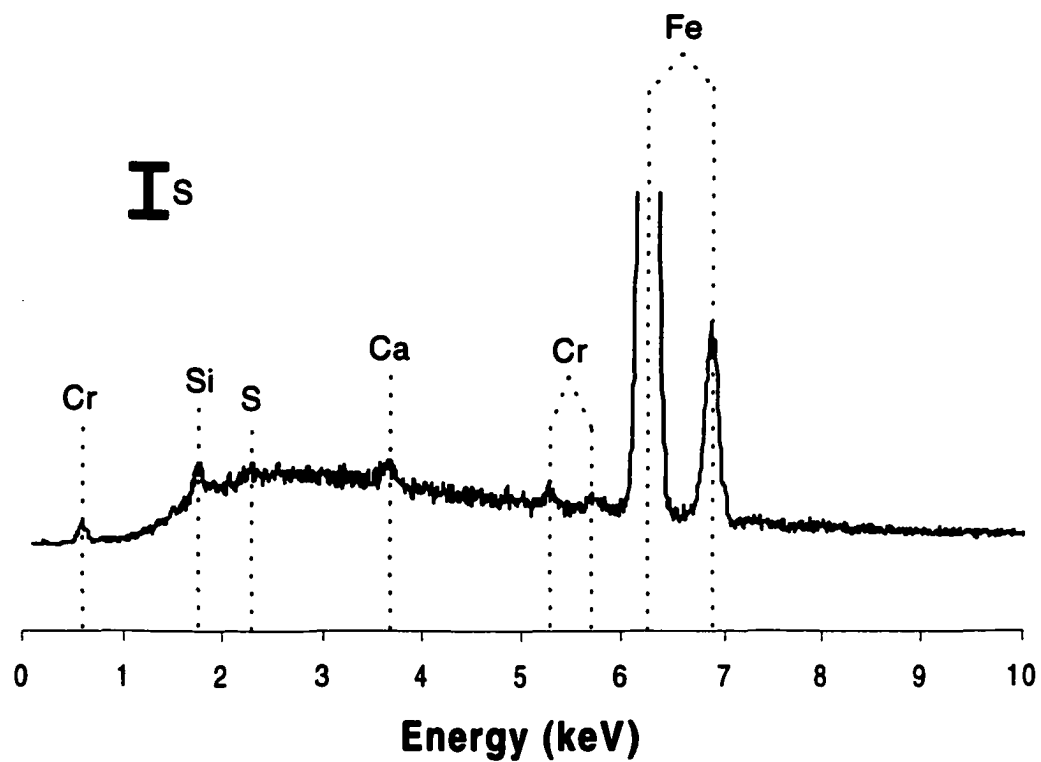


Figure 5.9. EDX spectrum of the film material at edge of the wear scar on the exhaust crosshead bridge. (S = 100 counts).

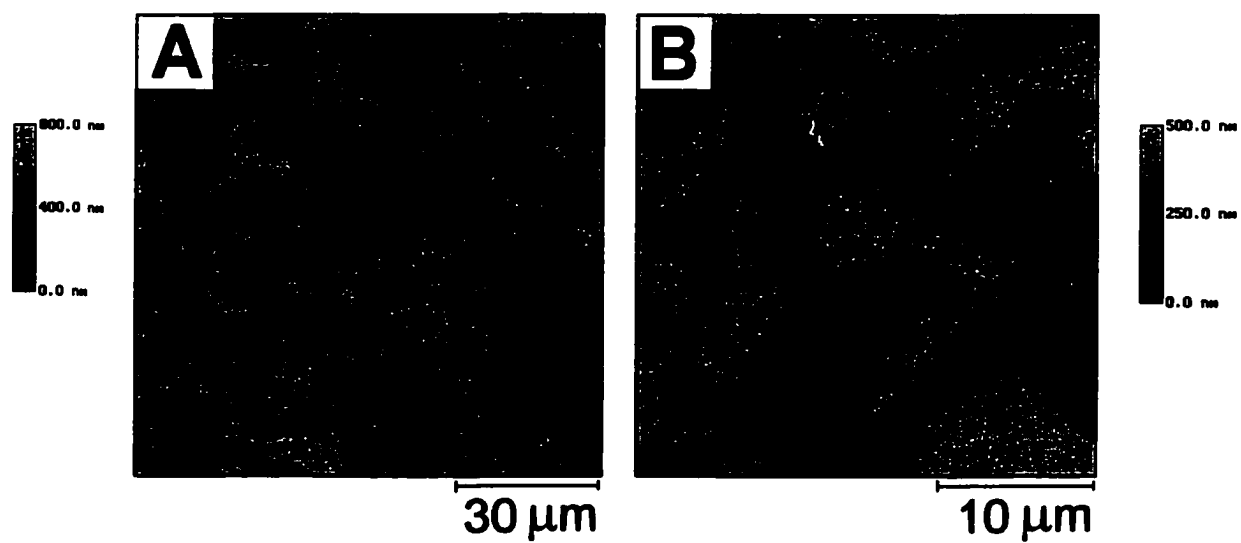


Figure 5.10. Topographic SFM images of the edge region of the exhaust crosshead bridge. Panel A is 100 μm field of view (z-scale = 800 nm). Panel B is 30 μm field of view (z-scale = 500 nm).

positioning the SFM probe just inside the boundary demarcating the contact and non – contact regions. Regions of high topography define the structure of the film as an irregular array of islands or pads that are from 500 – 800 nm in height. The film coverage is similar to laboratory tribofilms formed from long rubbing times in wear testers (see Chapter III). The lateral dimensions of the pads are approximately 5 – 10 μm and are morphologically similar to tribofilms prepared in the C – P wear tester. This can be seen more clearly at the 30 μm field of view (Figure 5.10B). The pads are not however elongated in any specific direction as was observed with the laboratory tribofilms. Thus, intriguingly, the edge region on the E – bridge is partially covered by a surface film that exhibits morphological similarities to ZDDP antiwear films prepared in the laboratory.

Our next experiments were directed towards elucidating the nanomechanical properties of the film on the E – bridge. The diamond tip was first positioned at the periphery of the contact zone to microscopically locate the pads. In this manner there was no ambiguity as to where the indent was performed. Nanoindentation profiles were obtained on several pads and one such profile is presented as curve A in Figure 5.11. Curve B is the nanoindentation profile of a 10 min ZDDP tribofilm from Chapter III. The similarity between curves A and B indicates very similar nanomechanical properties between the film on the E – bridge and ZDDP tribofilms. The indentation modulus as calculated from curve A is approximately 90 GPa. However subsequent experiments showed large inconsistencies in the profiles from spot to spot on the sample.

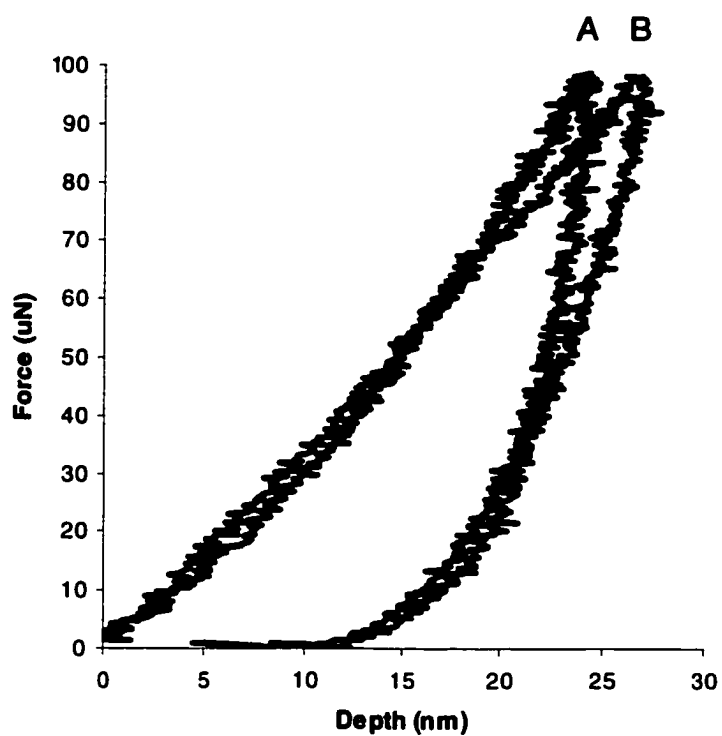


Figure 5.11. Nanoindentation profiles of the film region from the exhaust crosshead bridge (curve A), and a 10 min tribofilm prepared in a Cameron - Plint wear tester (curve B).

This point is illustrated in Figure 5.12 where nanoindentation profiles from two other pads are plotted. Curve A of Figure 5.12 indicates that the film is composed of at least two layers as evidenced by the large change in the slope at approximately 15 nm, where a compliant surface layer covers a stiffer bulk material. Notably, the duplex nature of antiwear films has been observed previously by interfacial force microscopy [5], and in a study that utilized the surface force apparatus (SFA) [7]. The film also has a high propensity to resist plastic flow. Close analysis of the unloading portion of Curve A in Figure 5.12 shows a distinct reduction in the slope at 15 nm, after which the curve returns to zero depth while still being in the repulsive force regime (i.e. $F > 0$). In contrast all of the tribofilm that have been analyzed previously deform plastically at a load of 100 μN . Curve B of Figure 5.12 resembles the nanoindentation profile of thermooxidative ZDDP films similar to curve C in Figure 5.7. The range of responses in Figures 5.11 and 5.12 indicate a large degree of spatial heterogeneity in the nanomechanical properties of film over the E – bridge. It is believed that some regions are simply adsorbed thermal decomposition products, while other regions exhibit properties that resemble antiwear films derived from ZDDP.

The combined results from the analyses of the wear zone on the E – bridge discloses a high degree of topographic diversity with respect to lateral position. The center region consists of pits and cavities and is morphologically similar to the I – bridge. The pits contain a soft material that is likely the thermooxidative decomposition products of ZDDP and other additives of the

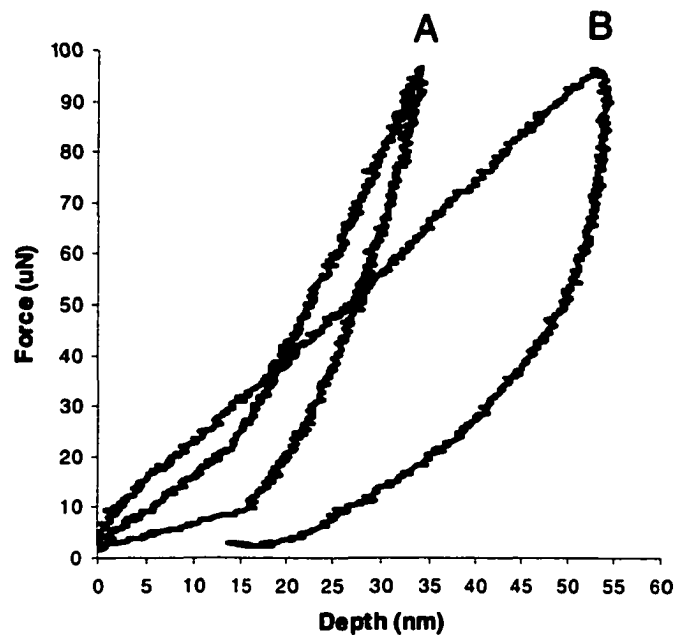


Figure 5.12. Nanoindentation profiles from different spots along the edge of exhaust crosshead bridge. The designations A and B are arbitrary.

lubricant. Interestingly, at a location near the edge of the scar, a film is detected. The film contains traces of S, Ca, and Si that originate from the lubricant. Contrary to expectation, P and Zn were not detected even though ZDDP was present in the lubricant. The majority of the film may be resulting in the dark contrast in the SEM images against the steel substrate. The EDX analyzer was not equipped to detect lighter elements such C and O, but their presence cannot be disregarded. The question as to whether the film is truly a tribofilm derived from ZDDP cannot be substantiated by these results. Certainly the film structure is similar in terms of the dimension of the pads to tribofilms prepared in the wear tester. The nanomechanical properties also show similarities to ZDDP tribofilm on some regions. EDX analysis however failed to detect P and Zn on the films, although other elements originating from the lubrication blend were detected. The majority of the film is likely composed of the decomposition products of the lubricant mixed with carbon impurities such as soot that are known to build on engine surfaces.

The fact that we have observed a surface film sheltering the substrate at the periphery of the wear scar on the E – bridge component is evidence that the lubrication blend is providing some level of wear protection. This is further supported by the smooth and featureless morphology of the exposed steel at the edge of the wear scar (Figure 5.8). By contrast the center of the wear scar where the film is absent is perforated with pits and cavities. The pits are a result of wear damage and their absence at the edge implies antiwear action by the film.

Although preliminary, the difference between the center and edge regions is likely a result of very different contact regimes along the bridge surface. It is envisaged that the center region encounters large stresses from the opposing cam, which essentially displaces the antiwear film. On the other hand, the periphery of contact is subjected to lower stresses where the antiwear film remains. The other possibility is of course that the lubricant was not replaced frequently enough to provide sufficient wear protection. Practical experience validates the latter statement since negligence in changing and maintaining engine oil results in severe engine damage.

The fact that a film was detected on the exhaust bridge and not on the intake bridge may also be attributed to differences in contact stress between the components. Interesting however, the E – bridge encounters a larger load than the I – bridge [8]. This extra loading comes from an air brake mechanism that uses the pressure from the exhaust gases to slow the vehicle. However a film is detected at the periphery of the contact zone on the E – bridge as opposed to the I – bridge even though the former is placed under more load.

Conclusions

These studies have shown that non-conventional samples such as used automotive components are amenable to analysis by scanning probe techniques to generate meaningful analytical data. Wear scars on a rocker arm bridge component removed from the exhaust manifold of a diesel engine were shown to be morphologically heterogeneous. The center of the scar is worn steel,

whereas a film was detected at the periphery of the scar. Analysis of a second sample removed from the intake manifold of a similar engine did not show any evidence for the presence of a film on any region of the wear scar. The presence or absence of the film may be due to differences in contact pressure between the center and edge of the wear scar and between the E –bridge and I – bridge components themselves. Further studies will be required to substantiate these results whereby components will be removed from the same vehicle that has been subjected to the same maintenance schedule and driving conditions.

The results also show that there is a considerable amount of damage at the center of the wear scar where high contact pressures are expected. The wear damage is evident by the presence of pits and cavities that dominate the topography at these locations. The pits contain materials that originate from the decomposition products of the lubricant formulation and impurities from the environment.

References:

1. A. G. Papay, *Lubrication Sci.* 10:209 (1998).
2. G. M. Bancroft, M. Kasrai, M. Fuller, Z. Yin, K. Fyfe, and K. H. Tan, *Tribol. Lett.* 3:47 (1997).
3. Z. Yin, M. Kasrai, G. M. Bancroft, K. F. Laycock, and K. H. Tan, *Tribol. Int.* 26:383 (1993).
4. J. F. Graham, C. McCague, and P. R. Norton, *Tribol. Lett.* 6:149 (1999).

5. O. L. Warren, J. F. Graham, P. R. Norton, J.E. Houston, and T. A. Michalske, *Tribol. Lett.* 4:189 (1998).
6. W. C. Oliver and G. M. Pharr, *J. Mater. Res.* 7:1564 (1992).
7. S. Bec, A. Tonck, J.-M. George, R. C. Coy, J. C. Bell, and G. W. Roper, *Proc. Roy. Soc. Lond.* A455:4181 (1999).
8. Private communications (Imperial Oil Limited, Samia, Ontario) September 2001.

Chapter VI

Conclusions and Future Work

Overall Conclusions

The science of friction, wear, and lubrication continues to be an exciting area of research that can lead to many valuable technological applications. The study of these phenomena on the macroscopic scale began with the work of Amonton, Coulomb, and Reynolds in the 17th Century [1, 2]. Technologies to investigate these phenomena on the microscopic scale are emerging and have been advanced immensely by the development of scanning probe microscopy (SPM) [3].

The majority of the work presented in this thesis describes the application of SPM technologies to the wear and lubrication of automotive combustion engines. Our research interests focussed on the characterization of films produced by a class of compounds known as zinc dialkyldithiophosphate (ZDDP) that function to prevent the wear of engine components during sliding contact. These agents have been used in engine oil formulations for many years and provide antiwear action by forming sacrificial boundary films at the interface of sliding contacts. Previous spectroscopic investigations had provided insights about the composition of the films. The driving force behind my work was that limited information was known about the morphology and nanomechanical properties of the films. The latter properties are of importance to the mechanism by which the films provide wear protection [4].

My investigations evolved from very fundamental and controlled studies under static conditions to complicated industrial samples that were obtained directly from commercial vehicles. In Chapter II, scanning force microscopy (SFM) and reflectance infrared spectroscopy were utilized to probe the topography and structure of films formed by the thermooxidative decomposition of ZDDP on Au substrates. The topography of thermal films on both a micron and sub-micron scale was shown to evolve with oil heating time. The morphology at the micron length scale is dominated by the formation of islands that originate from the precipitation of ZDDP decomposition products in the oil. An underlying layer surrounds and perhaps embeds these islands. The topography of this underlying layer transforms from a grain structure for 1 and 2 h films to smooth and featureless for 3 to 6 h. films.

In Chapter III, the morphology and nanomechanical properties of ZDDP tribofilms were studied. The tribofilms were prepared in a Cameron – Plint (C – P) wear tester under conditions that emulated the contact regimes of components along the valve train of an automotive engine. SFM and nanoindentation was employed to track the growth of the tribofilms on steel coupons as a function of time spent in the wear tester. Also some preliminary results on the effect of soot impurities and sliding velocity were presented. The main conclusion from these studies was that the morphology of ZDDP derived tribofilms evolve with rubbing time, such that at lower times distinct segregated pads form, which at longer times transform to a more even and morphologically smooth coating over the steel substrate. Although rubbing time influences the

morphology, it was shown through nanoindentation studies that the nanomechanical properties of the film are relatively constant with time. The films are characteristic of soft polymeric materials and exhibit higher plasticity than the steel substrate. This is consistent with the sacrificial nature of the films. It was also found that both the spatial distribution and nanomechanical properties of the films can vary from spot-to-spot on the wear zone. This was attributed to differences in pressures at the interface of contact.

Soot was shown to markedly decrease the amount of film on the surface, presumably by displacing the film through abrasion. Nanoindentation revealed that the films prepared in the presence of soot were mechanically stiffer than normal ZDDP tribofilms. This is a result of the soot particles becoming incorporated in the matrix of the antiwear films. The effect of sliding speed was also investigated. Preliminary studies indicate that sliding velocity influences the morphology of the tribofilms. This may be a result of the lower interfacial temperature at the lower reciprocating frequency. Sliding speed did not however affect the nanomechanical properties of the tribofilms under our experimental conditions.

The studies in Chapters II and III were conducted on tribofilms that had been prepared from neat ZDDP solutions. A typical engine lubricant however contains a plethora of chemical additives solvated in a matrix of base oil. Several studies had previously shown that various detergents and dispersants can interfere with the solution chemistry of ZDDP and the tribological properties of its resulting antiwear films. In Chapter IV it was shown that overbased calcium

sulfonate detergents promote tribofilm formation such that the surface coverage is complete at much lower rubbing times than films prepared from neat ZDDP blends. The presence of Ca in the lubrication blend however modifies both the chemistry and nanomechanical properties of the films. Elemental analysis confirmed the presence of Ca on the tribofilms and corroborated previous spectroscopic studies. An increase in the stiffness of the films was also observed and was attributed to either the formation of calcium phosphates or the incorporation of colloidal calcium carbonate particles in the matrix of the antiwear films. A dispersant that is commonly used in engine oil formulations was shown to impede the formation of the film but did not alter the elemental composition or the stiffness of the films. Tribofilms formed in the presence of the dispersant exhibit a lower coverage than films prepared from neat ZDDP blends.

One of the main objectives of our investigations was to gain an understanding of the function and behavior of ZDDP in the crankcase of the engine. The results in Chapters II – IV and the majority of published reports about the antiwear action of ZDDP are conducted on samples that are prepared in the laboratory under static oil bath conditions or in wear testers. Insight into the behavior and reactivity of ZDDP in the engine is then inferred from the laboratory tests. A concern that arises is the extent to which such experiments are valid in predicting the behavior of ZDDP in the engine during different driving conditions. The final phase of the studies was an effort to address these concerns by employing SPM analysis to the study of engine components removed directly from operational vehicles. These studies were the first of their

kind and demonstrated the applicability of SPM technologies to the analysis of engine components. SFM analysis of a rocker arm bridge obtained from the valve train of a diesel engine revealed large differences in surface structure and composition with respect to lateral location on the wear scar. The center of the scar is predominantly exposed steel, whereas a film was detected at the periphery of the scar. Analysis of a second component removed from a similar engine did not contain a film on any region of the wear scar. The presence or absence of the film was attributed to differences in contact pressure between the center and edge of the wear zone. Further studies will be required to substantiate these results whereby components will be removed from the same vehicle that has been subjected to the same maintenance schedule and driving conditions.

The results also showed a considerable amount of wear damage at the center of the wear scar where high contact pressures are expected. The wear damage is evident by the presence of pits and cavities that dominate the topography at the center of the wear scar on both components studied. The inside of the pits is composed of materials that originate from the decomposition products of the lubricant formulation and impurities from the environment.

The combined results of Chapters II-V have advanced the overall understanding of the chemistry, structure, and mechanical strength of antiwear films derived from ZDDP. The studies also demonstrate the importance of starting with fundamental and rudimentary experiments before progressing to more complicated systems. The order in which the data appears in the thesis is

exactly the same as that of the experiments. I initiated with experiments on flat Au substrates that may not be relevant to the engine and built upon these early results, which culminated with the direct analysis of engine components. The studies have built upon previous SPM studies [4, 5] and further demonstrated the utility of SFM and nanoindentation on 'real-world' samples. Scanning probe technologies have generally been employed on flat and uniform samples such as metals, semiconductors, and self assembled monolayers. My studies will help to extend the application of SPM in areas such as the automotive and lubrication industries.

Suggestions for Future Work

A host of new and interesting experiments remain for further investigation. These experiments derive from the fact that SPM techniques are capable of providing information well beyond the morphology and spatial distribution of a substrate or an adsorbed film. For example a powerful extension of SFM is lateral force microscopy (LFM), where an image is generated by monitoring the twisting of a cantilever as it scans over a surface [3]. The degree of twisting is in part a function of the combined tip-sample deformation, which is directly related to the mechanical properties of the surface. LFM has also been used widely by our group and others to map the chemistry of adsorbed films [6, 7]. This technique is therefore ideal to probe the heterogeneity in the chemistry and mechanical properties of ZDDP film on the microscopic scale.

Another mode of imaging referred to force modulation microscopy (FMM) generates contrast based on the elastic properties of a sample [8]. FMM will be an ideal tool to study the differences in elasticity across the pads as was reported recently [4] and to probe differences in elasticity throughout the films. The FMM technique consists of applying a small oscillation force between the sample and tip and monitoring the deflection of the cantilever. Stiffer features on the surface will induce more bending of the cantilever versus softer regions.

Of interest is the recently proposed model that antiwear films from ZDDP consist of a layered structure. XANES spectroscopy results convincingly indicate that the first 0.5 nm of these ZDDP antiwear films consists of a polyphosphate structure while the underlying layer (~300 nm) is mainly comprised of PO_4^{3-} or $\text{P}_2\text{O}_7^{4-}$ that is inter-grown with the iron oxide layer of the substrate [9]. SFM is an ideal technique to provide direct confirmation of this model. Employing tip-assisted removal of the top layer can image such a two-layer structure. Application of sufficient load to the tip will afford the “scraping” of the top layer in a localized region (e.g., a 100×100 nm square). Imaging the same area at lower resolution (e.g., 500×500 nm region) will permit the observation of both layers. The topography will consist of a 0.5 nm deep hole while distinct mechanical properties of the two layers will be resolved in friction images. This experiment was attempted initially with a standard Si_3N_4 tip/cantilever assembly, but the pressure afforded by the standard cantilevers was not sufficient to scrape away film materials. This experiment may work however with a much stiffer cantilever such those used for nanoindentation.

The duplex nature of the film may also be probed with nanoindentation analysis by observing changes in the slope of the nanoindentation profile. The nanoindenter is an ideal tool to detect layered materials, if the layers exhibit different mechanical properties. The layered structure of ZDDP tribofilms could not be confirmed by our studies because the instrument was not able to operate in low force regimes. The next generation of force sensors will make such a study possible. An experiment where the nanoindenter is used to scrape away layers of the film followed by nanoindentation is envisioned. This will allow the determination of the nanomechanical properties of the films at different depths. This was achieved to some extent in a study that used the surface force apparatus to measure the mechanical properties of ZDDP films at different depths [10].

Employing SPM to the study of a class of compounds known as extreme pressure (EP) additives [11] is yet another area that will be of interest to pursue. These additives are generally chlorine and sulfur compounds and are used in situations where the contact geometry mandates extremely high pressures. The morphology and nanomechanical properties of the EP films will be interesting to compare with those of ZDDP tribofilms, which function at lower contact pressures.

My work has demonstrated that SPM technologies may be employed to evaluate the performance of an engine oil blends. This leads to the possibility of utilizing SPM as a diagnostic tool to examine and compare the antiwear performance of “off-the-shelf” commercial engine oils. Engine oil manufacturers

often claim superior performance of their product in relation to another manufacturer. SPM will be an ideal tool to evaluate the validity of these claims by examining film properties such as surface coverage and mechanical strength.

The results from the analysis of engine components have demonstrated that the wear testers can only provide cursory insights about the tribological environment of the engine. The fact that the antiwear film is absent along the center of the wear zone implies that the geometry and pressure of the wear tester is not applicable to highly stressed junctions in the engine. The wear tester may be more relevant to less severe junctions as evidenced by the presence of a film at the periphery of the contact zone where the contact pressure is less. Thus it will be interesting to employ SPM analysis to study the effect of load on the structure of the antiwear films. The load between the coupon and pin is easily controlled in the C – P wear tester. In a previous study the maximum film thickness was shown to occur at a load of 600 N, beyond which the film thickness dropped sharply [12]. The contact pressure at the interface between the rocker arm bridge and the cam likely exceeds the optimal pressure for ZDDP films formation.

The application of SPM technologies to other industrial samples is evolving. A recent study employed tapping mode (TM) SFM to examine the morphological structure of lubricating greases [13]. Grease is composed of high molecular weight hydrocarbons and an organometallic thickener such as lithium hydroxystearate. The non-destructive property of TM SFM makes this an amenable imaging technique to map the topography of soft materials. This work

is currently on-going in our lab where the effect of various cross linkers and thickeners are being examined. In conclusion, it is my sincere hope that these studies will be continued and elaborated on by the next generation of researchers in this area.

References:

1. F. P. Bowden and D. Tabor, Friction and Lubrication of Solids, Oxford University Press, UK, 1950.
2. J. Halling, Principles of Tribology, Macmillan Press Ltd. London, 1975.
3. R. W. Carpick and M. Salmeron, Chem. Rev. 97:1163 (1997).
4. J. F. Graham, C. McCague, and P. R. Norton, Trib. Lett. 6:149 (1999).
5. A. J. Pidduck and G. C. Smith, Wear 212:254 (1997).
6. C. D. Frisbie, L. F. Rozsnyai, A. Noy, M. S. Wrighton, and C. M. Lieber, Science 265:2071 (1994).
7. T. C. Ta and M. T. McDermott, Anal. Chem. 72:2627 (2000).
8. P. Maivald, H. J. Butt, S. A. C. Gould, C. B. Prater, B. Drake, J. A. Gurley, V. B. Elings, and P. K. Hansma, Nanotechnology 2:103 (1991).
9. G. M. Bancroft, M. Kasrai, M. Fuller, Z. Yin, K. Fyfe, and K. H. Tan, Tribol. Lett. 3:47 (1997).
10. S. Bec, A. Tonck, J.-M. George, R. C. Coy, J. C. Bell, and G. W. Roper, Proc. Roy. Soc. Lond. A455:4181 (1999).
11. A. G. Papay, Lubr. Sci. 10:209 (1998).

12. Z. Yin, M. Kasrai, M. Fuller, G. M. Bancroft, K. Fyfe, and K. H. Tan, *Wear* 202:172 (1997).
13. S. Hurley and R. Cann, M., *Nlgi Spokesman* August:7 (2001).

Appendix A

Surface Directed Deposition of Platinum Nanostructures on Graphite by Chemical Vapor Deposition ¹

Preface

The following describes results from a collaborative project with the group of Professor Steve Bergens here in the Department of Chemistry at the University of Alberta. This work was completed during my initial year in the graduate program. The subject matter is not related to the previous chapters and hence will be included as an appendix to the thesis.

Introduction

The chemical vapor deposition of Pt on highly ordered pyrolytic graphite (HOPG) using Pt(COD)(CH₃)₂ (COD is 1,5-cyclooctadiene) (1) as the Pt source has been studied. The ability to control the deposition of thin metal films is of significant technological and economic importance to industries such as microelectronics and catalysis [1, 2]. Chemical vapor deposition (CVD) of organometallic precursors offers a simple alternative to conventional ultra-high vacuum (UHV) deposition methods because metal films are produced under relatively mild conditions of temperature and pressure. Formation of metal films by CVD is often enhanced by optimizing the deposition temperature and pressure, by introducing a reactive gas in the reaction chamber, by using plasma

¹ A form of this appendix was published as: M. Aktary, C.E. Lee, Y. Xing, S.H. Bergens, and M.T. McDermott, *Langmuir*, **16**:5837 (2000).

ion and laser sources, and by using a catalytically active metal to effect the deposition [3-7].

Technologies to control the spatial deposition of materials by CVD are emerging. Preparation of micron-scale metal patterns has been achieved using highly specific CVD in combination with pre-nucleated and chemically patterned substrates [8-10]. In most cases, studies describing the deposition of nanometer-scale structures by CVD have focused on elucidating nucleation events [11] or on the formation of quantum-dots [12, 13]. The production of nanoscale patterns of metals with shapes directed by the substrate has not been reported.

Whitesides et al. showed that platinum black catalyzes the hydrogenation of $\text{Pt}(\text{COD})(\text{CH}_3)_2$ in various solvents under ambient pressures of dihydrogen gas and low to ambient temperatures [14-16]. The hydrogenation results in deposition of platinum adatoms on the surface of Pt black. Furthermore, Hicks et al. showed that the CVD of Pt using CpPtMe_3 (Cp is cyclopentadiene) in dihydrogen is autocatalytic [4, 17]. In addition, metal deposition by electrochemical and thermal means has been shown to nucleate at cleavage defects on HOPG [18, 19]. These results implied that nanoscale patterns of Pt on HOPG could be produced via the following sequence. First, create nanoscale defects on the surface of HOPG by cleaving the surface with adhesive tape [20]. Second, nucleate Pt at the defects from an atmosphere of **1** and dihydrogen. Third, deposit further Pt adatoms on the nucleated sites by autocatalytic hydrogenation of **1**. We now report such a process. The resulting surfaces were

characterized by cyclic voltammetry (CV) and by tapping-mode scanning force microscopy (TM SFM).

Experimental Methods

Reagents and Materials. Ungraded HOPG substrates were a gift from Dr. Arthur Moore, Advanced Ceramic Materials, Cleveland. Pt(COD)(CH₃)₂ (**1**) (COD is 1,5-cyclooctadiene) was synthesized using a procedure from the literature [14]. All solvents used were HPLC grade.

Electrochemical Experiments. Cyclic voltammograms were generated with a Pine Bipotentiostat Model AFCBP1 controlled with Pinechem 2.00 software. The electrolyte 1.0 M H₂SO₄, was purged with argon for at least 10 min prior to use and electrochemical experiments were performed under argon unless stated otherwise. The reference electrode was a self-contained hydrogen electrode that has been named the convenient hydrogen electrode (CHE) [21]. All potentials are reported against this electrode. The counter electrode was a platinum wire behind a D-porosity glass frit.

SFM Imaging. TM SFM images were obtained in air using a Nanoscope III Multimode (Digital Instruments, Santa Barbara CA). Si cantilevers were oscillated at their resonance frequency (300 kHz). They were either purchased from Digital Instruments or they were a gift from the Alberta Microelectronics Center, Edmonton. Scanning was carried out with a constant amplitude of oscillation. An important parameter in TM SFM imaging is the ratio of the set point (or imaging) amplitude, A_{sp} , to the oscillation amplitude, A_0 where $r_{sp} =$

A_{sp}/A_o . This ratio governs the tapping force between the tip and the sample. All images shown here were collected with r_{sp} between 0.55 to 0.65 (moderate tapping force). The scan rate was between 1.0 and 2.0 Hz. The images presented here are representative of many images taken at different points on each sample. Images were software flattened and are shown unfiltered.

CVD Experiments. The center of a glass plate was coated with the CVD precursor, $Pt(COD)(CH_3)_2$ (**1**), by evaporating a few drops of **1** dissolved in pentane (~10 mM). The number of drops of pentane solution controls the amount of **1** on the plate. A freshly cleaved HOPG substrate is fastened with Teflon tape parallel to the glass plate and over the drop site using 5 mm glass spacers. The apparatus is laid flat on the bottom of a hot wall reaction flask, the atmosphere is exchanged with dihydrogen gas (1 atm), and the flask immersed for 3 min in a silicon oil bath preheated to 180°C. It is likely that heating to 180°C is required only to generate an atmosphere of **1** near the graphite surface because hydrogenation of **1** over Pt in hexane occurs at -20°C [14]. The temperature within the reaction flask was no more than 60 °C. We estimate that the deposition rate of our process is ~10 nm/min.

Results and Discussions

Cyclic voltammetry confirmed that Pt had deposited onto HOPG by CVD using **1**. Figure 7.1 contains current-potential curves of HOPG substrates recorded in 1.0 M H_2SO_4 . Curve A is the voltammogram on a freshly cleaved HOPG substrate consisting only of current due to double-layer charging and

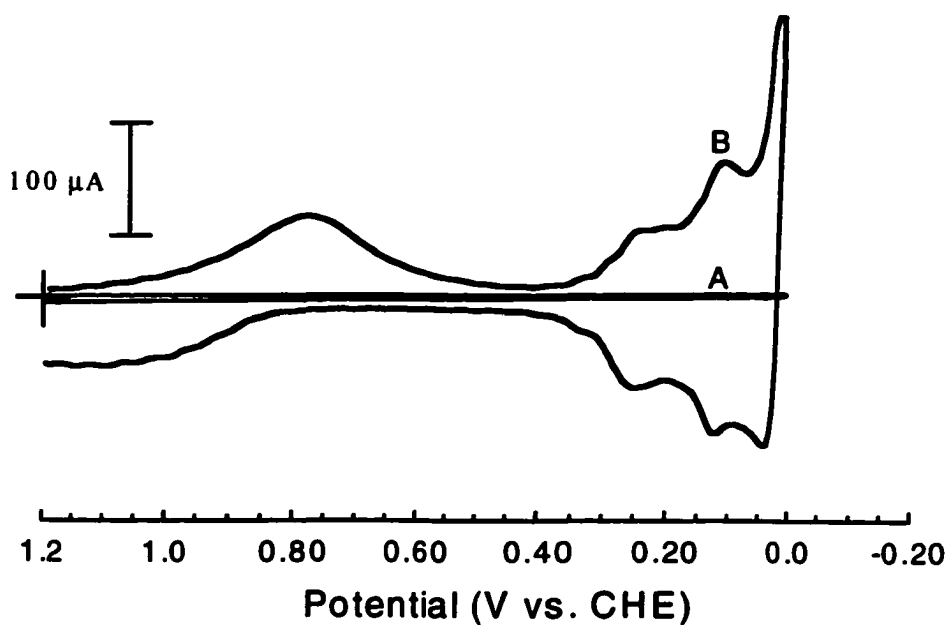


Figure 7.1. (A) Cyclic voltammetry of a freshly cleaved HOPG electrode in 1.0 M H_2SO_4 . (B) Cyclic voltammetry of CVD Pt on HOPG in 1.0 M H_2SO_4 . Both curves represent the first cycle of the potential sweep from 1.2 to 0.0 V vs. CHE at a scan rate of 1 V/sec.

showing no indication of any Faradaic processes. Curve B results from an HOPG substrate following CVD of Pt by the gas phase hydrogenation of **1**. Several Faradaic waves are now observed that are well-known and diagnostic of polycrystalline Pt surfaces [22].

The architecture of Pt deposited by CVD was evaluated with TM SFM. Figure 7.2A shows defects generated on HOPG by cleaving with adhesive tape. In this $12 \times 12 \mu\text{m}$ topographic image, cleavage steps are shown running parallel from the top left of the image to the bottom right. The measured height of these steps corresponds to multiples of the interlayer spacing of graphite (0.335 nm) indicating that the “face” of each step is composed of edge plane graphite [23]. Figure 7.2B is an $11 \times 11 \mu\text{m}$ topographic TM SFM image of a HOPG substrate following the CVD of **1**. The image reveals Pt structures that range 20 to 30 nm in height and are aligned along the cleavage steps. Importantly, Figure 7.2B illustrates the ability of this CVD process to deliver small amounts of Pt as is required for the fabrication of nanostructured materials. The morphology of the Pt structures in Figure 7.2B resembles a string of beads. In some cases, the Pt particles overlap each other, while in others the particles are bridged by thin (~10 nm high) Pt nanowires (highlighted by arrows).

The structures shown in Figure 7.2B result from initial nucleation of Pt along edge plane HOPG followed by growth through autocatalytic deposition. As $\text{Pt}(\text{COD})\text{Me}_2$ does not appreciably react directly with H_2 , [14] it is believed the mechanism of the nucleation is activation of $\text{Pt}(\text{COD})\text{Me}_2$ by the oxygen containing functional groups found on edge plane HOPG. In a study using

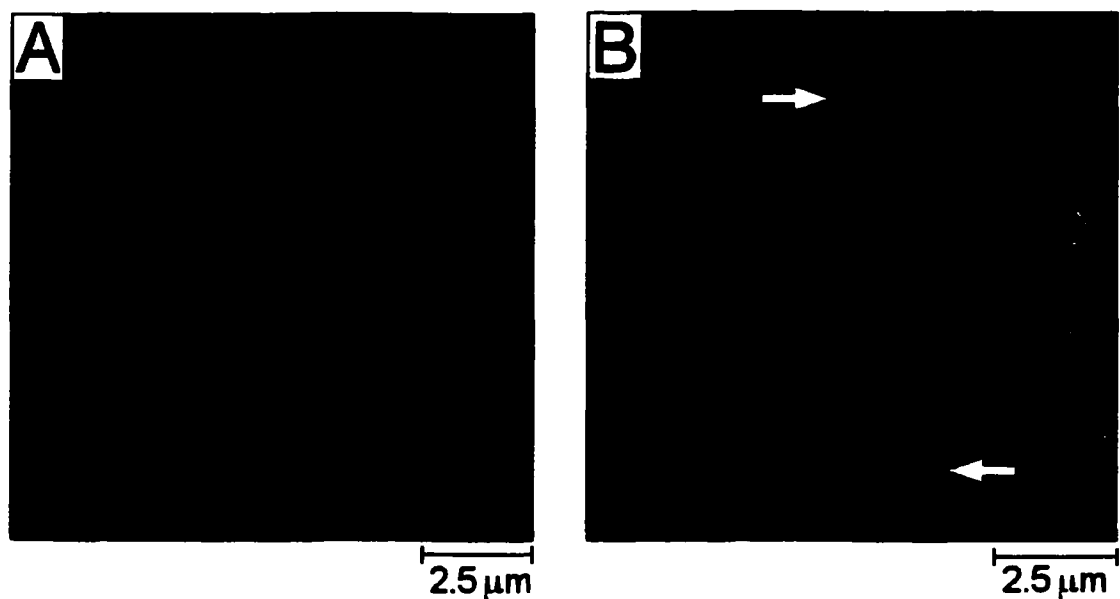


Figure 7.2. (A) $12 \times 12 \mu\text{m}$ topographic TM SFM image of freshly cleaved HOPG (z-scale = 10 nm). (B) $11 \times 11 \mu\text{m}$ topographic image of Pt deposited on HOPG by CVD (z-scale = 80 nm). The arrows in (B) highlight ~ 10 nm high nanowires that bridge Pt particles.

CpPtMe₃ precursor, an analog of 1, Hicks et al. proposed that the initial nucleation of CpPtMe₃ onto substrates such as silica glass and Teflon occur by electrophilic attack on CpPtMe₃ by surface hydroxyl groups [17]. Pristine basal plane HOPG is free of functional groups, and oxide moieties exist only at edge plane sites [24]. As shown in Figure 7.3, it is proposed that the initial nucleation of Pt proceeds by protonolysis of the Pt-Me bond in 1 by an edge-site O-H unit. Once activated, the complex reacts with H₂ to nucleate a Pt atom and to generate alkanes. The nucleated Pt atoms then catalyze further hydrogenation of 1 [25]. Nucleation on HOPG edge plane oxides was further confirmed by carrying out the deposition on oxidized HOPG. Oxidation of HOPG in air at 650°C is known to produce a high density of edge plane sites due to the formation of monolayer deep pits on the basal plane [26]. Deposition of Pt on this "pitted" HOPG using 1 under the same conditions generated a more uniform Pt film. Also shown in Figure 7.2B are several Pt particles not associated with cleavage defects. These particles arise from nucleation at point defects (e.g., vacancies) on the otherwise defect-free basal plane similar to the electrochemical nucleation of Ag and Pt on basal plane HOPG [27, 28].

Figure 7.2B also shows that the Pt beads vary in size and that there are very thin nanowires running along the cleavage steps. The larger beads are a result of early nucleation events and the smaller beads a result of later nucleation. The complete saturation of the defect site with Pt implies the kinetics leading to nucleation on the edge plane is rapid. The nanowires connecting the beads may result from growth along the defect from the beads, similar to growth

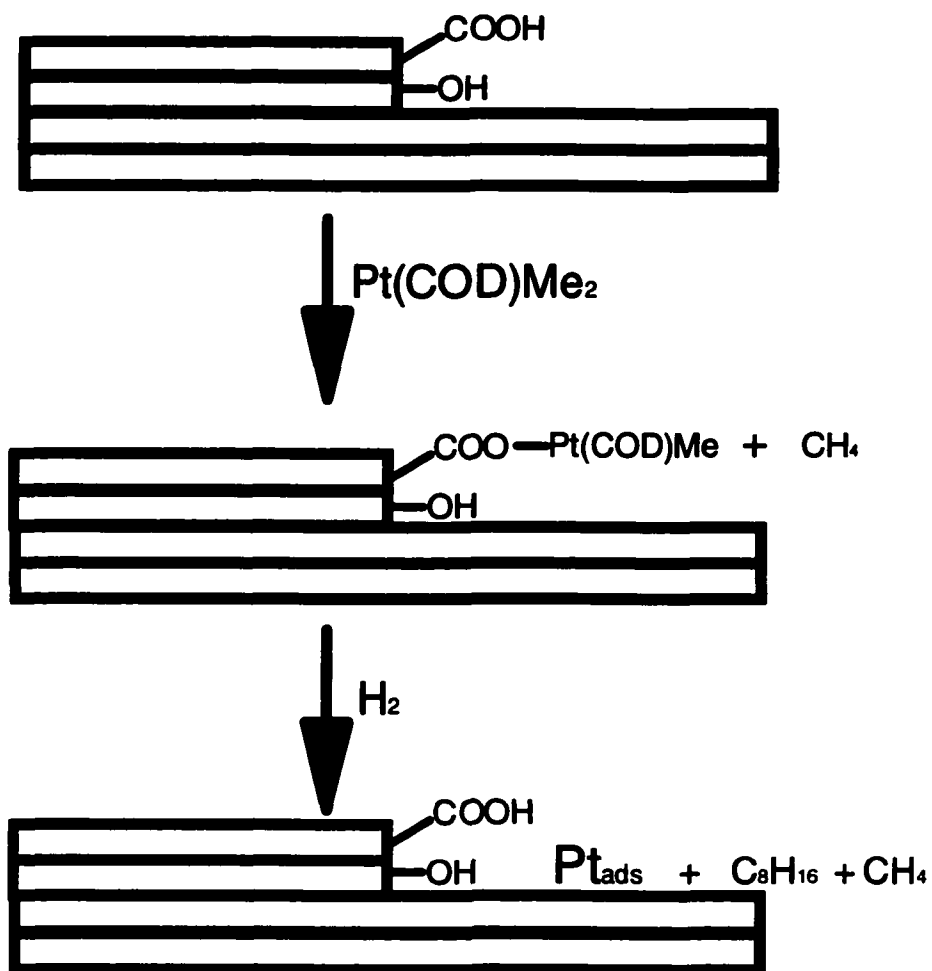


Figure 7.3. Possible nucleation mechanism for the CVD of $\text{Pt}(\text{COD})(\text{CH}_3)_2$ on the edge plane sites of HOPG leading to adsorbed Pt metal (Pt_{ads}) particles.

onto the basal plane (*vide infra*). The deposition of other metals on HOPG does not result in the bead-wire structures observed here. For example, it was recently reported that the evaporative deposition of Ag atoms onto HOPG resulted in a series of isolated, unconnected particles aligned along cleavage defects [19].

The final size of Pt structures deposited is controlled by the loading of 1 on the glass slide and by the deposition time. TM SFM images of HOPG substrates with higher Pt coverages reveal larger particles with morphologies that are different from samples with low Pt coverages. Figure 7.4 contains an $8 \times 8 \mu\text{m}$ topographic image of Pt deposited at higher coverage. Linear nanowire type structures are again apparent traversing diagonally from the top left of the image due to cleavage defect decoration. In general, the structures in Figure 7.4 are laterally larger but similar in height ($\sim 30 \text{ nm}$) to those in Figure 7.2B, implying 2-dimensional growth is preferred over 3-dimensional growth. Several dendritic structures emanate from the decorated defects suggesting anisotropic growth. This anisotropy may result in part from strain fields as proposed for the CVD of SiH_4 on Pt(111) [29] or from mass transport limitations along the basal plane. The latter is a requirement for dendritic growth [30]. The nanowire running perpendicular on the upper right of Figure 7.4 results from nucleation on a defect running perpendicular to the direction of the main defects. Pt coverages higher than those shown in Figure 7.4 resulted in growth and coalescence of islands and yielded a uniform Pt film.

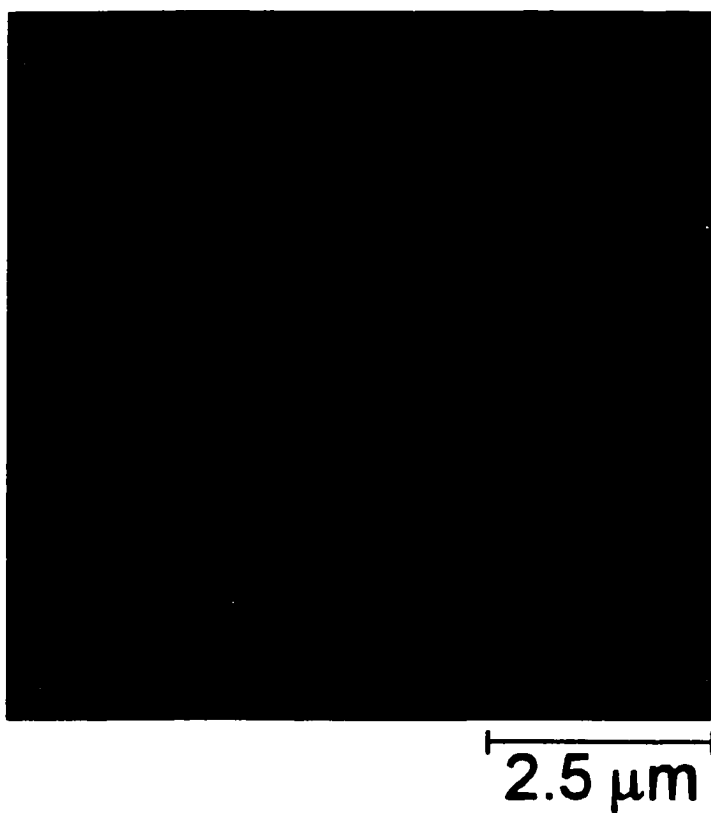


Figure 7.4. $8 \times 8 \mu\text{m}$ topographic (z-scale 60 nm) TM SFM image of Pt deposited on HOPG by CVD.

Important to the application of thin films is strong adhesion between the metal and the substrate. We note that CVD Pt particles observed on both the edge and basal plane are stable to repeated imaging by TM SFM and scanning tunneling microscopy (STM) for weeks, indicating strong interactions with the substrate. Penner et al., reported that electrochemically deposited Pt particles are weakly physisorbed to basal plane HOPG and are not stable to imaging with conventional SFM or STM [28].

Conclusions

It has been shown that the hydrogenation of $\text{Pt}(\text{COD})(\text{CH}_3)_2$ can be used to deposit Pt nanostructures onto HOPG substrates by CVD. Defects sites on HOPG can be used to nucleate and guide the deposition of Pt structures opening pathways for the creation of nanometer scale patterns of metallic species. We are currently producing pre-defined, nanometer-scale defect patterns on HOPG substrates with scanning tunneling microscopy to be used as templates for Pt nanostructures. We are also testing the ability of specific chemical groups to serve as nucleation sites for Pt CVD on other substrates.

References:

1. R. J. Puddephatt, *Polyhedron* **13**:1233 (1994).
2. D. C. Bradley, *Polyhedron* **13**:1111 (1994).
3. N. H. Dryden, R. Kumar, E. Ou, M. Rashidi, S. Roy, P. R. Norton, and R. J. Puddephatt, *Chem. Mater.* **3**:677 (1991).

4. Z. Xue, J. M. Strouse, D. K. Shuh, C. B. Knobler, H. D. Kaesz, R. F. Hicks, and S. R. Williams, *J. Am. Chem. Soc.* 111:8779 (1989).
5. R. Kumar, M. Rashidi, S. Roy, and R. J. Puddephatt, *Polyhedron* 8:551 (1989).
6. D. Braichotte, C. Garrido, and H. v. d. Bergh, *Appl. Surf. Sci.* 46:9 (1990).
7. Y. Zhang, S. W. Choi, and R. J. Puddephatt, *J. Am. Chem. Soc.* 119:9295 (1997).
8. N. L. Jeon, R. G. Nuzzo, Y. Xai, M. Mrksich, and G. M. Whitesides, *Langmuir* 11:3024 (1995).
9. B. Lecohier, J. M. Philippoz, and H. v. d. Bergh, *J. Vac. Sci. Technol. B* 10:262 (1992).
10. C. Lampe-Onnerud, U. Jansson, A. Harsta, and J.-O. Carlsson, *J. Cryst. Growth* 121:223 (1992).
11. L.-S. Hong and M.-Z. Lin, *Jpn. J. Appl. Phys.* 36:L711 (1997).
12. S. Ruvimow, P. Werner, K. Scheerschmidt, U. Gosele, J. Heydenreich, U. Richter, N. N. Ledentsov, M. Grundmann, D. Bimberg, V. M. Ustinov, A. Y. Egorov, P. S. Kop'ev, and Z. I. Alferov, *Phys. Rev. B* 51:14766 (1995).
13. F. Heinrichsdorff, A. Krost, M. Grundmann, D. Bimberg, A. Kosogov, and P. Werner, *Appl. Phys. Lett.* 68:3284 (1996).
14. T. M. Miller, A. N. Isumi, Y. S. Shih, and G. M. Whitesides, *J. Am. Chem. Soc.* 110:3146 (1988).
15. T. M. Miller, T. J. McCarthy, and G. M. Whitesides, *J. Am. Chem. Soc.* 110:3156 (1988).

16. T. M. Miller and G. M. Whitesides, *J. Am. Chem. Soc.* 110:3164 (1988).
17. Z. Xue, H. Thridandam, H. D. Kaesz, and R. F. Hicks, *Chem. Mater.* 4:162 (1992).
18. J. L. Zubimendi, L. Vasquez, P. Ocon, J. M. Vara, W. E. Triaca, R. C. Salvarezza, and A. J. Arvia, *J. Phys. Chem.* 97:5095 (1993).
19. A. Stabel, K. Eichhorst-Gerner, J. P. Rabe, and A. R. Gonzalez-Elipe, *Langmuir* 14:7324 (1998).
20. H. Chang and A. J. Bard, *Langmuir* 7:1143 (1991).
21. S. Gong, J. Lu, and H. Yan, *J. Electroanal. Chem.* 436:291 (1997).
22. P. N. Ross Jr, *J. Electrochem. Soc.* 126:67 (1979).
23. M. T. McDermott and R. L. McCreery, *Langmuir* 10:4307 (1994).
24. R. L. McCreery, in Electroanalytical Chemistry, Vol. 17 (A. J. Bard, ed.), Marcel Dekker, New York, 1991, p. 221.
25. C. E. Lee, P. B. Tiege, Y. Xing, J. Nagendran, and S. H. Bergens, *J. Am. Chem. Soc.* 119:3543 (1997).
26. H. Chang and A. J. Bard, *J. Am. Chem. Soc.* 113:5587 (1991).
27. J. V. Zoval, R. M. Stiger, P. R. Biernacki, and R. M. Penner, *J. Phys. Chem.* 100:837 (1996).
28. J. V. Zoval, J. Lee, S. Gorer, and R. M. Penner, *J. Phys. Chem. B* 102:1166 (1998).
29. J. C. Bondos, A. A. Gewirth, and R. G. Nuzzo, *J. Phys. Chem. B* 103:3099 (1999).
30. W. A. Tiller, *Science* 146:871 (1964).